



LUND UNIVERSITY

Using Light to Probe Surface Electrochemical Processes

Linpe, Weronica

2021

[Link to publication](#)

Citation for published version (APA):

Linpe, W. (2021). *Using Light to Probe Surface Electrochemical Processes*. Lund University.

Total number of authors:

1

General rights

Unless other specific re-use rights are stated the following general rights apply:

Copyright and moral rights for the publications made accessible in the public portal are retained by the authors and/or other copyright owners and it is a condition of accessing publications that users recognise and abide by the legal requirements associated with these rights.

- Users may download and print one copy of any publication from the public portal for the purpose of private study or research.
- You may not further distribute the material or use it for any profit-making activity or commercial gain
- You may freely distribute the URL identifying the publication in the public portal

Read more about Creative commons licenses: <https://creativecommons.org/licenses/>

Take down policy

If you believe that this document breaches copyright please contact us providing details, and we will remove access to the work immediately and investigate your claim.

LUND UNIVERSITY

PO Box 117
221 00 Lund
+46 46-222 00 00



Using Light to Probe Surface Electrochemical Processes

WERONICA LINPÉ

SYNCHROTRON RADIATION RESEARCH | FACULTY OF SCIENCE | LUND UNIVERSITY





Faculty of Science
Department of Physics
Division of Synchrotron Radiation Research

ISBN 978-91-7895-749-1



Using Light to Probe Surface Electrochemical Processes

Weronica Linpé



LUND
UNIVERSITY

DOCTORAL THESIS

by due permission of the Faculty of Science, Lund University, Sweden.
To be defended in the Rydberg Lecture Hall at the Department of Physics,


4 June 2021 at 9:00

Faculty opponent

Professor Julia Kunze-Liebhäuser, Universität Innsbruck

Organization LUND UNIVERSITY, Divison of Synchrotron Radiation Research, Department of Physics Box 118, S-221 00 Lund Author: Weronica Linpé	Document name DOCTORAL THESIS	
	Date of disputation 4 June 2021	
	Sponsoring organization	
Title and subtitle Using Light to Probe Surface Electrochemical Processes		
Abstract <p>This thesis shows how various light-based <i>in situ</i> techniques can be used to follow different surface electrochemical processes such as electrochemical deposition into Nanoporous Anodic Aluminium Oxide (NP-AAO) templates and the surface structure of electrodes. Techniques based on both x-rays and visible light were used to follow surface structures and compositions, <i>in situ</i>. The samples were also investigated with <i>ex situ</i> techniques, such as scanning electron microscopy (SEM), transmission electron microscopy (TEM) and various other techniques. Templated electrodeposition processes, which can be used for growing various nanostructures with applications in for example gas sensors, catalysts, electrocatalysts and colouring of metal products [1]–[10] were studied. Cyclic voltammetry (CV) for investigating electrooxidation and corrosion of model systems as well as real industrial materials [11]–[14] was combined with Surface X-ray Diffraction and 2-Dimensional Surface Optical Reflectance.</p> <p>Electrochemical deposition of Sn, Pd and Au into NP-AAO was investigated with both <i>in situ</i> and <i>ex situ</i> methods to gain information about the deposition process, the influence of the NP-AAO template on the growth of the nanostructures and the chemical and crystallographic nature of the grown nanostructures. For the Sn, it was possible to determine that the grown nanostructures were metallic with a β-Sn crystal structure and a compression of the nanostructures due to the confinement of the pores were measured. Both the Pd and the Au nanostructures were constructed of crystalline grains with grain sizes in the range of the pore diameter. A compressive and tensile strain could be measured across and along the nanostructures, respectively.</p> <p>The combination of 2-Dimensional Surface Optical Reflectance (2D-SOR), an optical microscope, with a modified electrochemical cell, was investigated through cyclic voltammetry measurements on Au, Pd and Super Duplex Stainless Steel and anodization of aluminium. The measured reflectance could be correlated with characteristic features in the CV curve corresponding to oxidation and reduction of the surface. By combining 2D-SOR with High Energy Surface X-ray Diffraction (HESXRD) during CV measurements the reflectance could be correlated with the atomic changes of the Au(111) surface. It was also shown that 2D-SOR could detect monolayer changes of the surface, due to its sensitivity to the increased electron density of the Herringbone reconstruction, a rearrangement of the atoms in the topmost layer of the Au(111) single crystal surface. By applying this method to polycrystalline samples, it was possible to follow how differently oriented grains react differently during the same experimental conditions, showing the possibility for 2D-SOR to image inhomogeneous surfaces.</p> <p>The Au(111) single crystal was further studied using CV and potential stepping going into the oxygen evolution reaction (OER). The combined HESXRD and 2D-SOR measurements detected a roughening of the surface as it was oxidized and during the OER. These measurements also suggest that the oxide on the Au(111) single crystal is amorphous, due to the lack of oxidation peaks in the measured diffraction pattern. With X-ray photoelectron spectroscopy measurements, it could be shown that sulphate species absorb on the surface before any oxide is detected, the oxide is then formed and detected as the sulphate desorbs.</p> <p>The possibility to follow and understand these different surface reactions gives knowledge which in the future could be used for example for the continued development of fuel cells, the development of devices, sensors, catalysts and to develop more corrosion-resistant materials.</p>		
Keywords: Electrochemistry, X-ray methods, In situ, Synchrotron radiation, Ex situ, Single Crystal, Polycrystalline, Aluminium oxide, Au, Pd, Pt, Sn, Super duplex stainless steel.		
Classification system and/or index terms (if any)		
Supplementary bibliographical information		Language
ISSN and key title		ISBN 978-91-7895-749-1 (print) 978-91-7895-750-7 (pdf)
Recipient's notes	Number of pages	Price
	Security classification	

I, the undersigned, being the copyright owner of the abstract of the above-mentioned dissertation, hereby grant to all reference sources permission to publish and disseminate the abstract of the above-mentioned dissertation.

Signature 

Date 2021-04-21

Using Light to Probe Surface Electrochemical Processes

Weronica Linpé



LUND
UNIVERSITY

Copyright Weronica Linpé

Cover image: High Energy Surface X-ray Diffraction Pattern from a Au(111) single crystal as the surface has started to become unordered and rough during the electrochemical oxygen evolution reaction.

Funding information: The thesis work was financially supported by the Swedish Research Council by the Röntgen Ångström Cluster “In situ High Energy X-Ray Diffraction from Electrochemical Interfaces” (HEXCHEM) (Project No. 2015-06092).

Faculty of Science
Department of Physics
Division of Synchrotron Radiation Research

ISBN: 978-91-7895-749-1 (print)

ISBN: 978-91-7895-750-7 (pdf)

Printed in Sweden by Media-Tryck, Lund University
Lund 2021



Media-Tryck is a Nordic Swan Ecolabel certified provider of printed material. Read more about our environmental work at www.mediatryck.lu.se

MADE IN SWEDEN 

To my family, both on earth and in heaven.

Table of Contents

Preface	iii
List of publications.....	iv
List of abbreviation	vii
Abstract	ix
Populärvetenskaplig sammanfattning	xi
Acknowledgement.....	xii
Using Light to Probe Surface Electrochemical Processes	1
Introduction	3
Materials and elements	5
Single crystals	5
Reciprocal space.....	7
Polycrystalline & amorphous samples	8
Surface reconstruction.....	9
Aluminium (Al).....	9
Aluminium oxides and hydroxides	10
Native and barrier layer aluminium oxide.....	11
Porous non-ordered and ordered aluminium oxide	12
Tin (Sn)	16
Palladium (Pd).....	17
Platinum (Pt)	17
Super Duplex Stainless Steel (SAF 2507).....	17
Gold (Au)	18
Au(111)	18
Au oxide and hydroxide	20
Electrochemical Au oxide formation	21
Our proposed Au oxide formation	22
Electrochemistry	25

Electrochemical cell	25
Electrochemical methods	29
Potential stepping/Potential step voltammetry	29
Cyclic Voltammetry (CV).....	29
Linear Sweep Voltammetry (LSV)	33
Anodization	33
Electrochemical deposition	35
X-ray methods.....	37
X-rays and Synchrotrons.....	37
Grazing incidence angle geometry	39
X-ray diffraction (XRD).....	41
Surface X-ray diffraction (SXRD)	45
Grazing Transmission Small Angle X-ray Scattering (GTSAXS).....	51
X-ray spectroscopy methods	54
X-ray Fluorescence (XRF).....	56
X-ray Absorption Spectroscopy (XAS)	57
X-ray Absorption Near Edge Structure (XANES).....	58
X-ray Photoelectron Spectroscopy (XPS).....	59
Non-X-ray based techniques.....	65
2D-Surface Optical Reflectance (2D-SOR)	65
Atomic Force Microscopy (AFM)	67
Focused Ion Beam-Scanning Electron Microscope (FIB-SEM).....	68
Scanning Electron Microscope (SEM).....	68
Focused Ion Beam (FIB).....	71
Transmission Electron Microscope (TEM).....	72
Energy Dispersive X-ray Spectroscopy (EDS)	73
Selected Area Electron Diffraction (SAED)	74
Electron Backscattering Diffraction (EBSD).....	74
Low Energy Electron Diffraction (LEED).....	75
Summary of papers	77
Conclusions & Outlook	85
References	87

Preface

List of publications

Included in this thesis:

Paper I. *Observing growth under confinement: Sn nanopillars in porous alumina templates*, G. S. Harlow, J. Drnec, T. Wiegmann, W. Linpé, J. Evertsson, A. R. Persson, R. Wallenberg, E. Lundgren and N. A. Vinogradov, *Nanoscale Adv.* **1** (2019) 4764.

I was involved in the measurements and discussion about the paper.

Paper II. *The State of Electrodeposited Sn Nanopillars within Porous Anodic Alumina from in Situ X-ray Observation*, W. Linpé, G. S. Harlow, J. Evertsson, U. Hejral, G. Abbondanza, F. Lenrick, S. Seifert, R. Felici, N. A. Vinogradov, E. Lundgren, *ACS Appl. Nano Mater.* **2** (2019) 3031

I was involved in the measurements, performed most of the analysis and wrote the paper.

(The final fitting of the GTSAXS data was performed by G. S. Harlow)

Paper III. *Electrochemical Fabrication and Characterization of Palladium Nanowires in Nanoporous Alumina Templates*, A. Larsson, G. Abbondanza, W. Linpé, F. Carlá, P. Mousley, C. Hetherington, E. Lundgren and G. S. Harlow, *J. Electrochem. Soc.* **167** (2020) 122514

I was involved in the measurements and discussion about the paper.

Paper IV. *Electrochemical synthesis of Au nanostructures using porous anodic alumina templates*, G. Abbondanza, A. Larsson, W. Linpé, C. Hetherington, F. Carla, E. Lundgren, and G. S. Harlow

In Manuscript

I was involved in the measurements and discussion about the paper.

Paper V. *An electrochemical cell for 2-dimensional surface optical reflectance during anodization and cyclic voltammetry*, W. Linpé, G. S. Harlow, A. Larsson, G. Abbondanza, L. Rämisch, S. Pfaff, J. Zetterberg, J. Evertsson, E. Lundgren, *Rev. Sci. Instrum.* **91** (2020) 044101

I was involved in the measurements, and the development of the new electrochemical cell design and performed the main analysis of the data as well as took part in the discussions and writing of the paper.

Paper VI. *Operando Reflectance Microscopy on Polycrystalline Surfaces in Thermal Catalysis, Electrocatalysis and Corrosion*, S. Pfaff, A. Larsson, D. Orlov, G. S. Harlow, G. Abbondanza, W. Linpé, L. Rämisch, S. M. Gericke, J. Zetterberg, and E. Lundgren, *ACS Appl. Mater. Interfaces* (2021)

I took part in the discussion about the paper.

Paper VII. *The brightest gold: A combined high energy x-ray diffraction and optical reflectance study of the Au(111) surface during cyclic voltammetry*, W. Linpé, L. Rämisch, G. Abbondanza, A. Larsson, S. Pfaff, J. Zetterberg, L. R. Merte, L. Jacobse, A. Stierle, Z. Hegedues, U. Lienert, E. Lundgren, and G. S. Harlow

In Manuscript

I was the main responsible for the planning and execution of the experiment and wrote the paper. L. Rämisch analysed the data in collaboration with me.

Paper VIII. *The electro-oxidation of Au(111): An ex situ Electrochemical, XPS and LEED study*, M. Peña Diaz, W. Linpé, G. S. Harlow, E. Lundgren, S. Barja

In Manuscript

I took part in the discussion about the paper and performed preliminary measurements at MAX IV.

Paper IX. *High-energy surface x-ray diffraction reveals the dynamic surface structure of Au(111) in acidic media*, G. Harlow, W. Linpé, S. Pfaff, L. Jacobse, V. Vonk, G. Abbondanza, M. Peña Diaz, S. Barja, A-C. Dippel, O. Gutowski, A. Larsson, L. Rämisch, L. Mertr, A. Stierle, E. Lundgren

In Manuscript

I lead the experimental planning, took part in the experiment and discussions about the paper.

Related papers but not included in the thesis:

Self-organization of porous alumina oxides studied in situ with grazing-incidence transmission small-angle X-ray scattering, J. Evertsson, N. A. Vinogradov, G. S. Harlow, F. Carlà, L. Rullik, W. Linpé, R. Felici, E. Lundgren, RSC Advances **8** (2018), 18980.

Observation of Pore Growth and Self-Organization in Anodic Alumina by Time-Resolved X-ray Scattering, N. A. Vinogradov, G. S. Harlow, F. Carlà, J. Evertsson, L. Rullik, W. Linpé, R. Felici and E. Lundgren, ACS Appl. Nano Mater. **1** (2018) 1265

In situ scanning x-ray diffraction reveals strain variations in electrochemically grown nanowires, A. Larsson, G. Abbondanza, L. Rämisch, W. Linpé, D. V. Novikov, E. Lundgren, G. S. Harlow, J. Phys. D: Appl. Phys. **54** (2021), 235301

List of abbreviation

2D-SOR	2-dimensional/(2-D) surface optical reflectance
AFM	Atomic Force Microscopy
BA	Born Approximation
BCC	Body Centred Cubic
CE	Counter Electrode
CV	Cyclic Voltammetry
DBWA	Distorted Wave Born Approximation
EC	Electrochemical/Electrochemistry
ECD	Electrochemical Deposition
EBSD	Electron Back Scattering Diffraction
EDS	Energy Dispersive X-ray Spectroscopy
FIB	Focused Ion Beam
FIB-SEM	Focused Ion Beam-Scanning Electron Microscopy
FCC	Face Centred Cubic
GISAXS	Grazing Incidence Small-Angle X-ray Scattering
GTSAXS	Grazing incidence Transmission Small-Angle X-ray Scattering
HB	Herringbone (reconstruction)
HCP	Hexagonal Close Packed
HESXRD	High Energy Surface X-ray Diffraction
LEED	Low Energy Electron Diffraction
LSV	Linear Sweep Voltammetry
NP-AAO	Nanoporous Anodic Aluminium Oxide
OCP	Open-Circuit Potential
PD	Path Difference
PZC	Potential of Zero Charge
RE	Reference Electrode
SAXS	Small-Angle X-ray Scattering
SC	Simple Cubic

SEM	Scanning Electron Microscopy
SXRD	Surface X-ray Diffraction
TEM	Transmission Electron Microscopy
UHV	Ultra High Vacuum
WE	Working Electrode
XANES	X-ray Absorption Near Edge Structure
XAS	X-ray Absorption Spectroscopy
XRD	X-ray Diffraction
XRF	X-ray Fluorescence
XPS	X-ray Photoelectron spectroscopy

Abstract

This thesis shows how various light-based *in situ* techniques can be used to follow different surface electrochemical processes such as electrochemical deposition into Nanoporous Anodic Aluminium Oxide (NP-AAO) templates and the surface structure of electrodes. Techniques based on both x-rays and visible light were used to follow surface structures and compositions, *in situ*. The samples were also investigated with *ex situ* techniques, such as scanning electron microscopy (SEM), transmission electron microscopy (TEM) and various other techniques. Templated electrodeposition processes, which can be used for growing various nanostructures with applications in for example gas sensors, catalysts, electrocatalysts and colouring of metal products [1]–[10] were studied. Cyclic voltammetry (CV) for investigating electrooxidation and corrosion of model systems as well as real industrial materials [11]–[14] was combined with Surface X-ray Diffraction and 2-Dimensional Surface Optical Reflectance.

Electrochemical deposition of Sn, Pd and Au into NP-AAO was investigated with both *in situ* and *ex situ* methods to gain information about the deposition process, the influence of the NP-AAO template on the growth of the nanostructures and the chemical and crystallographic nature of the grown nanostructures. For the Sn, it was possible to determine that the grown nanostructures were metallic with a β -Sn crystal structure and a compression of the nanostructures due to the confinement of the pores were measured. Both the Pd and the Au nanostructures were constructed of crystalline grains with grain sizes in the range of the pore diameter. A compressive and tensile strain could be measured across and along the nanostructures, respectively.

The combination of 2-Dimensional Surface Optical Reflectance (2D-SOR), an optical microscope, with a modified electrochemical cell, was investigated through cyclic voltammetry measurements on Au, Pd and Super Duplex Stainless Steel and anodization of aluminium. The measured reflectance could be correlated with characteristic features in the CV curve corresponding to oxidation and reduction of the surface. By combining 2D-SOR with High Energy Surface X-ray Diffraction (HESXRD) during CV measurements the reflectance could be correlated with the atomic changes of the Au(111) surface. It was also shown that 2D-SOR could detect monolayer changes of the surface, due to its sensitivity to the increased electron density of the Herringbone reconstruction, a rearrangement of the atoms in the topmost layer of the Au(111) single crystal surface. By applying this method to polycrystalline samples, it was possible to follow how differently oriented grains react differently during the same experimental conditions, showing the possibility for 2D-SOR to image inhomogeneous surfaces.

The Au(111) single crystal was further studied using CV and potential stepping going into the oxygen evolution reaction (OER). The combined HESXRD and 2D-

SOR measurements detected a roughening of the surface as it was oxidized and during the OER. These measurements also suggest that the oxide on the Au(111) single crystal is amorphous, due to the lack of oxidation peaks in the measured diffraction pattern. With X-ray photoelectron spectroscopy measurements, it could be shown that sulphate species absorb on the surface before any oxide is detected, the oxide is then formed and detected as the sulphate desorbs.

The possibility to follow and understand these different surface reactions gives knowledge which in the future could be used for example for the continued development of fuel cells, the development of devices, sensors, catalysts and to develop more corrosion-resistant materials.

Populärvetenskaplig sammanfattning

Kemiska reaktioner drivna av en ström eller som producerar en ström heter elektrokemiska reaktioner och finns överallt omkring oss, ta bara till exempel ett batteri, här produceras en ström som kan driva till exempel din mobiltelefon. Förståelsen för dessa kemiska reaktioner och hur de påverkar den yta där reaktionerna sker är därför viktig. Det är också viktigt att förstå hur olika strukturer reagerar på den kemiska reaktionen då ett material kan ha många olika strukturer på sin yta samtidigt. Ett område som har fått stor betydelse är just elektrokatalys, där reaktionen vattendelning är av intresse och guld är ett av de material som kan användas som katalysator för att driva reaktionen. Denna reaktion kan användas för att producera väte till bränsleceller, en nödvändig utveckling för att skifta världens energikällor till förnybara. Ett annat viktigt område är produktionen av nanotrådar och nano partiklar då de har många användningsområden, i allt ifrån sensorer och katalysatorer till något så enkelt som att färga aluminiumprodukter. Undersökningar med hjälp av röntgenstrålning och synligt ljus kan ge en ökad förståelsen för olika elektrokemiska processer, var till exempel oxidering av en yta eller hur nanotrådar växer inuti en ordnad struktur kan studeras under reaktionens gång.

I denna avhandling har potentialen av att använda 2D-SOR, ett optiskt reflektants mikroskop, för att undersöka yt-elektrokemiska reaktioner påvisats. Denna teknik kan detektera förändringar i en ytas reflektans då elektrokemiska reaktioner sker. Även möjligheten att visualisera olika strukturer i materialen med denna teknik är av stor nytta. Guld har även studerats i djupare utsträckning i denna avhandling för att få en bättre förståelse av dess yt-förändringarna då det oxiderar och då syreproduktion sker på dess yta. Nanotråds växt inuti porös aluminiumoxid har också studerats i denna avhandling, vilket gav både kunskap om hur nanotrådarna växte och hur den porösa aluminiumoxiden i vilken de växte påverkade nanotrådarna.

Denna avhandling är del av Röntgen-Ångström projektet HEXCHEM (In situ High Energy X-ray Diffraction from Electrochemical interfaces). Detta projekt är ett samarbete mellan tyska och svenska forskningsgrupper som fokuserar på att använda synkrotron (röntgen) experiment för att studera elektrokemiska yt-processer. Denna avhandling bidrar till detta projekt genom sina studier av nanotrådsväxt i porös aluminiumoxid, sin användning av optisk reflektans för att följa yt-förändringar kombinerat med röntgendiffraction för att få kompletterande atomisk kunskap om reaktionen, samt studier av guld under elektrokatalytiska reaktioner.

Acknowledgement

First of all, I would like to thank my supervisor Edvin for your support and encouragement during my PhD. Your everlasting enthusiasm when we saw something interesting and cool during our beamtimes always brightened up my day.

I would like to thank my co-supervisors, Johan Gustafson and Gary Harlow for your help during my PhD. Gary thank you for teaching me about electrochemistry and synchrotron measurements.

I would also like to thank Jonas Evertsson, Nikolay Vinogradov, Uta Hejral, Giuseppe Abbondanza, Alfred Larsson, Sebastian Pfaff, Sabrina Gericke, Lisa Rämisch and Leon Jacobse, for all your help during experiments as well as analysing of data and writing of papers.

I would also like to thank Marina Peña Díaz and Sara Barja for your help during experiments and all your hard work with the XPS and LEED measurements. I'm sorry I couldn't come to visit and learn from you as planned due to Corona.

Zbynek Novotny, thank you for all your hard work during our "remote" beamtime.

Thank you, Filip Lenrick for showing me how to polish my aluminium samples.

I would also like to thank Lidsay Merte, Johan Zetterberg, Roberto Felici, Soenke Seifert, Francesco Carla, Jacob Drnec, Andreas Stierle, Tim Wiegmann, Axel Persson, Reine Wallenberg, Crispin Hetherington, Philip Mousley, Dmytro Orlov, Zoltan Hegedues, Ulrich Lienert, Vedran Vonk, Ann-Christin Dippel, Celia Rogero and Olof Gutowski for your help with experiments, data analysis and writing of papers.

I would also like to thank all the people at SLJUS for creating a friendly and welcoming place. A special thank you goes to Tami, Hanna and Stefano for being there during both difficult and happy times. Claudiu, thank you for being a great office roommate and for all our interesting conversations. Anne Petersson Jungbeck and Patrik Wirgin thank you for all the help with administrative and economic problems. Patik Wirgin also thank you for all your friendliness and not least all your lunchtime stories, the division wouldn't be the same without you.

Lastly, I want to thank my family for all your support and love, Dad, Becca, Mum, Markus, Niclas and Mikko. Dad and Becca, you are the best dad and sister one can have, I love you both. Niclas, thanks for being there for my sister. Markus thank you for always being there for me in both good and bad times and especially for all the support you have given me during the last year, I love you with all my heart. Mum, I love you to heaven and back and I know we will meet again someday. Mikko you are the cutest dog companion one can have while writing the thesis.

Using Light to Probe Surface Electrochemical Processes

Introduction

Electrochemistry is a wide research field with many different applications where some investigated in this thesis using both *in situ* and *ex situ* studies are deposition of metals into Nano Pours Anodic Aluminium Oxide (NP-AAO) and studies of the surface changes of single and polycrystalline samples, with a main focus on gold, during Cyclic Voltammetry (CV) and potential stepping.

The electrochemical deposition of metals into the NP-AAO, a porous oxide with hexagonal ordering between the pores, can be used to grow ordered nanowires/nanostructures. These grown nanostructures will have structures that are greatly affected by the oxide template and it is therefore of great importance to understand this effect. This can be achieved by investigating the deposition process *in situ* as well as studying the nanostructures *ex situ*. The understanding of the deposition process makes it possible to create the nanostructures one desires, which can be applied as sensors [1], [2], [4]–[6], in catalysis [3], [7], [10] and for colouring aluminium products [9]. In this thesis, the electrochemical deposition of Sn, Pd and Au into NP-AAO was studied with various *in situ* x-ray techniques and *ex situ* techniques to gain a deeper knowledge about how the nanostructures grow and how the NP-AAO template affects these structures.

Another important field of research is the development of tools for investigating the electrochemical reactions occurring at the solid-liquid interface and how these reactions change the sample's surface. 2-Dimensional Surface Optical Reflectance (2D-SOR) is such a tool which have earlier been developed and applied to gas-phase reactions [15]–[18], in this thesis, the possibility to apply this technique to electrochemical reactions have been investigated. Using this technique, it is possible to image the sample through the liquid electrolyte, which shows great potentials for following surface changes, such as oxidation and reduction, during realistic reaction conditions. The combination with X-ray Diffraction studies showed the potential of the 2D-SOR to detect monolayer changes in the surface. Both single-crystalline and polycrystalline samples can be imaged with this technique, making it possible to distinguish between surface changes occurring at different grains in the sample. Using this technique processes such as corrosion (on for example steel) [12], [13] or water splitting on, for example, gold [11], [14] can be investigated.

The understanding of water splitting is of importance for the development of more sustainable energy. To get a better understanding of these reactions model systems can be used, such a system is the electrochemical reactions oxidation and oxygen evolution reactions (OER) occurring on single-crystalline gold surfaces, which have been studied with *in situ* and *ex situ* techniques in this thesis. By studying this system, better knowledge can be gained about how the surface oxidised, how the OER reaction proceeds and whether the surface promotes or poisons the reaction. Understanding how the reactions dissolve the electrode and its stability is important for understanding the water-splitting reaction, which can contribute to the development of future fuel cells. This thesis studied Au(111) during CV and potential stepping, where the surface reconstruction, the oxidation and the OER reactions have been studied. 2D-SOR and X-ray Diffraction were able to follow the surface changes *in situ* while X-ray Photoelectrons Spectroscopy was used *ex-situ* to determine the chemical species on the surface during oxidation.

Materials and elements

Single crystalline, polycrystalline and amorphous materials have all been investigated in this thesis. The different materials and their properties will be presented below. The different material systems investigated are electrochemical deposition of Sn, Pd and Au into Nanoporous Anodic Aluminium Oxide (NP-AAO) in Papers I-IV, and surface processes such as oxidation, reduction, adsorption, and corrosion of the metals Al, Pt, Pd, Au and Super Duplex Stainless Steel in papers V-IX.

Single crystals

The periodicity of a single crystal is described by the Bravais lattice, an infinite lattice with regularly spaced points [19]. By positioning a basis of atoms at the lattice points the crystal structure can be described. The lattice is defined by the basis vectors \mathbf{a}_1 , \mathbf{a}_2 and \mathbf{a}_3 , which are combined into the lattice vector \mathbf{R} , equation 1, to describe the crystal lattice [20]. In the equation m_1 , m_2 and m_3 are integers.

$$\mathbf{R} = m_1\mathbf{a}_1 + m_2\mathbf{a}_2 + m_3\mathbf{a}_3 \quad (\text{Equation 1})$$

The crystal structure will be the same even if the vectors \mathbf{a}_1 , \mathbf{a}_2 and \mathbf{a}_3 are translated by an integer multiple of any of the vectors, therefore the whole crystal can be described by translation of \mathbf{R} .

The lattice can also be described by its unit cells, which is the volume that fills the entire space when translated. The primitive unit cell contains only one lattice point and is the smallest volume used to describe the lattice, one such unit cell is the simple cubic (SC) unit cell, shown in Figure 1. However, it might not always be practical to use the primitive unit cells to describe the lattice, therefore non-primitive unit cells are used. These non-primitive unit cells include more than one lattice point and are usually more intuitive, the face-centered cubic (FCC), body-centered cubic (BCC), face-centred diamond cubic, body-centred tetragon and hexagonal close-packed (HCP) unit cells are shown in Figure 1. The FCC and BCC unit cells have all its sides equal, $a = b = c$ and the angles between the sides are all 90° ,

$\alpha=\beta=\gamma=90$. The FCC unit cell has lattice points at each corner as well as lattice points on the faces of the cell, while the BCC unit cell has lattice points in the corners as well as a lattice point in the middle of the unit cell. Metals usually have a face centred cubic (FCC) or a body centred cubic (BCC) structure, Al, Pd, Pt and Au all have a FCC structure [21]–[24]. The respective lengths of the sides for the FCC metals are 4.05 Å for Al [22], 3.89 Å for Pd [21], 3.92 Å for Pt [23] and 4.08 Å for Au [24]. Sn has two structures a $\alpha - Sn$ and a $\beta - Sn$, the $\alpha - Sn$ has a face-centred diamond cubic unit cell with the length of the sides being 6.49 Å, while the $\beta - Sn$ has a body-centred tetragonal unit cell with the length of the sides being 5.83 Å and 3.18 Å [25]–[28].

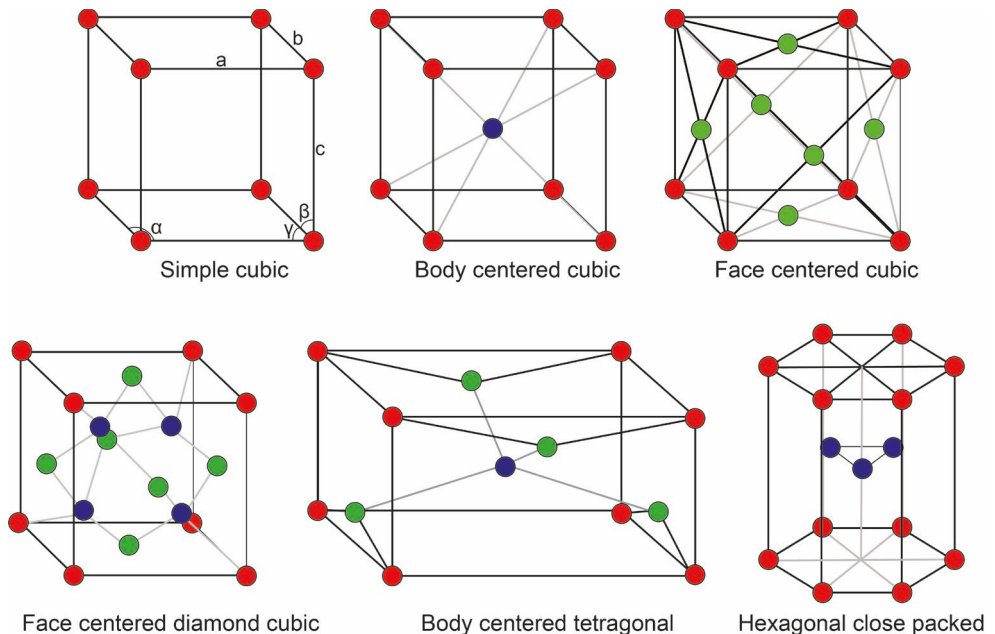


Figure 1. The unit cells for the SC, BCC, FCC, the face centred diamond cubic, the body centred tetragonal and HCP structures. The red circles are the atoms at the corners of the cells, the green circles are the atoms at the side of the cells and the blue circles are the atoms inside of the cells.

A real crystal has a termination, which is the surface of the crystal. This surface is created by cutting the crystal and depending on which direction the crystal is cut, different surfaces with specific ordering of the atoms are created. These 2-dimensional crystal planes are defined by the miller indices (hkl) [29]. The miller indices are given by the inverse intersections between the axes of the unit cell and the crystal plane. In the case for example for the (100) surface, the intersection between the plane and the axes will occur at $(1 \ \infty \ \infty)$, which will result in the miller indices $(1/1 \ 1/\infty \ 1/\infty)=(100)$. The (100), (110) and (111) surface planes of the FCC crystal with the surface unit cells indicated are shown in Figure 2.

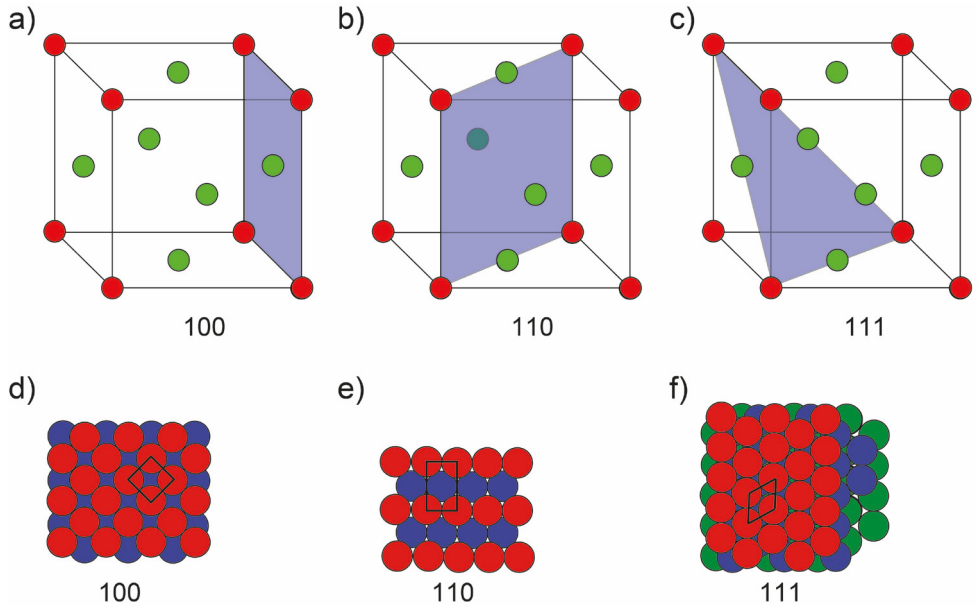


Figure 2. a-c) The respective planes through the FCC crystal, shown as the blue field in the figures. To get the respective surface structures the crystals will be cut through the indicated planes. d-f) The 2-D surface structure is shown for each respective surface, with the primitive unit cells indicated by the black lines. These structures will repeat themselves going into the crystal.

In this thesis single crystal Au and Pt samples were used, Pt was used in paper V while Au was used in papers V and VII-IX. The Au and Pt samples had a (111) and (100) surface orientation, respectively.

Reciprocal space

The reciprocal lattice is the Fourier transform of the real space lattice, which can be defined by the reciprocal lattice vector \mathbf{G} .

$$\mathbf{G} = q_1 \mathbf{b}_1 + q_2 \mathbf{b}_2 + q_3 \mathbf{b}_3 \quad (\text{Equation 2})$$

In the equation q_1 , q_2 and q_3 are integers and \mathbf{b}_1 , \mathbf{b}_2 and \mathbf{b}_3 are the reciprocal vectors that describe the reciprocal lattice [29]. The relationship between the reciprocal vectors and the real space vectors \mathbf{a}_1 , \mathbf{a}_2 and \mathbf{a}_3 are given by equation 3-5.

$$\mathbf{b}_1 = 2\pi \frac{\mathbf{a}_2 \times \mathbf{a}_3}{\mathbf{a}_1 \cdot (\mathbf{a}_2 \times \mathbf{a}_3)} \quad (\text{Equation 3})$$

$$\mathbf{b}_2 = 2\pi \frac{\mathbf{a}_3 \times \mathbf{a}_1}{\mathbf{a}_2 \cdot (\mathbf{a}_3 \times \mathbf{a}_1)} \quad (\text{Equation 4})$$

$$\mathbf{b}_3 = 2\pi \frac{\mathbf{a}_1 \times \mathbf{a}_2}{\mathbf{a}_3 \cdot (\mathbf{a}_1 \times \mathbf{a}_2)} \quad (\text{Equation 5})$$

These equations can be simplified in equation 6, in which i and j are integers.

$$\mathbf{a}_i \cdot \mathbf{b}_j = 2\pi\delta_{ij} \quad (\text{Equation 6})$$

From this, an inverse relationship between the reciprocal and real space vectors are shown, which results in small objects in real space becoming large in reciprocal space and vice versa.

Polycrystalline & amorphous samples

A polycrystalline material is composed of many differently oriented crystalline grains. These grains are typically randomly oriented in respect to each other but have a coherent atomic structure within the grain. This leads to a surface containing multiple crystallographic orientations [30], an illustration of this is shown in Figure 3. In this thesis polycrystalline Al was used in papers I-V and polycrystalline Au, Pd and Super Duplex Stainless Steel (SDSS) were used in paper VI. In the case of an amorphous material, the atoms in the material have no long-range order [30]. The NP-AAO grown on the Al samples in paper I-IV and the gold oxide in papers VII-VIII are amorphous.

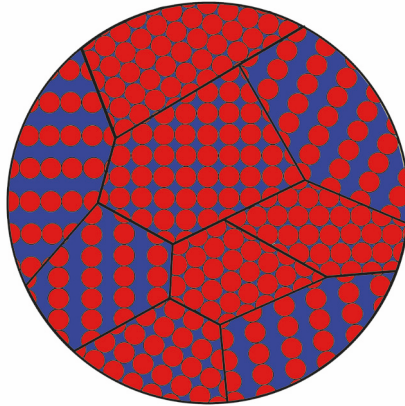


Figure 3. An illustration of a polycrystalline FCC sample. The black lines are the grain boundaries and inside of these are the grains. The grains have different surface orientations (100), (110) and (111). These grains can also be rotated as shown in the illustration.

Surface reconstruction

The termination of the crystal creates the surface as mentioned earlier and if the atoms in the surface have the same ordering and periodicity as the bulk the surface is unreconstructed. However, if the atoms in the surface layer have a different periodicity than the bulk the surface is reconstructed. The reconstruction can have the same number of atoms as the bulk layers but with a different placement or a different number of atoms than the bulk, these atoms can also have an orientation that is different from the bulk atoms. The surface reconstruction is a way for the material to minimise its surface free energy. A surface reconstruction on the sample usually occurs during specific conditions, where for example the single crystal Au(111) has a surface reconstruction both in UHV and in specific liquid environments [26], [31]–[33].

Aluminium (Al)

Aluminium is a material with low density, high strength and good corrosion resistance. Because of these characteristics, it has wide use in many products ranging from household products to transportation and constructions. Aluminium's good corrosion resistance is attributed to the formation of a protective (native) oxide layer on its surface when it is exposed to air, which hinders further oxidation of the surface [34], [35]. The native oxide will have a limiting thickness, which can be increased through electrochemical anodization [36]. This method can also be used to grow a porous oxide (a so-called Nanoporous Anodic Aluminium Oxide (NP-

AAO)) and these pores will under certain conditions become ordered [37]. An application of the porous oxide is as a template for the electrochemical deposition of ordered structures.

This thesis has investigated the electrochemical deposition of Sn, Pd and Au into the NP-AAO with the *in situ* techniques X-ray Diffraction, Grazing Transmission Small Angle X-ray Scattering, X-ray Absorption Near Edge Structure and X-ray Fluorescence in papers I-IV.

Aluminium oxides and hydroxides

The oxide which forms naturally or is grown electrochemically on aluminium is composed of aluminium oxide (Al_2O_3) and hydroxide ($AlOOH$, $Al(OH)_3$) [38]. The aluminium oxide has a lot of different structures, which are constructed from oxide blocks with either a tetrahedral, pyramidal or octahedral form. All the oxide blocks have a single aluminium atom in the middle which is surrounded by oxygen atoms, the structures are shown in Figure 4. These structures are then either ordered into an FCC or HCP (hexagonal closest packed) structure, leading to arrays of well-ordered aluminium atoms as well as a great variability in the oxide structures. All these oxides are metastable except for $\alpha - Al_2O_3$, corundum, which is thermodynamically stable. This leads to all the aluminium oxide and hydroxide structures transforming into the $\alpha - Al_2O_3$ under heat [39], [40].

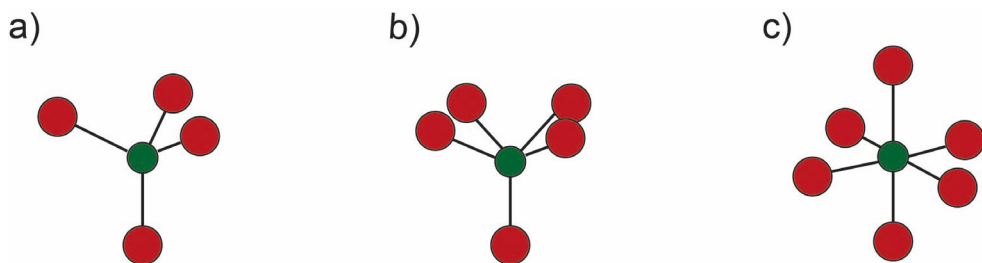


Figure 4. The oxide building blocks, the green circles are the aluminium atom and the red circles are the oxygen atoms. The tetrahedral building block is shown in a), the pyramidal building block in b) and the octahedral building block in c).

The aluminium hydroxide has a structure with stacked oxygen double layers and in between these layers positioned at the octahedral sites are the aluminium atoms. The hydrogen atoms in the structures are either connected to the oxide atoms or placed in between the layers. These hydroxides are either monohydroxides ($AlOOH$) or trihydroxides ($Al(OH)_3$) [38]–[43].

Native and barrier layer aluminium oxide

Aluminium is protected from corrosion by the formation of a native aluminium oxide on its surface when exposed to air. This oxide has a limiting thickness of 2-7 nm and is self-healing, which means that if the oxide is damaged it will be repaired with the formation of a new oxide [34], [37]. Many theories have been proposed for the formation of the native oxide and its limiting thickness [41], [44], [45], [46]. However, the most commonly used theory for explaining the native oxide growth in ambient conditions and its limiting thickness is the Cabrera and Mott theory [47].

In the Cabrera and Mott theory, positive aluminium ions are created at the metal/oxide interface and at the oxide/electrolyte interface negative oxygen ions are created. The oxygen ions are created by the adsorbed oxygen molecules on the oxide surface dissociating, some of these dissociated oxygen atoms are then ionised by the electrons which have travelled to the oxide surface from the metal/oxide interface. A (Mott) potential is established over the oxide, due to the ions formed on the separate interfaces. This potential creates an electric field in the oxide which drives the migration of ions through the oxide. The migration of the ions occurs via a hopping mechanism, where the ions move from one interstitial position or regular site to the next neighbouring interstitial site or vacancy. At each interface, the ions will react with its counterpart to grow the oxide thicker. When the oxide increases in thickness the electric field over the oxide will decrease, resulting in a slower oxide growth. This decrease in the electric field and oxide growth will continue until the electric field becomes too small to drive the ion transport through the oxide. At this time, the oxide will stop growing, and a limiting thickness is reached [47], [48].

In the case when the aluminium should be used in harsh environments, better protection can be achieved by growing the oxide thicker. This is possible with electrochemical anodization, presented in the electrochemical methods section. Anodizing in neutral electrolytes results in a homogenous oxide, which grows to a certain thickness depending on the anodization potential applied over the sample. The anodization will result in approximately a thickness of 1.4 nm/V and it is possible to grow oxides with thicknesses of up to a 1 μm [37]. The correlation between the thickness and applied potential means that the oxide will stop growing when a certain thickness is reached. This limit in thickness is explained by the resistance of the oxide (migration length of the ions) increasing with oxide thickness. Therefore a larger potential is needed to drive the migration of ions through the oxide. In Figure 5, the current response as a function of anodization time is shown for the growth of a barrier layer oxide. To achieve a thicker oxide the anodization potential can be increased, however eventually a 'breakdown potential' will be reached and at this potential and beyond the oxide will burn and crack instead of increase in thickness.

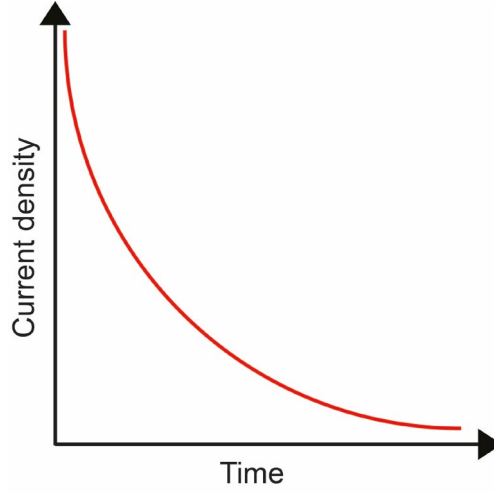


Figure 5. The current behaviour as a function of time when anodizing in neutral electrolytes and at constant potentials.

The relation between the ionic current, the potential drop and electric field over the oxide is given by equation 7 [37], [41].

$$j = A \exp(BE) = A \exp\left(\frac{B\Delta U}{t}\right) \quad (\text{Equation 7})$$

The variables in the equation are the ionic current j , material constants A and B , the electric field E , the potential drop over the oxide ΔU and the oxide thickness t .

Porous non-ordered and ordered aluminium oxide

Anodization of aluminium in an acidic electrolyte will result in a porous aluminium oxide forming on its surface, which is due to the oxide being partly soluble in acidic electrolytes [41]. The oxide that forms will have cylindrical pores, see Figure 6. These pores have a barrier layer oxide in the bottom and the oxide surrounding the pore will be in the shape of a hexagonal unit cell. The thickness of the barrier layer t_b , the pore size D_p and the interpore distance D_{int} are all linearly dependent on the used anodization potential. In the case of the barrier layer thickness, the correlation with the applied potential is 1.2 nm/V and the interpore distance is 2.5 nm/V [37]. These pore parameters will also be affected by the anions in the electrolyte and the

temperature used. A porous oxide can be grown to a thickness of several tens of micrometres, where the thickness will be determined by the total applied charge and as such the anodization time. Using specific anodization conditions, such as a specific electrolyte and anodization potential results in hexagonally ordered pores [49], [50].

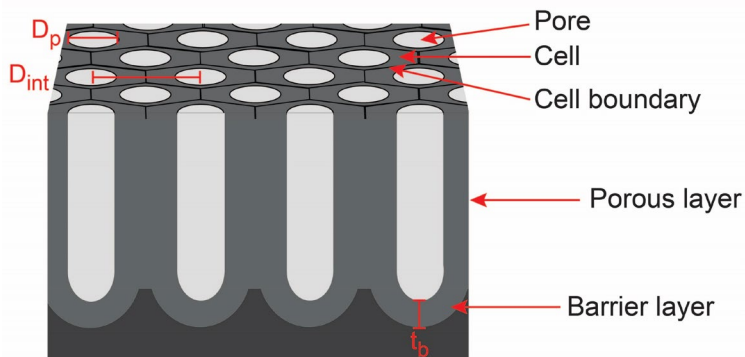


Figure 6. An illustration of the porous oxide. The pore size D_p , the inter-pore distance D_{int} and the thickness of the barrier layer t_b are indicated in the figure.

The porous aluminium oxide can be grown using either a constant potential (potentiostatic) or constant current (galvanostatic). The most common one of these is the constant potential method because of a clear correlation with the pore parameters, whereas the current parameters depend on the sample surface area. The growth of the porous oxide with a constant potential can be described by four steps, which can be correlated to the current response of the system, as illustrated in Figure 7.

In the first step of the oxide growth, a homogenous barrier layer oxide is formed. As the thickness of the oxide is increased with oxidation time, there will be a decrease in the current and the electric field over the oxide. This will lead to a minimum in the measured anodization current, see region 1 in Figure 7. At this minimum the electric field will be focused on cracks, defects and other imperfections in the oxide, leading to the start of the second step in the oxide growth, region 2 in Figure 7. At these imperfections the electrolyte can penetrate the oxide, resulting in local dissolution of the oxide and subsequently the growth of disordered pores. The barrier layer in the pores decreases in thickness, which will increase the anodising current and electric field over the aluminium oxide. The third step of the oxide growth will start when the current reaches a maximum, region 3 in Figure 7. Here the small pores either merge with the large pores or terminate, while the larger pores continue to grow [37], [51]. At this time, the pore density will decrease, which is considered the main reason for the measured current drop. In the fourth and final step, region 4 in Figure 7, the system will go towards an equilibrium morphology determined by the anodising potential, by the pores readjusting their size and spatial

arrangement. With the right anodization conditions, this can result in well-ordered pores over micrometre large domains. The pore height will increase continuously as long as the anodization is occurring [37].

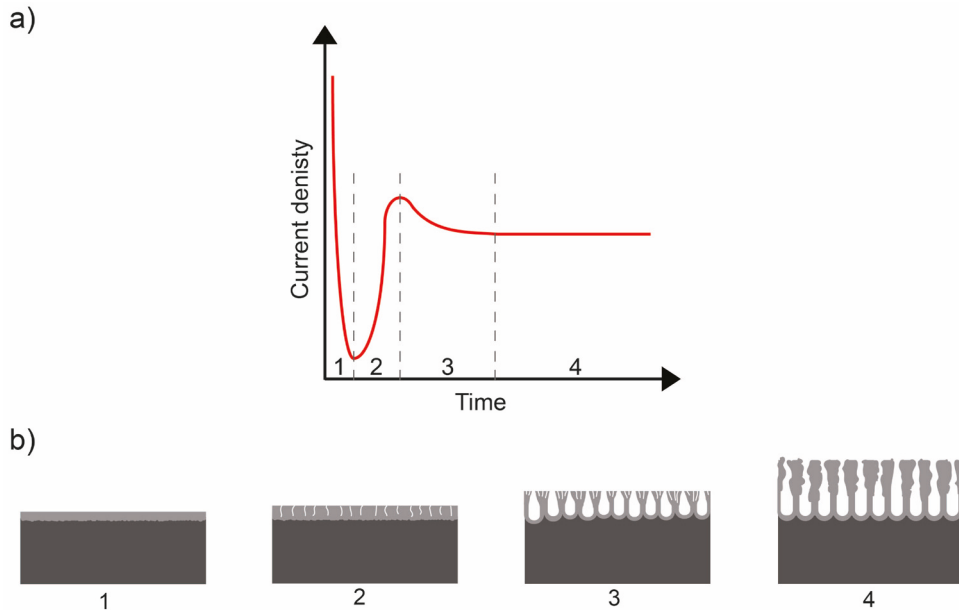


Figure 7. a) Illustration of a characteristic current curve for porous aluminium oxide growth. b) The different stages of porous oxide growth. Region 1 of the current curve and illustration 1 shows the growth of a homogenous barrier layer oxide. Region 2 and illustration 2 shows the start of the growth of unordered pores. Region 3 and illustration 3 shows the growth of the pores as they strive towards a steady-state growth. Region 4 and illustration 4 shows the steady-state growth of the porous oxide.

There exist different theories to explain the growth of the porous aluminium oxide, which can be used to model the experimental data. In all of them, the oxide is only grown on the oxide/metal interface. The reason for the lack of oxide growth at the oxide/electrolyte is because of the Al^{3+} ions reaching the oxide/electrolyte interface being ejected directly into the electrolyte instead of forming an oxide [37]. This is supported by experimental measurements where an immobile marker has been implanted into the native aluminium oxide before electrochemical oxide growth. In these studies, when all Al^{3+} ions reaching the surface contributes to the oxide growth the marker will be found 40 % into the oxide and when all Al^{3+} ions reaching the surface are ejected into the electrolyte the maker is found at the surface of the oxide. In the case of the porous oxide, the maker was found at the surface of the oxide supporting the claim that the porous oxide will only grow at the metal/oxide interface [37], [52]. In one theory the pore growth is explained by the oxide being

dissolved through an electric field-assisted dissolution at the oxide/electrolyte interface. This will result in O^{2+} ions being freed at this interface; these ions will move through the oxide and combine with aluminium at the oxide/metal interface to form aluminium oxide. The pores are then grown into the aluminium at the oxide/metal interface [53]. A second theory explains the pore growth by the expansion of the oxide, which creates mechanical stress within the oxide, and electrostriction. Electrostriction is the mechanical deformation of the oxide created by the electric field in the oxide. These processes will create a continuous transport of oxide to the pore walls from the bottom of the pores, resulting in the growth of the pores [37]. These are just theories and more knowledge is needed for understanding the exact mechanism behind the pore growth.

Masuda et al. discovered that the porous aluminium oxide could become well-ordered using specific electrolytes and anodising potentials. In 1996 he used this discovery to develop the two-step anodization method [49], [50], for creating aluminium oxides that have pores that are well ordered over several micrometres.

The two-step method anodizes the oxide in two separate steps with a chemical etch in between. The anodization conditions used, the electrolyte and the applied potential will be chosen to be the ones that create well-ordered pores. In both anodization steps, the same anodization conditions will be used. The best ordering of the pores is achieved by anodizing at potentials near the breakdown potential [54].

The first anodization step creates an oxide that is unordered at the top and well-ordered at the bottom, as explained above. The longer the anodization is conducted the more ordered the pores will become, why anodization times of up to 24 hours are used. The next step is to leave the aluminium sample with the grown oxide in a chromic-phosphoric acid etch to etch away the grown oxide. This leaves the aluminium surface with concaves from where the oxide pores were grown. The second anodization will grow pores which are guided by the concaves in the aluminium creating an oxide with well-ordered pores throughout, one name for this oxide is a Nanoporous Anodic Aluminium Oxide (NP-AAO). The anodization steps are shown in Figure 8. It is possible to control the size of the pores with the used electrolyte, anodization potential and by etching of the pores and their pore walls [55]. This well-ordered oxide has a lot of different applications, where it for example can be used for the colouration of aluminium products and as a template for growing well-ordered nanowires.

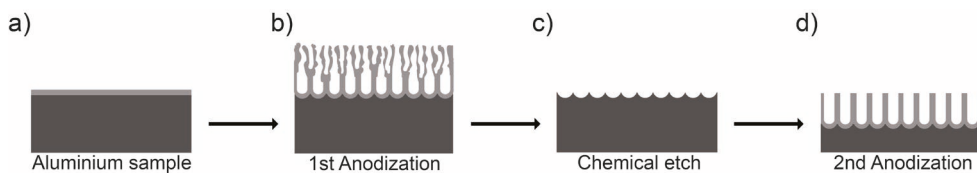


Figure 8. The two-step anodization process. a) The aluminium sample before any anodization, the light grey layer is the native oxide on the aluminium. b) The first anodization step, creating pores that are unordered at the top and ordered at the bottom. c) The aluminium sample left with concaves after the oxide has been etched away. d) The second anodization step, anodized under the same condition as the first step, leading to well-ordered pores through the whole oxide.

In this thesis ordered NP-AAO has been grown with anodization in 0.3 M oxalic acid at 40 V and 0.3 M sulphuric acid at 25 V, this gives pores with a 40 nm pore size and 100 nm pore distance and 25 nm pore size and 60 nm pore distance respectively [56], [57].

In papers I-IV, these ordered oxides have been used for electrochemical deposition of Sn, Pd and Au.

Tin (Sn)

Tin is a metal that has good corrosion resistance and electrical conductivity, why Sn nanowires are of interest for nanoscale products where they can be used for example as solders or wires. Sn is also used in the aluminium industry to colour aluminium products black [9].

In ambient conditions, Sn exists as one of two stable crystalline states, the $\alpha - Sn$ or the $\beta - Sn$ state. Their stability is dependent on the temperature where $\alpha - Sn$ is stable below 13°C and $\beta - Sn$ above 13°C. The $\alpha - Sn$ is a semiconductor and the $\beta - Sn$ is a metal. As mentioned in the Single Crystals section, the $\alpha - Sn$ has a face-centred diamond cubic structure and the $\beta - Sn$ a face-centred tetragonal structure, where the unit cell is a body centred tetragonal structure [25], [58], [59].

The deposition of Sn into NP-AAO was followed in papers I and II. In these papers the measured crystalline state of the Sn was $\beta - Sn$ and the crystalline grains in the nanorods were highly oriented with the (100) crystal orientation along the length of the pores.

Palladium (Pd)

Palladium is a material with good corrosion resistance and catalytic activity. Some applications of the metal are in catalytic converters, electronics and fuel cells, where also palladium nanowires are used [3], [60], [61]. Another application of the palladium nanowires is as hydrogen gas sensors [2], [60], [62]. Palladium is a metal with an FCC structure.

In this thesis, Pd nanowires have been grown in NP-AAO and investigated with different *in situ* and *ex situ* techniques in paper III. While CO oxidation of a polycrystalline Pd was investigated in paper VI.

Platinum (Pt)

Platinum is a metal with an FCC structure, and it is inert in air and has good corrosion resistance. It has applications as a catalyst in both gas phase and electrochemical reactions. In electrochemistry, it is, for example, used as a catalyst in proton-exchange membrane (PEM) fuel cells [63], [64], where it is used in the cell as both the anode and cathode [65]. Platinum single crystals can be used as a model catalyst, where for example *in situ* studies of the electrochemical reactions taking place on the surface will give a deeper understanding of the surface changes as well as the chemical reactions.

In this thesis, a Pt(100) single crystal has been used, this surface has a reconstruction into a hexagonal surface layer on top of the squared FCC substrate [66]. The surface changes of the single crystal were investigated with 2D-SOR during CV measurements.

Super Duplex Stainless Steel (SAF 2507)

The Super Duplex Stainless Steel (SDSS) used in this thesis is a steel produced by the company Sandvik. The steel contains both austenite and ferrite grains and has high corrosion resistance and mechanical strength. It is used in highly corrosive environments, for example in contact with seawater. It is also used for pipes for oil refining, chemical processing and mechanical components which need high strength [67].

In this thesis, the surface changes of the different grains in a SDSS sample have been followed with 2D-SOR in paper VI.

Gold (Au)

Gold is the noblest metal and one of the least reactive metals and as such has good corrosion resistance. It is used in applications ranging from fuel cells (water splitting) [14], electrical connectors, sensors and jewellery. Single crystals of Au can be used as model electrodes, since they have well-known features in CV measurements correlating with the reactions occurring on its surface, such as oxidation and reduction [11], [14], [68]. This makes them ideal for the study of surface reactions.

Au has an FCC structure and depending on which direction the sample is cut one can get different surface orientations. Two different Au samples were used in this thesis, Au(111) and a polycrystalline gold sample containing grains with different surface orientations.

Au(111)

In this thesis Au(111) single crystals have been studied under electrochemical conditions. The Au single crystal is cut along the [111] direction creating a surface with a (1x1) termination [69]. This surface is known to reconstruct in UHV under certain conditions [70], as well as under certain electrochemical conditions, for example at low applied potentials [31], [32]. The ability for the surface to rearrange and relax into the reconstruction occurs since this will reduce the surface free energy and the tensile stress of the surface, created when the bulk was cleaved [71]–[74]. However, this action is countered by the mismatch between the bulk and surface atoms occurring due to the reconstruction, leading to an increase in the surface free energy. The structure of the reconstruction is created as a balance between these two counteracting forces [71], [72]. At equilibrium, the reconstructed surface will be the crystal surface that has the lowest surface free energy.

The reconstruction of the Au(111) single crystal is hexagonally arranged and has a rectangular unit cell of $(22 \times \sqrt{3})$, shown in Figure 9. The unit cell is constructed from 23 surface atoms placed atop 22 bulk atoms in the [110] surface direction and has a width of 2 atomic rows in the [112] direction [31], [32], [69], [71]–[80]. The 23 atoms atop 22 bulk atoms are however somewhat variable [31], this is also shown in paper IX, where the unit cell change somewhat before the reconstruction lifts. The reconstruction leads to a compression of the surface layer of about 4 % compared to the bulk in the [110] direction, which in the reconstruction decreases the distance between the atoms [31], [32], [69], [73]–[75]. This mismatch between the bulk and the surface atoms, makes the position of the surface atoms shift between the FCC and HCP sites continuously with only 2-3 atoms perfectly lined up with the bulk positions. The FCC regions are somewhat larger than the HCP

regions [72]–[75], [77]–[80]. In between the HCP and FCC sites, the atoms will be positioned on bridge sites, and at these positions the compression is further increased, which leads to the atoms becoming extended from the surface, resulting in the creation of ridges. These ridges are visible as parallel rows in STM measurements of the reconstruction [73], [76], [78]–[81]. The visible ridges and the reconstruction will at certain positions (about every 250 Å) be rotated by 120° against each other creating a superstructure arranged in a zigzag pattern, which has been visualized in STM measurements. This reconstruction with three rotational domains will reduce the surface stress and create domain boundaries in the structure. The surface reconstruction is known as the Herringbone reconstruction (HB) due to this characteristic superstructure pattern.

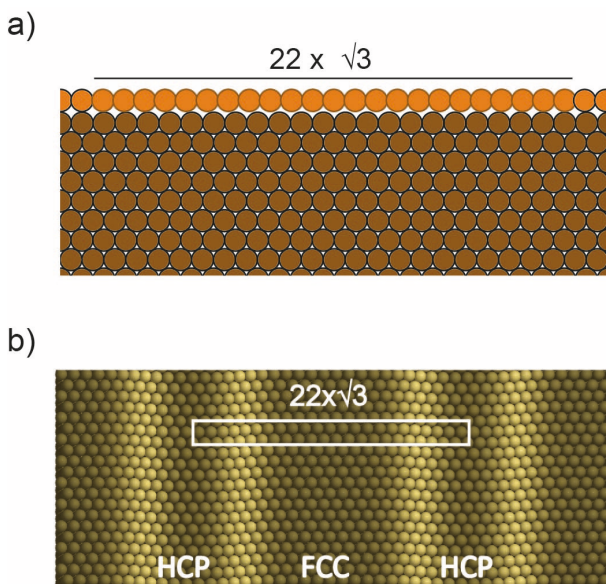


Figure 9. a) The Au(111) sample shown from the side, with the Herringbone reconstruction as the top surface layer, shown as the brighter orange atoms. The reconstruction places 23 surface atoms on top of 22 bulk atoms, the 23 surface atoms in the $(22 \times \sqrt{3})$ unit cell are indicated by the black line above the sample. b) The reconstructed Herringbone surface showed from the top of the sample, the $(22 \times \sqrt{3})$ unit cell is indicated. This image was constructed through theoretical modelling of the surface, which is presented in paper VII.

The reconstruction can be imaged and detected with a lot of different techniques, for which some are STM, LEED and SXRD and it has also been investigated by theoretical means [32], [69], [72]–[74], [78], [80].

The reconstructed Au(111) is also present during electrochemical conditions and its occurrence is dependent on the potential on the Au electrode. It will occur when the potential on the Au electrode is negative of the potential of zero charge (pzc) [32],

[69]. This reconstruction will be somewhat less ordered than the one present on the Au surface during UHV conditions. The lifting of the reconstruction in electrochemical environments will occur as the surface becomes positively charged [82]. It has been shown, that between the potential where the HB starts to lift and the potential where it is completely lifted and the unreconstructed (1x1) surface is recovered, there will appear a new surface structure [31], [32], [69], [82]. In this surface structure, the HCP regions will start to disappear resulting in a surface constructed by FCC regions and new wider dislocations. The structure has been shown to appear when the surface charge density is between -5 and $28 \frac{\mu C}{cm^2}$ [82]. Another measurement showed that the lifting of the reconstruction occurred when the surface charge density reached $0.07 \pm 0.02 \frac{e}{atom}$ [32], [69].

Au oxide and hydroxide

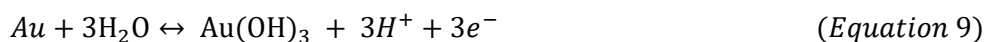
There can form oxides and hydroxides on gold under harsh conditions, the two stable and most likely to form are gold oxide Au_2O_3 and trihydroxide $Au(OH)_3$. The hydrous form of the Au_2O_3 and the $Au(OH)_3$ are considered equivalent [14]. Other oxidation structures which are also likely to form during the oxidation of gold are Au_2O and $Au(OOH)$, however these are not stable [14], [83]–[85]. Au_2O_3 has an atomic structure, where the unit cell is constructed by 40 atoms. The unit cell is created from AuO_4 units. These units have four Au-O bonds and the oxygen atoms have two different crystallographic positions in the units, one where the atoms are connected to two AuO_4 units and one where they are connected to three AuO_4 units. The cell also has an out of plane distortions of the AuO_4 units. Au_2O forms a cuprite structure, with a cubic unit cell containing six atoms. The oxygen atoms in the oxide form a body centred lattice and the gold atoms form a tetrahedron around the oxygen atoms with the Au atoms at its corners. The Au atoms have a face-centred lattice [86]. For the hydroxides, there is no wide knowledge about their exact structures, but one proposal for the $Au(OH)_3$ structure is that the gold atoms is constructed as a linear polymer, with OH groups between them, the gold atoms are also connected to two additional OH groups [87].

In electrochemistry, gold can form an oxide layer on the surface during anodic polarisation. This formation is sensitive to the crystal structure, meaning that the oxidation starts at different potentials depending on the crystals surface orientation, shown by the differences between oxide peaks in the CV curves for the different crystal surface orientations [14], [88], [89]. When the oxide is formed, it will start as a surface oxide on the sample, and at a certain potential, a bulk oxide will start to form. To be able to form this oxide the system will need to overcome an energy barrier, meaning that a high enough potential will be needed to be applied to the

system for the reaction to occur [90]. All formation of oxides on the Au surface will contribute to roughening of the Au surface and the creation of Au islands [14], [91].

Electrochemical Au oxide formation

Au(111) will form an oxide on its surface during electrochemical conditions when a certain potential is reached, for example in a 1 M HClO₄ electrolyte it was suggested that the oxide starts to form at a potential of 1.3 V [14]. The oxide can form a range of oxide structures [92], with the most stable ones being the Au₂O₃ and the Au(OH)₃. The general electrochemical reactions of Au with water to form these structure are given in equations 8-9 [14].



Below is presented three models/experiments following the oxidation of Au(111), one of these experiments, indicates anion adsorption onto the surface before oxidation [93]. All three of them indicates that there is OH adsorption onto the Au(111) surface before oxidation occurs [14], [94], [93].

One theoretical model for the formation of the oxide in a 1 M HClO₄ electrolyte with pH 1, is that at a potential of 1.05 V adsorption of OH species on the surface will start. As the potential reaches 1.17 V the surface will start to oxidize, forming a Au(OH)₃ hydroxide on the surface. During the oxide formation, some Au atoms will be freed. These atoms will either form islands on the Au surface or be incorporated into the bulk of the sample, leading to a roughening of the surface. When a potential of 1.28 V is reached the oxide changes to an oxyhydroxide Au(OOH) and at 1.54 V the oxide changes from a hydroxide to an oxide, where the most likely state is the Au₂O₃. All the stages of the oxide formation will lead to a non-ordered oxide. At a potential of 2 V [14], the oxygen evolution reaction will start, at which point there will have formed a 3 ML thick oxide on the Au surface. In this theory, the oxygen evolution starts as a decomposition of the oxide, which will release oxygen from the electrode. As this happens there will be a continued build-up of bulk oxygen, due to unstable Au(OOH) oxide decomposing to oxygen and Au₂O₃. As the potential is increased the oxygen evolution will be due to for example oxygen exchange mechanisms instead of the decomposition process [14].

In another experiment, using an electrolyte of 0.01 M HClO₄ and pH of 2, the water adlayer on the surface will turn to an OH adlayer at potentials of 1.2 V, which leads to the oxidation of the Au surface. An Au(OH)₃ oxide will be formed when the applied potential is between 1.2 V and 1.35 V. This oxide formation will change the configuration of the surface atoms of the Au, which will roughen the surface. Above 1.55 V, the surface will be composed of an Au(OOH) oxide [14], [94].

A third experiment where the reactions on the Au sample occur in 0.05 M H₂SO₄ and pH of 1 show that when performing CV measurements the HB reconstruction will be lifted at a potential of 0.31 V. After the reconstruction is lifted the surface will have become rougher due to the reconstruction containing 4 % more Au atoms than the bulk (1x1) structure. As the surface is changing from the reconstructed to the original (1x1) structure anion adsorption will occur. These adsorbed anions will at somewhat more positive potentials of 0.86 V form ordered phases on the surface. At 1.05 V, the anions will have desorbed and OH adsorption will occur and at 1.4 V the formation of an oxide on the surface will start. The oxidation will lead to roughening of the surface by the penetration of oxygen into the outermost layers of the Au crystal [93].

Our proposed Au oxide formation

In this thesis, the Au oxide formation on Au(111) has been followed using two different electrolytes 0.05 M H₂SO₄ and 0.1 M HClO₄. The oxide formation using the 0.1 M HClO₄ electrolyte was followed *in situ* with 2D-SOR and HESXRD and the oxide formation in 0.05 M H₂SO₄ was followed *ex situ* using LEED and XPS.

Using these measurements, we propose that for the case of electrooxidation using the 0.05 M H₂SO₄ electrolyte, a measurable amount of sulphate or bi-sulphate (SO₄²⁻ or HSO₄⁻) adsorb onto the Au surface at a potential of 1.6 V. Sulphate or bi-sulphate ions is well known to also adsorb at lower potentials [93], [95], [96], however, our setup is not sensitive to this earlier sulphate adsorption. The (bi-)sulphate ions adsorbed at 1.6 V, will start to desorb around 1.8 V when the peak in S 2p XPS spectra disappears. At this potential and above there will grow an oxide or hydroxide (Au₂O₃ or Au(OH)₃) on the Au surface indicated by the detection of an oxidic peak in the Au 4f spectra and a new oxide peak in the O 1s spectra. The LEED pattern is disappearing as the applied potential is going into sulphate adsorption and oxidation, indicating that the Au surface is changed from its nicely ordered crystalline structure to an unordered surface due to these processes.

From the HESXRD & 2D-SOR measurements on the Au crystal using an 0.1 M HClO₄ electrolyte, we propose that the surface will become rougher and oxidize as the oxide peak in the CV is reached, indicated by a decrease in the CTR signal and 2D-SOR reflectance. As the surface is oxidized and the CV is scanned to even

higher potentials the CTR signal disappears indicating that the surface is not a well ordered crystalline surface anymore. The reaction was brought into the OER region at which point Au powder rings appeared in the HESXRD pattern, indicating a rough and disordered surface. Our proposal of the appearance of these powder rings is that the surface of the Au crystal will start to dissolve at these high potentials and some of the dissolved Au will re-deposit onto the surface creating a rough disordered surface. It was also not possible to detect any oxide diffraction peaks in the HESXRD pattern, which indicates that the formed Au oxide is amorphous.

Electrochemistry

The field of electrochemistry focuses on chemical reactions that either generate an electrical current or use an electrical current to drive the reaction. These reactions are controlled by a potentiostat or power supply, which is supplying the driving force, the applied voltage, to the electrodes in an electrochemical cell and measuring the resulting current [97], [98]. The reaction can occur either at a solid electrolyte interface or a liquid-liquid interface and will result in a charge transfer between the two phases. At the solid electrolyte interface, the charge transfer can result in oxidation and reduction of the electrode surface and the electrolyte species, while at the liquid-liquid interface charge transfer can occur both in the form of reduction and oxidation of species and by transfer of ions between the two phases [99], [100]. Electrochemistry has many applications ranging from batteries, fuel cells, water splitting, nanowire growth to increasing corrosion resistance through for example oxide growth [9], [14], [65], [101], [102].

Electrochemical cell

Aqueous electrochemical reactions are conducted in an electrochemical cell. The driving force of these reactions is charge transfer (the exchange of electrons) between the electrode (metal) and the ions in the electrolyte (the liquid into which the electrode is inserted). This charge transfer can be explained by the Fermi level of the metal electrode and the Fermi level of the electrolyte (the electrochemical potential of the atoms/ions in the electrolyte), which will differ. The reaction wants to equalise the Fermi levels between the electrode and electrolyte, which results in a flow of electrons from the phase with the higher Fermi level to the one with the lower, creating a current in the electrochemical cell. When the Fermi levels of the two phases are equal an equilibrium will be reached, where no current will be flowing in the cell. At this position, the reaction rates of the reduction and oxidation in the cell will be equal and the measured potential over the cell will be the so-called Open Circuit Potential (OCP) [98]. These reactions which are due to the charge transfer are faradic processes, while all other reactions which do not include charge transfer are called non-faradic processes.

The reactions can either occur spontaneously in a so-called galvanic cell or need an applied potential to occur in a so-called electrolytic cell [97], [98]. In the galvanic cell, a spontaneous exothermic reaction will occur, which releases energy and creates an electrical current in the cell. In the electrolytic cell an energy, a potential, is supplied to the cell to drive the endothermic reaction. These reactions will result in a change in the Gibbs free energy ΔG of the system, and the value of this energy change can indicate whether the reaction in the cell is spontaneous or not. This change in the Gibbs free energy can be correlated to the cell potential E according to equation 10, where n is the number of electrons taking part in the reaction and F is Faraday's constant.

$$\Delta G = -nFE \quad (\text{Equation 10})$$

In the case of a spontaneous reaction, galvanic cell, the cell potential will be positive, which will result in a negative change of the Gibbs free energy. For the non-spontaneous reaction, electrolytic cell, the cell potential will be negative and the change in the Gibbs free energy will be positive [97].

The electrochemical cell is constructed by a vessel that contains an electrolyte, into which two or three electrodes, electric conductors, are submerged. To make the electrochemical reaction possible this electrochemical cell is connected to a power supply or potentiostat, which applies the potential over the cell and measures the resulting current. The electrolyte solution is composed of a solvent, most commonly a liquid, into which ions of both a supporting electrolyte and an analyte is dissolved. The supporting electrolyte is a substance that is inert during the reaction conditions but will help to increase the conductivity of the solution while the analyte is the substance taking part in the electrochemical reaction [99]. In the electrochemical cell there exist the working electrode (WE), the counter electrode (CE) and the reference electrode (RE). The reaction that is of interest occurs at the interface between the WE and the electrolyte, and the potential of this electrode will be measured against the RE. The RE will have a constant potential and should therefore be an ideal nonpolarizable electrode. The current in the cell will flow between the WE and CE. At the CE the counter-reaction of that occurring at the WE will occur, and this electrode should be chosen to be inert during the experimental conditions used. The electrodes are sometimes also referred to as anode and cathode, and in this case, the reactions occurring at these are oxidation at the anode and reduction at the cathode. The electrochemical cell can be used with either a two-electrode or three-electrode setup, shown in Figure 10 a) and b). The two-electrode setup contains only a working and reference electrode. In this setup, the potential and current are applied and measured between these two electrodes. The three-electrode setup contains the working, counter, and reference electrode. The potential in this cell is measured between the working and reference electrode, while the current is

conducted between the working and counter electrode. In the case of the reference electrode, a lot of different standard electrodes exist, some of them are the standard hydrogen electrode, the reversible hydrogen electrode and the Ag/AgCl electrode [99], [103], [104]. In this thesis both a two-electrode, papers I-IV, and a three-electrode setup, papers V-IX, have been used, the two designs of the electrochemical PEEK cells used in this thesis is shown in Figure 10 c) and d).

The electrochemical cells might also incorporate the possibility to purge the electrolyte from dissolved oxygen. Oxygen should be removed from the electrolyte since it might interfere with the reaction, react itself in the potential range used for the experiment, and because the oxygen reduction reaction will create a large current that can obscure the current one wants to measure. To get rid of this oxygen the electrolyte can be purged with an inert gas such as argon or nitrogen [99].

It is sometimes also of interest to dissolve gases into the electrolyte to investigate specific reactions with these gases. The dissolved gas can potentially react with the sample surface or it might promote or hinder the reactions occurring in the electrochemical cell.

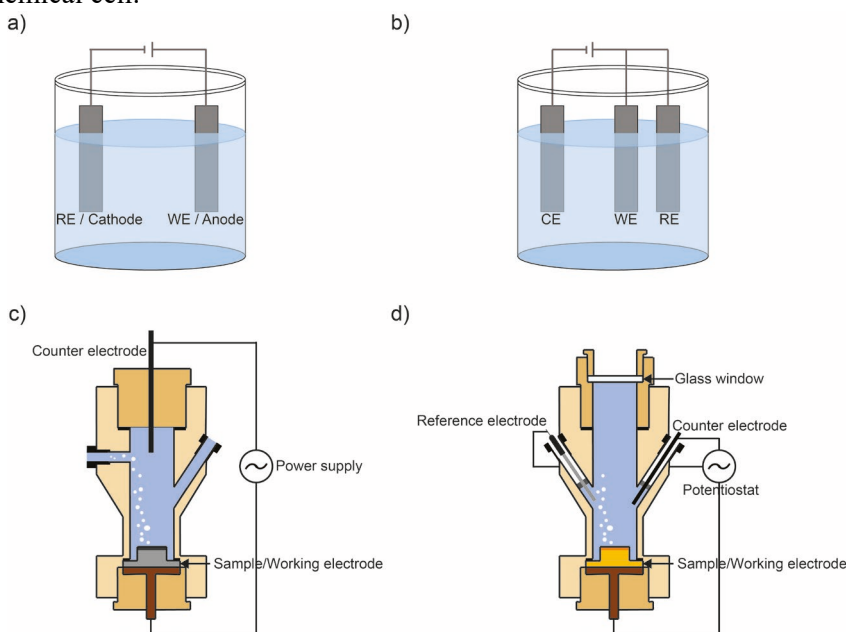


Figure 10. The different electrochemical cell designs. a) A two-electrode cell consisting of a working and a counter electrode. In this thesis, a two-electrode setup was used for the anodization of aluminium and electrochemical metal deposition. b) A three-electrode cell consisting of a working, counter and reference electrode. This setup up was used for the CV measurements of Pt(100), Au(111), polycrystalline Au and SDSS samples. c) The two-electrode PEEK cell used for anodization and electrochemical metal deposition, the aluminium was chosen to be the anode during anodization and the cathode during the electrochemical deposition process. d) The three-electrode PEEK cell used for CV measurements. In this cell design, a glass window was incorporated in the top, to make the cell compatible with 2D-SOR.

Electrochemical methods

In this thesis, we use CV, Linear Sweep Voltammetry (LSV), potential stepping/potential step voltammetry, anodization and electrochemical deposition [97]–[99]. Voltammetry methods are standard electrochemical methods used for studying electrochemical reactions, CV was used in paper V-IX and LSV was used in paper VIII. Anodization can be used to grow an oxide on the surface of the anode material, which was used in paper I-V to grow an oxide on aluminium. Electrochemical deposition can be used to either coat a surface or for example to grown nanostructures, this technique was used in paper I-IV.

Potential stepping/Potential step voltammetry

In this technique, a constant potential will be applied to the electrochemical cell and the resulting current measured. As the potential is applied instantaneously the current will respond with a peak and then a continuous decrease in current. This is because the reaction taking place on the working electrode surface will be dependent on the number of reactants that is available in the electrolyte. At the start of the applied potential the electrolyte is homogenous throughout the cell, but as the reaction is occurring the electrolyte next to the working electrode will be depleted resulting in less amount of reactants able to take part in the reaction and as such a decrease in the reaction and the produced current. The system will go towards a steady state where the rate of the reaction will be determined by the diffusion of reactants from the bulk electrolyte to the working electrode surface [98].

Cyclic Voltammetry (CV)

Cyclic voltammetry is an electrochemical technique that probes the electron transfer between electrodes and the electrolyte and as such makes it possible to follow the electrochemical process occurring in the electrochemical cell [99]. The CV will probe the surface changes as well as the electroactive species in the electrolyte [105]. The method applies a potential over the electrochemical cell and measures the corresponding current, where the current will be proportional to the electron

transfer rate. The reactions and changes on the electrode surfaces can be detected as characteristic features/peaks in the CV curve, see Figure 11 for a CV of a Au(111) single crystal. CV is a powerful technique enabling studies of chemical reactions over a large range of potentials [104].

The applied potential E during the CV is scanned back and forth between a starting potential E_i and a switching potential E_s , while the resulting current due to the applied potential is measured. The potential is changing with a scan rate v of V/s, which is the rate at which the potential is changed during the potential scan. Equation 11 gives the potential shift in the positive direction and equation 12 the potential shift in the negative direction. In these equations, t is the time for the experiment and t_{switch} is the time at which the scan direction is changed [105].

$$E = E_i + vt \quad (\text{Equation 11})$$

$$E = E_s + v(t - t_{switch}) \quad (\text{Equation 12})$$

Depending on which direction the scan is conducted the scan is called an anodic scan (the potential is scanned from low to high potentials) or a cathodic scan (the potential is scanned from high to low potentials). When performing an anodic scan and a specific potential is reached the material of the working electrode or in the solution will become oxidized, shown as a peak in the CV curve, see Figure 11. In the cathodic scan, a potential lower than that for the oxidation reaction will need to be reached before the reactant is reduced. The reduction will be shown as a reduction peak, see Figure 11.

Another way to express the potential of the electrochemical cell is with the Nernst equation, written as equation 13 [99]. This equation correlates the cell potential with the standard potential of the chemical species in the electrochemical reaction and their relative activity.

$$E = E^0 + \frac{RT}{nF} \ln \frac{(Ox)}{(Red)} = E^0 + 2.3026 \frac{RT}{nF} \log_{10} \frac{(Ox)}{(Red)} \quad (\text{Equation 13})$$

In the equation F is Faraday's constant, R is the universal gas constant, T is the temperature, n is the number of electrons taking part in the reaction, E^0 is the standard potential of the chemical species in the reaction, and (Ox) and (Red) are the relative activities of the reduced and oxidized species when the system is at equilibrium.

In the case of a one-electron transfer reaction, the Nernst equation can be rewritten as equation 14, where the activities of the chemical species can be replaced with their concentrations $[Ox]$ and $[Red]$ and the standard potential can be replaced by the formal potential E' . This version of the Nernst equation is usually easier to work with when it comes to experiments since the concentrations are easier to determine than the activities. In the case of the formal potential E' , it can be defined as the potential $E_{1/2}$ which is the middle potential between the oxidation and the reduction peaks. At this potential, the electrolyte solution right next to the working electrode contains an equal amount of oxidized and reduced species. Using the Nernst equation it is possible to predict how changes in the potential will result in changes in the concentration of the chemical species, and vice versa.

$$E = E' + \frac{RT}{F} \ln \frac{[Ox]}{[Red]} = E' + 2.3026 \frac{RT}{F} \log_{10} \frac{[Ox]}{[Red]} \quad (\text{Equation 14})$$

The current as commented above will depend on the electron transfer between the ions in the electrolyte and the atoms in the electrode, and as such the occurring reaction. There will, during a reaction be an increasing diffusion layer in the electrolyte next to the electrode due to the reacting species getting depleted, resulting in the reaction becoming diffusion-limited [105]. This diffusion layer will become thicker as the scan is progressing. The measured current is dependent on the thickness of the diffusion layer, which results in a decrease of the current with increasing diffusion layer thickness. The correlation between the current and the build-up of the diffusion layer is the reason for there being a peak for the anodic and cathodic CV scans [3]. The thickness of this diffusion layer will be determined by the scan rate, where a faster scan rate results in a smaller diffusion layer and a higher peak current. In the case of a reversible reaction, the relation between the peak current and the scan rate can be expressed by the Randles-Sevcik equation, equation 15 below.

$$i_p = 0.446nFAC^0 \left(\frac{nFvD_o}{RT} \right)^{1/2} \quad (\text{Equation 15})$$

In the equation, n is the number of electrons taking place in the reaction, F is Faraday's constant, A is the electrode surface area, C^0 is the bulk concentration of the chemical species, D_o is the diffusion coefficient of the chemical species and v is the scan rate [99].

Two features that are of interest to investigate to determine if the chemical reaction is reversible is the peak currents and the peak separation of the oxidation and reduction peaks. In the case of a reversible reaction, the peak current for the anodic and the cathodic currents will be equal. The oxidation and the reduction peaks will have a certain separation in the CV curve, which is due to the chemical species diffusing either towards or away from the electrode surface. In the case of a reversible reaction, where the equilibrium is established directly when the potential is changed, these peaks have a distance between them of $\frac{59 mV}{n}$, where n is the number of electrons taking part in the reaction [98], [104].

Some other reactions which might occur at the electrode/electrolyte interface during CV are hydrogen and oxygen evolution, oxygen reduction reaction and anion adsorption. The degree of anion adsorption is dependent on the specific anion in the electrolyte [106].

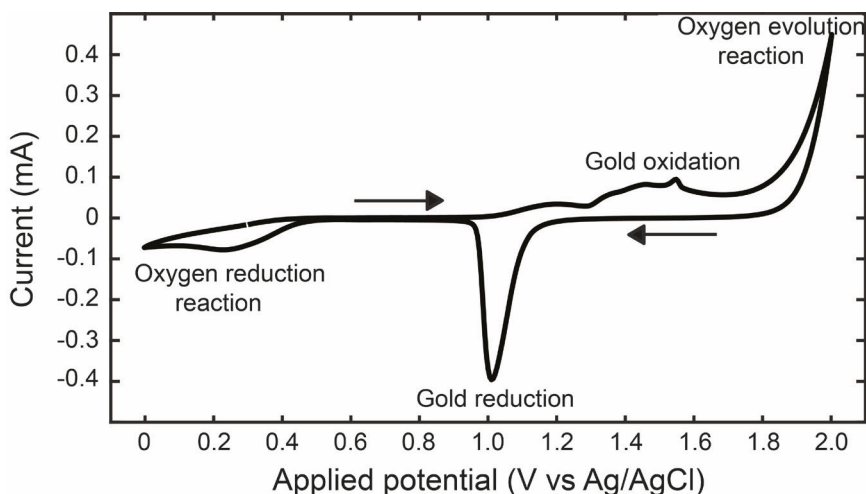


Figure 11: A CV curve for an Au(111) crystal, which also had less-well-ordered sides in contact with the electrolyte. The electrolyte was a 0.05 M sulphuric acid solution. In the CV curve, peaks for oxidation and reduction of the Au surface are indicated as well as the peak for the oxygen evolution reaction.

CV measurements were used in paper V-IX. In these papers, CV was measured on Au(111) and Pt(100) single crystals, polycrystalline Au and SDSS samples. This was combined with 2D-SOR, HESXRD, XPS and LEED measurements to image the surface changes during the CV.

Linear Sweep Voltammetry (LSV)

This is an electrochemical method that scans the potential between a starting and an end potential and measures the resulting current, much like the CV with the main difference being that the scan only goes in one direction and will not be reversed when the end potential is reached. This method uses the same electrochemical setup as for the CV and the Nernst equation can be used here as well to express the measured potential as a function of the chemical species taking part in the reaction [98].

LSV was used in paper VIII for scanning the potential into the OER region for the Au(111) single crystal.

Anodization

Anodization is an electrochemical process used for growing an oxide on the surface of the anode in the electrochemical cell. In this method, metal atoms from the anode and oxygen atoms from the electrolyte will combine to create an oxide. The oxide growth will be made possible by applying a high electric field over the electrochemical cell, which will drive the ion transport through the oxide. The metal ions and the oxygen ions will at the electrolyte/oxide and the metal/oxide interfaces combine to grow the oxide.

This process can be used to increase the corrosion resistance of aluminium by growing a thicker barrier layer oxide on the surface of the aluminium. Either a homogenous barrier layer oxide, when using neutral electrolytes, or a porous oxide, when using acidic electrolytes, can be grown on the aluminium surface [41]. The porous oxide has also been shown to grow hexagonally ordered pores under certain anodization conditions. Masuda et al. developed this porous aluminium oxide growth into a two-step anodization process to get nicely ordered pores through the whole oxide [49], [50], resulting in NP-AAO, this method is explained in the section: Porous non-ordered and ordered aluminium oxide. All of the above-mentioned aluminium oxides are illustrated in Figure 12.

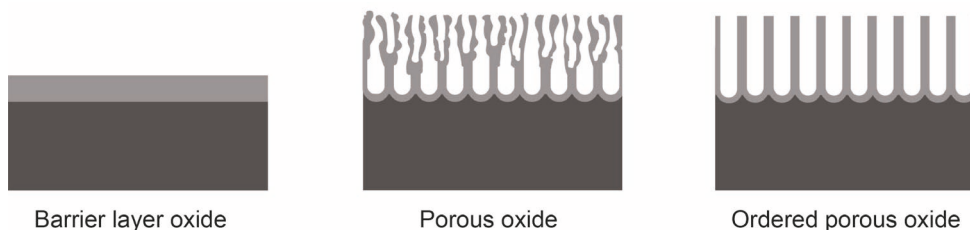


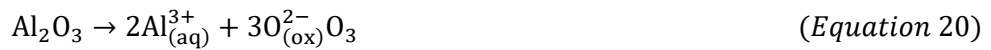
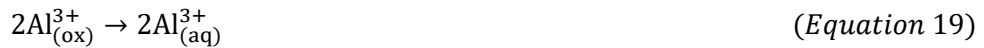
Figure 12. The different oxides grown on aluminium, the oxide is the light grey region and the aluminium is the dark grey.

The anodization and aluminium oxide growth occurs by migration of Al^{3+} , O^{2-} and OH^- ions through the oxide layer, which is made possible by the high electric field and mechanical stress in the oxide. The ions will combine at the metal/oxide and the electrolyte/oxide interface to grow the oxide, this is true for the homogenous barrier layer oxide, however, for the porous oxide, the oxide will only grow at the metal/oxide interface [41]. The reactions occurring during the anodization of aluminium are given in equation 16-24.

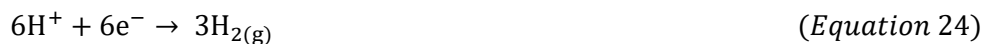
The metal/oxide reactions



The electrolyte/oxide reactions



The cathode reactions



The oxide growth will also incorporate anions of the specific electrolyte used into the oxide. In the case of sulphuric and oxalic acids which are used in paper I-IV, SO_4^{2-} and $\text{C}_2\text{O}_4^{2-}$ anions should theoretically be incorporated into the oxide at the sample/electrolyte interface after they have been adsorbed onto the surface of the sample, as either part of the oxide growth process or due to migration of the ions into the oxide due to the strong electric field over the oxide [107]. The incorporation of these anions leads to an oxide that has a layer structure, where the outer layer has anions incorporated and the inner layer is almost a pure aluminium oxide. To which extent the anions get incorporated depends on the electrolyte as well as the specific oxide, where the porous oxide has more anion incorporation than the barrier layer type. The optical, chemical and mechanical properties of the oxide will be affected by this incorporation of anions in the oxide [41], [108].

Electrochemical deposition

Electrochemical deposition (ECD) can be used for growing nanowires inside porous structures and for coating metallic surfaces. This technique uses a standard electrochemical cell that has the metal on which the deposition should occur as the cathode and the electrolyte contains the ions of the material which should be deposited. These metal ions are either dissolved into the electrolyte already before the deposition process starts or supplied via dissolution of a sacrificial counter electrode. To deposit the metal ions a potential is applied over the electrochemical cell, which will lead to reduction of the metal ions and deposition. For the deposition to run either a direct, alternating or pulsed potential will be applied over the electrochemical cell. When using an alternating or pulsed potential mode, the electrolyte solution will be replenished during the anodic pulse [109].

In the case of deposition into the porous aluminium oxide, there are some problems to overcome, such as the non-conducting barrier layer, limited diffusion of ions into the pores, build-up of charge in the barrier layer as well as cathodic side reactions, for example, hydrogen evolution, which might occur in the oxide [110]–[112]. To reduce these problems a pulsed or alternating potential deposition is favoured over direct potential deposition. A better deposition can also be achieved by attaching the porous oxide to another substrate or modifying the pores via barrier layer thinning and pore widening [110], [113]–[116]. Barrier layer thinning reduces the thickness of the barrier layer in the bottom of the pores and creates branching of the pores by

decreasing the anodization potential. This occurs due to the dependence of the barrier layer oxide thickness with the anodization potential, lower potentials give thinner oxide. The reason for the branching is also correlated with the potential, where lower potentials result in thinner pores. This branching and thinner barrier layer will result in an enhanced deposition [113], [114]. In the case of the pore widening the sample is immersed in an acid etch, this will result in some of the pore wall material being dissolved. The dissolution of the pore wall material will lead to pores that becomes wider and have a thinner barrier layer, making it easier for the metal ions to diffuse into the pores as well as for the electrons to tunnel through the barrier layer [17]. The deposition process for barrier layer thinned NP-AAO templates is illustrated in Figure 13.

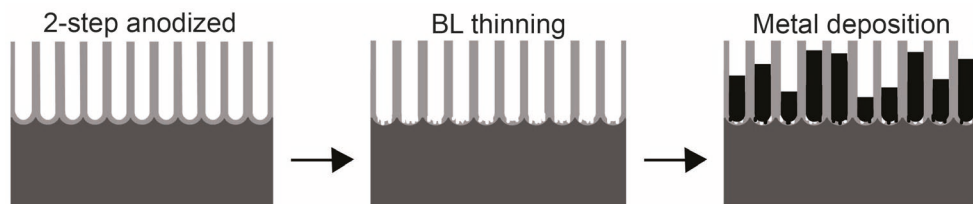


Figure 13. The deposition process illustrated from the second anodization step, through the barrier layer thinning and lastly the deposition of metal ions into the porous oxide.

In this thesis deposition of tin, palladium and gold into the NP-AAO have been investigated. The deposition of tin used an alternating voltage, the palladium and gold deposition used a combination of pulsed and alternating potentials. For the deposition of tin and palladium, the NP-AAO templates were modified using the barrier layer thinning method, while the deposition of gold used templates modified with either the barrier layer thinning or the pore widening method. The grown nanorods have been imaged with different *ex situ* techniques and an SEM image of the Sn nanorod inside of the NP-AAO is shown in the SEM section.

X-ray methods

X-rays and Synchrotrons

In 1895 W. C. Röntgen discovered x-rays, for which he received the Nobel prize in 1901. The use of x-ray has since the discovery become part of both medicine and science, making them an invaluable asset. X-rays are electromagnetic radiation, with energies between 100 electronvolts (eV) and 100 kiloelectronvolts (keV) and wavelengths in the Ångström range (10^{-10} m). The wavelength and energy of the x-rays are inversely proportional, expressed with equation 25, where E is the energy of the x-rays, λ is the wavelength of the x-rays, h is Planck's constant, and c is the speed of light.

$$E = \frac{hc}{\lambda} \quad (\text{Equation 25})$$

X-rays will penetrate deep into a material and interact with the electrons through scattering or absorption. Scattering of the x-rays leads to either elastic (no energy loss) or inelastic (energy loss) scattering and can be used for investigating different material properties. Absorption leads to the x-ray energy being absorbed by an electron, resulting in the excitation of the electron. The electron might either excite to a higher energy shell or become ejected from the atom, which is the principle of the photoelectric effect. The excitation of the electron leaves behind a core hole, this will be filled by an electron from a higher energy electron shell. The energy difference between the electron and the core hole will be emitted as either a fluorescent x-ray or as an auger electron.

The x-rays can be produced either by an x-ray tube or in a synchrotron. The x-ray machines at hospitals and in research labs use x-ray tubes. These work by heating a filament that will emit electrons. These electrons will then be accelerated onto an anode, which will result in x-rays as they collide. Two types of x-rays will occur Bremsstrahlung and characteristic x-rays. Bremsstrahlung occurs because of the deceleration of the electrons as they hit the anode. Characteristic x-rays occur due to the electrons that collide with the anode ejecting a core electron and creating a core hole, the core hole will be filled by an electron from an outer electron shell.

The energy difference between the core-shell and the outer shell will be emitted as a characteristic X-ray, which will have an energy that is characteristic of the material of the anode. These x-rays have a specific energy that is not possible to tune and will have a lower intensity than the x-rays produced in synchrotrons.

Today's synchrotrons are third and fourth generation, in which narrow x-ray beams with high intensities are produced. The x-rays are produced through the circulation of electrons inside a storage ring. These electrons travel at relativistic velocities and at the sections of the storage ring, bending magnets, wigglers and undulators, where there is a magnetic field the electrons will change their travelling direction. This change in travelling direction will result in an energy loss of the electrons, which will be emitted as x-ray radiation that travels in the forward direction in which the electrons originally travelled. The bending magnets will change the general travelling direction of the electrons, while wigglers and undulators oscillate the electrons while its general travelling direction is unchanged. The x-rays will travel onward into so-called beamlines. At the end of the beamline, there will be the experimental station, where the x-rays are used for the desired experiment. The beamline is constructed with apertures, slits, gratings and monitors to modify and control the x-ray beam. The first step of the beamline is the monochromator which is used to control the bandwidth/energy of the x-rays. Thereafter the x-rays are focused, the two kinds of mirrors used for this focusing are the K-B mirrors and the Fresnel Zone plates. Focusing of the x-rays with the curved K-B mirrors occurs by the x-rays impinging onto them at a grazing incidence angle and being reflected. The focusing of the x-rays with the Fresnel Zone plates is instead through diffraction of the x-rays as they pass through the circular plate. These plates are constructed by alternating absorbing and transparent materials, making the diffraction occur at the interface between these materials. After this step, the x-rays are shone onto the sample and detected with a detector after the interaction with the sample. This gives information about the experiment, for example, its structure or the reaction occurring.

The x-rays can penetrate deep into materials, as mentioned earlier, which makes them a good tool for investigating electrochemical reactions at surfaces. In this thesis x-rays have been utilised for the investigation of nanoporous aluminium oxide growth, electrochemical deposition into these porous oxides, CV measurements of Au(111), polycrystalline Au and Super duplex stainless steel and LSV measurements of Au(111). In this thesis, the x-ray techniques used to follow these reactions are Grazing Incidence Transmission Small-angle X-ray Scattering (GTSAXS), X-ray Fluorescence (XRF), X-ray Absorption Near Edge Structure (XANES), X-ray Diffraction (XRD), Surface/High Energy Surface X-ray Diffraction (SXR/HESXR) and X-ray Photoelectron Spectroscopy (XPS).

The measurements in the different papers were conducted at different synchrotrons, which synchrotron and beamline that were used for each paper are shown in Table 1, as well as which research is typically conducted at that beamline. Papers V, VI

and VIII did not use synchrotron measurements and are therefore not included in the table.

Paper	Synchrotron	Beamline	Research
Paper I	Argonne Photon Source (APS) in Argonne, USA	12-ID-C	Small angle X-ray scattering measurements.
Paper II	ESRF in Grenoble, France	ID31	Interface and material studies with high energy x-rays.
Paper III and IV	Diamond Light Source, Didcot, United Kingdom	I07	X-ray diffraction at surfaces.
Paper VII	DESY in Hamburg, Germany	P21	Material science using x-ray energies between 40-150 keV.
Paper IX	DESY in Hamburg, Germany	P07	Material science using high x-ray energies.

Table 1. The table shows which synchrotron and beamline were used for the measurements in each paper as well as what kind of research/measurements those beamlines focuses on.

Grazing incidence angle geometry

X-ray measurements can with a small enough incidence angle between the sample surface and the x-rays become sensitive to the near-surface region of the sample. This is possible because the refractive index n for most materials is negative for x-rays, making total external reflection at small enough grazing incidence angles possible when the x-rays go from a less dense to a denser material.

The refractive index is given in equation 26, where n is the refractive index, δ the dispersion coefficient and β the absorption coefficient. δ and β are both small values.

$$n = 1 - \delta - i\beta \quad (\text{Equation 26})$$

The penetration depth of the x-rays will decrease with the incidence angle, making the measurement more surface sensitive when a smaller incidence angle is used. Because of this, measurements using small incidence angles of the x-rays onto the sample which are near or below the critical angle of total external reflection (α_c) for the investigated material are very sensitive to the surface region [117].

For the scattering of the x-rays which has impinged onto the sample, the scattering wave vector \mathbf{q} divided into each (x,y,z) direction is expressed in equations 27-30 and illustrated in Figure 14. In the equations, k_0 is the magnitude of the wave vectors \mathbf{k} and \mathbf{k}' , $2\theta_f$ is the in-plane scattering, α_f is the scattering angle between the scattered x-ray beam and the samples surface, α_i is the incidence angle between the x-ray beam and the samples surface and λ is the x-ray wavelength [118]–[120].

$$q_x = k_0[\cos(2\theta_f) \cos(\alpha_f) - \cos(\alpha_i)] \quad (\text{Equation 27})$$

$$q_y = k_0[\sin(2\theta_f) \cos(\alpha_f)] \quad (\text{Equation 28})$$

$$q_z = k_0[\sin(\alpha_f) + \sin(\alpha_i)] \quad (\text{Equation 29})$$

$$k_0 = \frac{2\pi}{\lambda} \quad (\text{Equation 30})$$

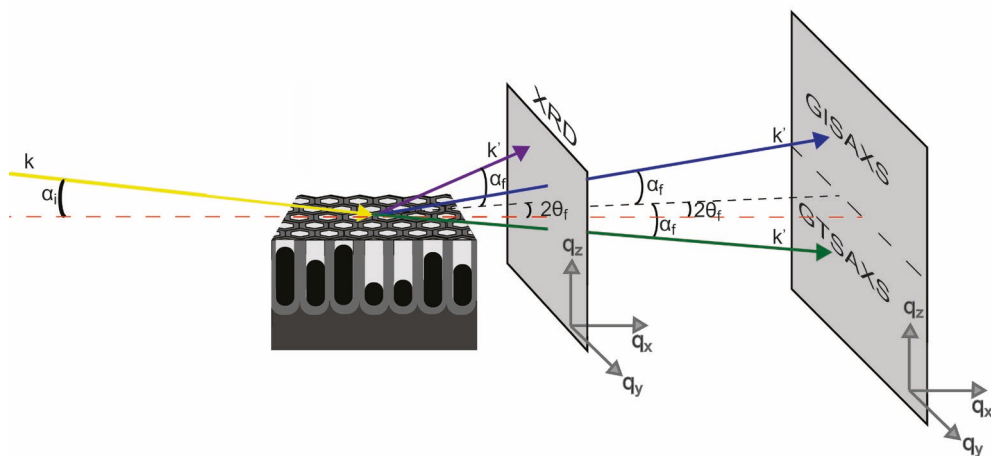


Figure 14. The experimental setup using grazing incidence angles for XRD, GISAXS and GTSAXS, used in papers I-IV, VII and IX. The image illustrated is the NP-AAO sample, however, the same XRD setup applies to the Au(111) sample.

X-ray diffraction (XRD)

XRD is used to investigate and determine a materials atomic structure. The method shines x-rays onto a sample where they interact through elastic scattering with the electrons. In the case of an ordered and periodic atomic structure the scattering of the x-rays will lead to constructive interference and as such a detected maximum intensity in specific directions. These measured maximum intensities are called diffraction peaks or Bragg peaks, and together they create the so-called diffraction pattern. In the case of a crystalline structure, well-defined peaks are shown in the pattern. A sample that is constructed from many small crystalline grains, such as a polycrystalline sample, will instead lead to diffraction in many different directions which are corresponding to the directions where the diffraction conditions are met for the respective grains. This leads to diffraction of the x-rays which will spread out from the sample as (Debye-Scherrer) cones. At the position where these cones intersect the detector, a diffraction pattern in form of (powder) rings will be detected. The possibility to measure a diffraction pattern of the atomic structure is due to the x-ray wavelength being smaller than the distance between the atomic planes. This leads to the use of x-rays with energies between 5-100 keV [20]. The diffraction pattern is the projection of the reciprocal space structure of the real space atomic structure and can be used to obtain the real space atomic structure through modelling or a Fourier transform.

Two separate (but equivalent) conditions or laws are used for explaining XRD, the Laue condition, and the Bragg's law, developed in the beginning of the 20th century by M. von Laue and W.H. Bragg and W. L. Bragg respectively [20], [29].

The Laue condition describes the occurrence of the diffraction peaks by the interference of x-rays scattered from two atoms. Figure 15, shows the geometry used to derive the Laue conditions.

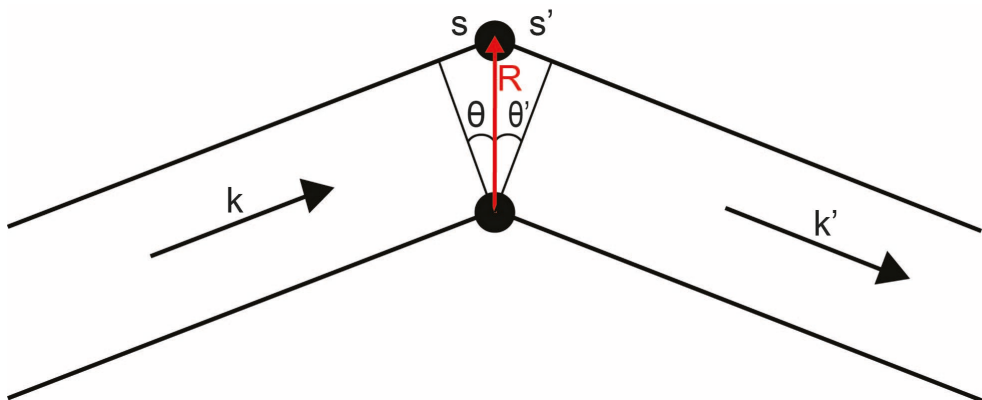


Figure 15. The Laue condition, where the x-rays are scattered from two atoms to create interference and diffraction peaks.

In the Laue condition the incoming \mathbf{k} and outgoing \mathbf{k}' x-ray wave vectors have equal magnitude (since Bragg diffraction is due to elastic scattering), given earlier in equation 30.

The two atoms in the Laue condition have a distance between them of \mathbf{R} , which is the real space lattice vector. There is a path difference (PD) between the x-rays scattered at the separate atoms. The PD will be the sum of the difference in travelling path s for the incoming and s' for the outgoing x-ray wave, with the angles θ for the incoming and θ' for the outgoing wave, as shown in Figure 15. This PD is expressed in equation 31, where \mathbf{k} , \mathbf{k}' and $\Delta\mathbf{k}$ are wave vectors and k is the magnitude of the wave vectors.

$$PD = s + s' = \mathbf{R} \cos \theta + \mathbf{R} \cos \theta' = \frac{\mathbf{k} \cdot \mathbf{R} - \mathbf{k}' \cdot \mathbf{R}}{k} = \frac{\mathbf{R} \cdot \Delta \mathbf{k}}{k} \quad (\text{Equation 31})$$

To achieve constructive interference, the PD for the scattered x-rays needs to be an integer of the x-ray wavelength, λ . This correlation between the PD and the wavelength is expressed in equation 32, where n is an integer.

$$PD = n\lambda = n \frac{2\pi}{k} \quad (\text{Equation 32})$$

By combining equation 31 and 32, the equation for constructive interference for the scattering can be derived, given as equation 33. In the equation, \mathbf{R} is the real space lattice vector, $\Delta\mathbf{k}$ is a wave vector and n is an integer. Fulfilment of this equation will lead to diffraction by the Laue condition.

$$\mathbf{R} \cdot \Delta \mathbf{k} = 2\pi n \quad (\text{Equation 33})$$

For diffraction, and constructive interference, to occur by this condition the $\Delta\mathbf{k}$ vector needs to be equal to the reciprocal lattice vector \mathbf{G} , as shown below. $\Delta\mathbf{k}$ can be expressed as equation 34, where h , k and l do not have to be integers.

$$\Delta\mathbf{k} = h\mathbf{b}_1 + k\mathbf{b}_2 + l\mathbf{b}_3 \quad (\text{Equation 34})$$

Constructive interference in a lattice is then given by equation 35, where \mathbf{R} is the real space lattice vector, n , m_1, m_2 and m_3 are integers, $\mathbf{b}_1, \mathbf{b}_2$ and \mathbf{b}_3 are the reciprocal vectors and $\mathbf{a}_1, \mathbf{a}_2$ and \mathbf{a}_3 are the real space vectors.

$$\begin{aligned} 2\pi n &= \Delta\mathbf{k} \cdot \mathbf{R} = (m_1\mathbf{a}_1 + m_2\mathbf{a}_2 + m_3\mathbf{a}_3) \cdot (h\mathbf{b}_1 + k\mathbf{b}_2 + l\mathbf{b}_3) \\ &= 2\pi \cdot (m_1h + m_2k + m_3l) \quad (\text{Equation 35}) \end{aligned}$$

From this equation 36 is attained.

$$(m_1h + m_2k + m_3l) = n \quad (\text{Equation 36})$$

For equation 35 and 36 to be valid and constructive interference to occur h, k and l need to be integers, which gives that $\Delta\mathbf{k} = \mathbf{G}$, meaning that $\Delta\mathbf{k}$ is a reciprocal lattice vector during these specific conditions. This $\Delta\mathbf{k}$ lattice vector describes a specific lattice point that is measured due to a specific orientation between the x-ray beam, the sample and the detector.

The interference of the detected x-rays can be visualised with the Ewald sphere, Figure 16 shows the Ewald sphere in 2D, in this construction \mathbf{k} is the wave vector that originates from the centre of the Ewald sphere and points at a reciprocal lattice point. The magnitude k of this \mathbf{k} wave vector is the radius of the Ewald sphere. The Ewald sphere will describe which lattice points in reciprocal space can be measured at a specific orientation between the x-ray beam and the reciprocal lattice, by moving the detector. By rotating the sample so that a specific lattice point falls onto the Ewald sphere and moving the detector to the specific \mathbf{k}' direction it is possible to detect the diffraction in that direction [20].

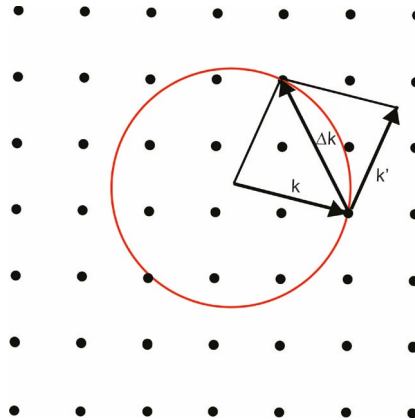


Figure 16. An illustration of the Ewald sphere in the reciprocal lattice.

Another equivalent construction of the diffraction condition is as mentioned the Bragg's law [29], here a plane x-ray wave impinges onto the sample crystal planes. The incidence and exit angle for the x-rays onto the sample is θ , as shown in Figure 17, which shows the scattering geometry.

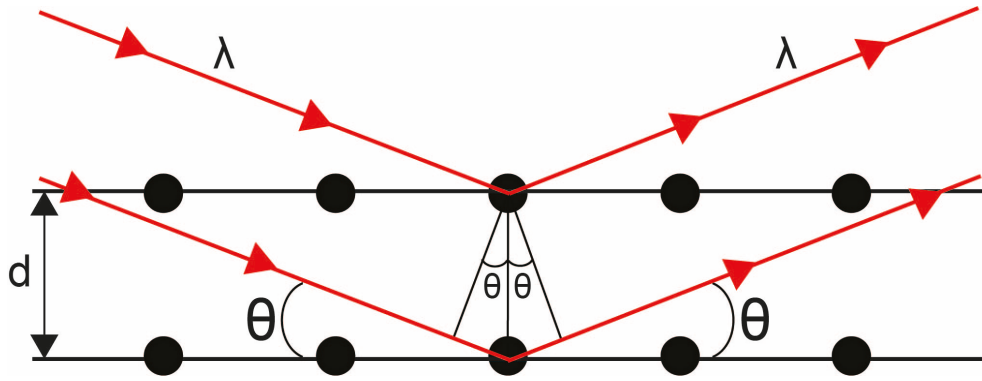


Figure 17. The scattering geometry used for Bragg's law. The x-rays will scatter on the atomic planes and interfere under the specific conditions defined by Bragg's law.

The scattered x-rays from the two planes will have a PD between them, and constructive interference occurs when the PD is a multiple of the x-ray wavelength. This can be expressed with Bragg's law defined in equation 37, where d is the distance between the atoms in the sample, θ is the incidence or exit angle, n is an integer and λ is the x-ray wavelength.

$$2d \sin \theta = n\lambda \quad (\text{Equation 37})$$

Surface X-ray diffraction (SXR D)

SXR D is a version of XR D used for investigating a samples surface structure. It can be used for determining the crystallographic surface structure and surface reconstructions, as well as to follow surface changes during reactions. In this technique, the detected diffraction signal will be a combination of the bulk and the surface diffraction signals, where the intensity of the diffraction from the surface is many orders of magnitude smaller than the signal from the bulk [117]. Due to this, usually intense x-ray radiation is needed to get a good enough signal from the surface, which is why synchrotron measurements are used [121].

The detected SXR D diffraction pattern can be explained as a combination of the diffraction from the bulk and the surface, see Figure 18. A 2D structure has a periodic structure horizontally in the plane but is finite in the vertical out of plane direction. Due to this, the Fourier transform of the structure and as such the diffraction pattern will result in lattice rods of continuous intensity which are perpendicular to the surface of the sample [122], [123]. If this 2D structure is the surface of a material and has the in-plane periodicity of the bulk, the lattice rods will pass through the Bragg reflections. This will result in a combined signal of the lattice rod and the Bragg reflections which is called a Crystal Truncation Rod (CTR). The CTR signal is sensitive to both the bulk and the surface structure, where the Bragg reflections determine the bulk structure and the signal in between the Bragg peaks gives the surface information. The part of the CTR which is the most sensitive to the surface is the position in the middle between two Bragg peaks [124]. In the case the top atomic layer has a different periodicity than the bulk the diffraction of the x-rays will occur in a slightly different direction compared to the bulk. This will result in diffraction rods with a continuous intensity, these are called superstructure rods or superlattice rods (SLR). These rods have a different periodicity than the bulk reflections and do not go through any Bragg reflections, they give information about the atomic structure of the reconstructed surface [121].

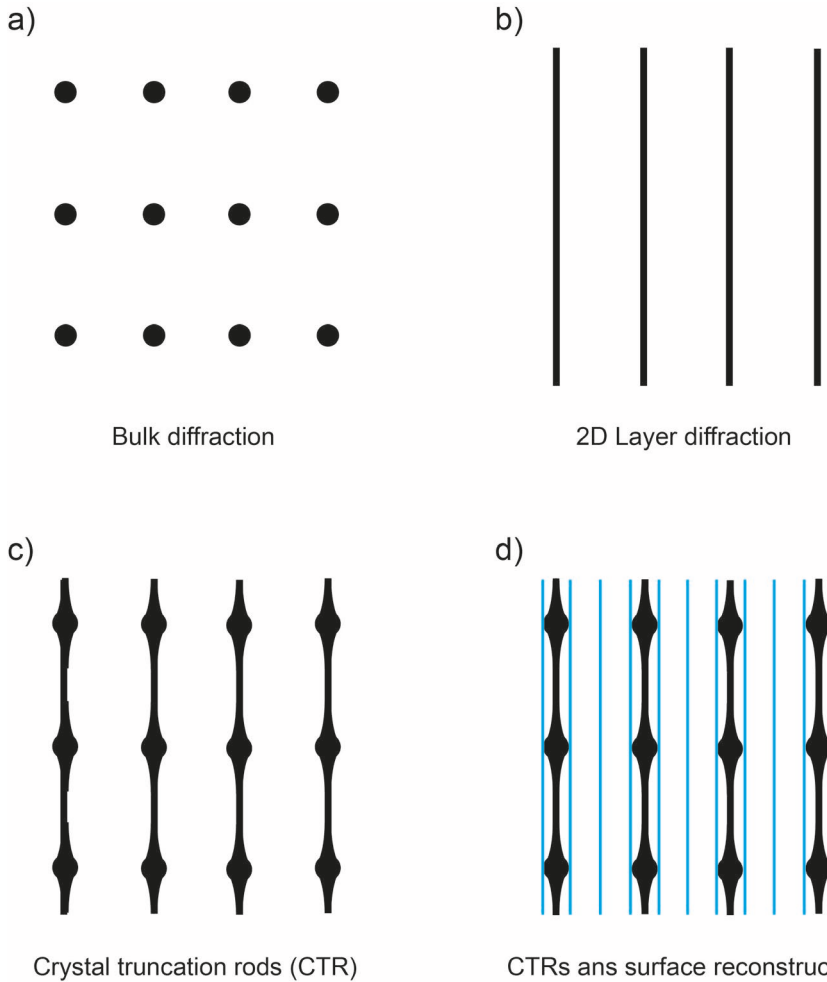


Figure 18. The different XRD diffraction patterns. a) The diffraction from a bulk sample, where the black circles are the Bragg peaks. b) The diffraction pattern from a 2D layer, here the diffraction is in the form of continuous lattice rods. c) The diffraction from a terminated bulk resulting in CTRs. In this case, the surface has the same ordering as the bulk and the lattice rods pass through the Bragg peaks. These CTRs have more intense scattering at the position of the Bragg peaks and lower intensity in between them. d) The diffraction pattern from a terminated bulk where the top surface layer has a reconstruction, meaning the surface ordering is different from the bulk. This leads to a diffraction pattern containing the CTR signal as well as a separate signal for the surface layer (the blue lattice rods, so-called superlattice rods). Due to the surface layer being a single atomic layer the lattice rods will have a continuous intensity.

The SXRD measurement is performed by shining x-rays with a small incidence angle onto a flat and smooth sample surface and detecting the diffracted x-rays. The small incidence angle will lead to an enhancement of the surface diffraction and a reduction of the bulk signal. Traditional SXRD measurements use x-ray energies

between 10-30 keV and small detectors. When probing the whole of the reciprocal space to determine the surface structure, the detector has to be moved around the sample and the sample needs to be tilted and rotated to meet the diffraction conditions, which is due to the curvature of the Ewald sphere. In this case when the detector is moved close to or onto a Bragg peak the intensity of the x-ray beam will be lowered to not saturate the detector.

It is also possible to image the SXRD signal with large 2D-detectors, where a full plane of reciprocal space can be measured at once. By rotating the sample, a 3D map of the reciprocal lattice for the material can be constructed [121]. The possibility to probe a large part of reciprocal space with just a single detector image makes this a useful method to follow the reactions on the sample's surface [125]. Because of the intensity difference between diffraction from the bulk and the surface, the Bragg peaks are usually blocked by beam stoppers, placed on the detector, when the surface changes are of interest. In the case when higher x-ray energies are employed, smaller incidence angles will be used, and a flattening of the Ewald sphere will occur. This will make the detected CTR signals into almost straight lines on the detector. When energies around 70-80 keV are used the SXRD technique is called High Energy Surface X-ray Diffraction (HESXRD) [126]. This method (HESXRD) was used to follow the surface changes of Au(111) both during CV and stepping of the applied potential to the electrochemical cell. The setup used for these measurements is shown in Figure 19.

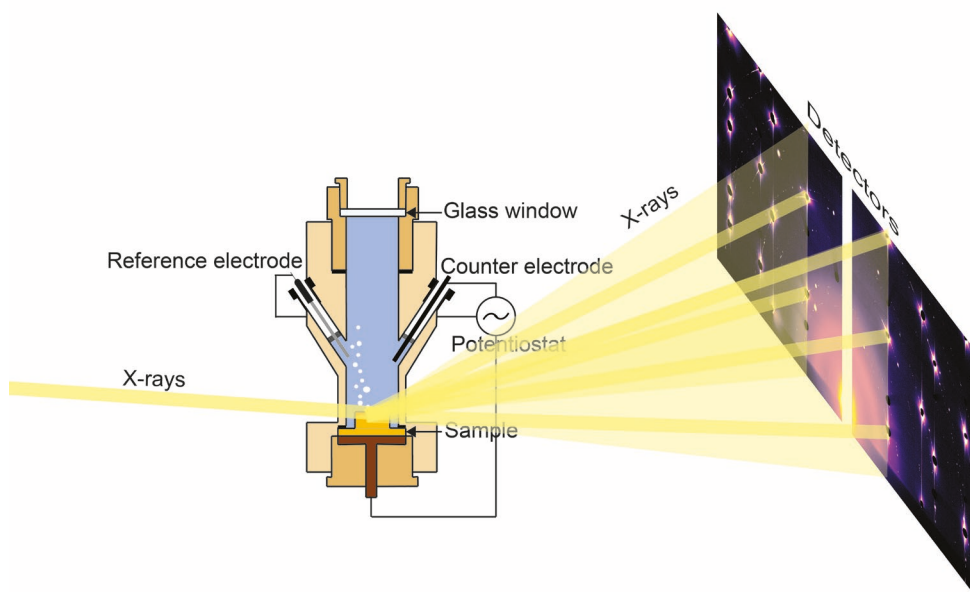


Figure 19. The experimental setup used for the XRD measurements of Au(111). The X-rays shines onto the sample inside of the electrochemical cell and are detected with either a single (paper IX) or two detectors (paper VII).

The measured HESXRD pattern during CV is shown in Figure 20, it shows the characteristic diffraction of Au(111). At the position of the Bragg peaks, beam stops are placed on the detector resulting in the black circles in the XRD pattern. The CTR signal is detected in between the Bragg peaks. The SLR signal due to the reconstructed Au(111) Herringbone (HB) surface is detected next to the CTR signal. The reason for the shift between the CTR and SLR is that the HB has a smaller lattice constant in real space than the bulk of the Au(111), which will result in a somewhat larger reciprocal lattice constant, why the SLR is detected next to the CTR. The dynamics of the lifting and reconstruction of the Herringbone reconstruction of Au(111), is followed in paper IX, where it is possible to see how the superstructure rod is disappearing and appearing as the reconstruction is lifted and reconstructed.

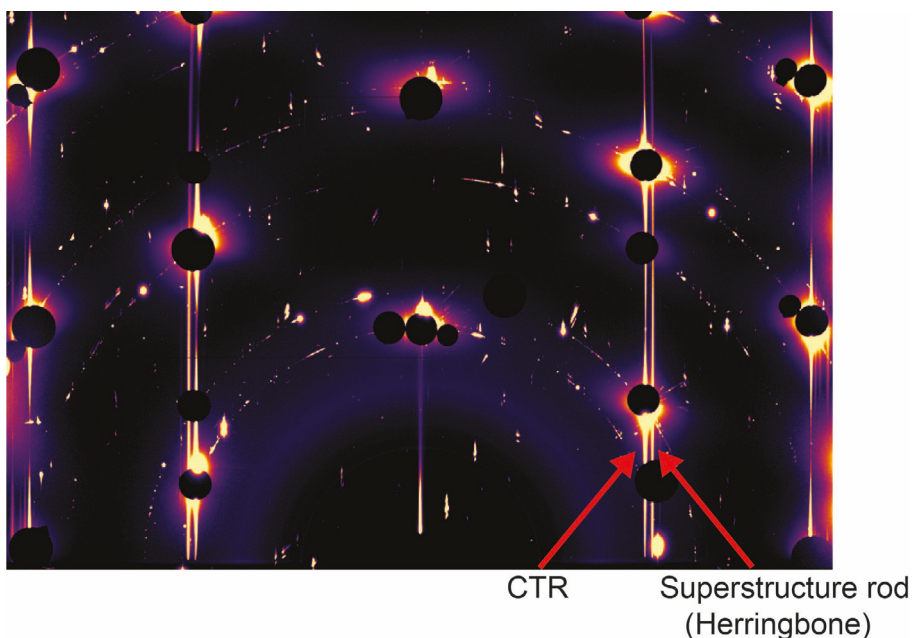


Figure 20. A HESXRD image of the Au(111) surface, when performing CV in an 0.1 M HClO₄ electrolyte. The Bragg peaks are covered with beams stop shown as the black circles in the image. In between these Bragg peaks are the CTR signals, one of the CTRs is indicated in the image. The signal due to the Herringbone reconstruction is shown as a superstructure rod, one of them is indicated in the image. This signal is not going through the Bragg reflections, due to the different structure of the surface compared to the bulk. It is possible to see how this superstructure rod is disappearing as the surface reconstruction is lifted.

The measured HESXRD pattern during potential stepping is shown in Figure 21, where four different XRD patterns are shown for the Au(111) at certain applied potentials. At a potential of -0.2 V the Herringbone reconstruction is present on the Au(111) surface, this signal is hard to detect in the shown XRD pattern due to the

sample not having an optimal surface since the sample had been used in other experiments before this one. The CTR signal is clearly visible in between the Bragg peaks. In the XRD pattern measured at a potential of 0.6 V there is only the CTR signal present, indicating that the HB reconstruction has in this case been lifted before this potential is reached. As the potential is stepped to 1.9 V, where the Au surface should be oxidized, the CTR signals are disappearing, this is due to the surface becoming less ordered and rougher as well as the presence of the oxide. At 2.2 V, where the reaction is in the OER region, Au powder rings appear in the diffraction pattern going through the Bragg peaks, these are due to the surface becoming unordered, which could be due to some of the Au being dissolved and redeposited onto the surface [127]. At the potentials of 1.9 V and 2.2 V the Au surface should be oxidized, shown by new O 1s and Au 4f peaks in the XPS spectra measured in paper VIII. If the oxide would have been ordered there would have been new diffraction spots/rings in the XRD pattern. No such peaks are observed suggesting the formation of an amorphous oxide. The possibility to follow the surface changes with the XRD measurements are of great value for understanding how the electrochemical reaction changes the surface. These measurements as well as the XRD signals measured during CV cycling has been combined with 2D-SOR and XPS measurements in paper VII and VIII.

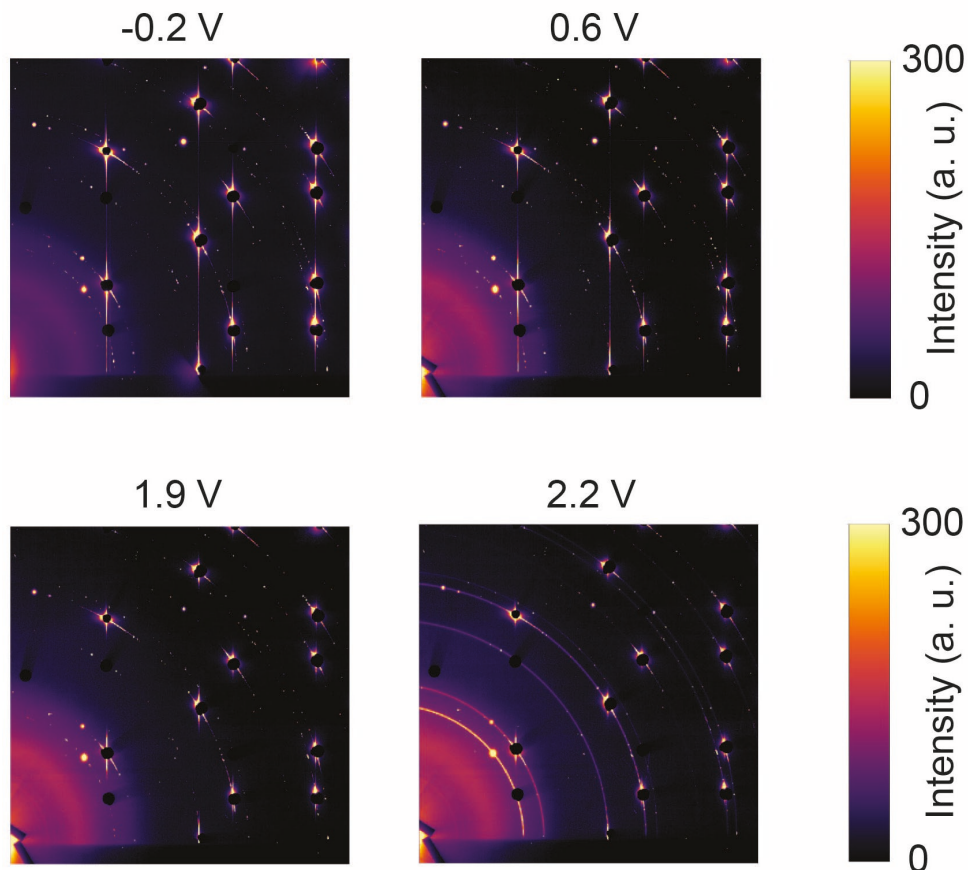


Figure 21. The XRD pattern for the Au(111) surface during four different applied potentials over the electrochemical cell using an 0.1 M HClO_4 electrolyte. The Bragg peaks are covered by beam stops, resulting in the black circles in the images. The CTRs are shown as bright lines in between the Bragg reflections in the images for the applied potentials of -0.2 V and 0.6 V. At 1.9 V the CTR signal is reduced due to the surface becoming less ordered and at 2.2 V Au powder rings can be observed. At 1.9 V and 2.2 V, the Au surface is oxidized but no new diffraction spots or rings due to this oxide are observed in the images, indicating the formation of an amorphous oxide.

Grazing Transmission Small Angle X-ray Scattering (GTSAXS)

GTSAXS is a Small Angle X-ray Scattering (SAXS) technique that can probe the nanometre to micrometre size structures of a samples surface region [20], making it a good method for following the NP-AAO growth and deposition into the pores. Standard SAXS measures the transmitted signal of the sample, making the total signal a combination of the bulk and surface interactions, and is as such not very sensitive to the surface contribution. The surface sensitivity is increased by applying a grazing incidence angle geometry for the SAXS measurements, where two methods able to probe the surface and the in-plane structure is the GTSAXS and the Grazing Incidence Small Angle X-ray Scattering (GISAXS).

The GISAXS method lets the x-rays shine onto the sample at a grazing incidence angle which is chosen to be close to the materials critical angle of total external reflection. This makes the x-ray beam both become reflected and refracted at the sample's surface, leading to a signal that is a combination of a simple reflection and the refracted beam which has undergone multiple scatterings inside of the sample before escaping. In the scattering pattern, there is also going to be a horizontal streak, the Yoneda peak, which is due to dynamical scattering at these grazing incidence angles where the exit angle is close to the critical angle. The scattering pattern is measured as the reflection from the sample and the Distorted Wave Born Approximation (DWBA) can be used to analyse this pattern. However, the analysis of the GISAXS pattern is quite challenging due to it containing contributions of both reflection, refraction and the Yoneda peak [118], [128].

GTSAXS is the other mentioned SAXS method, this one has been developed to have an easier and more uncomplicated analysis than GISAXS. The GTSAXS method uses a small incidence angle, but substantially larger than the materials critical angle of total external reflection and detects the x-ray signal exiting from the samples side. This leads to an x-ray signal which only contains the refracted signal, where the multiple scattering of the refracted beam is reduced by letting the x-rays impinge on the sample near its edge. Due to these simplifications in the x-ray interaction with the sample, the GTSAXS signal can be analysed with the easier Born Approximation (BA) [120].

The scattering angle of the X-rays emitted from the side of the sample will be small and therefore the detector has to be placed several metres away from the sample to be able to resolve the scattering pattern. To reduce the scattering of the x-rays while they travel between the sample and the detector an evacuated flight tube can be

placed in between them [129]. An illustration of the GTSAXS measurements for the electrochemical experiments performed in paper II is shown in Figure 22.

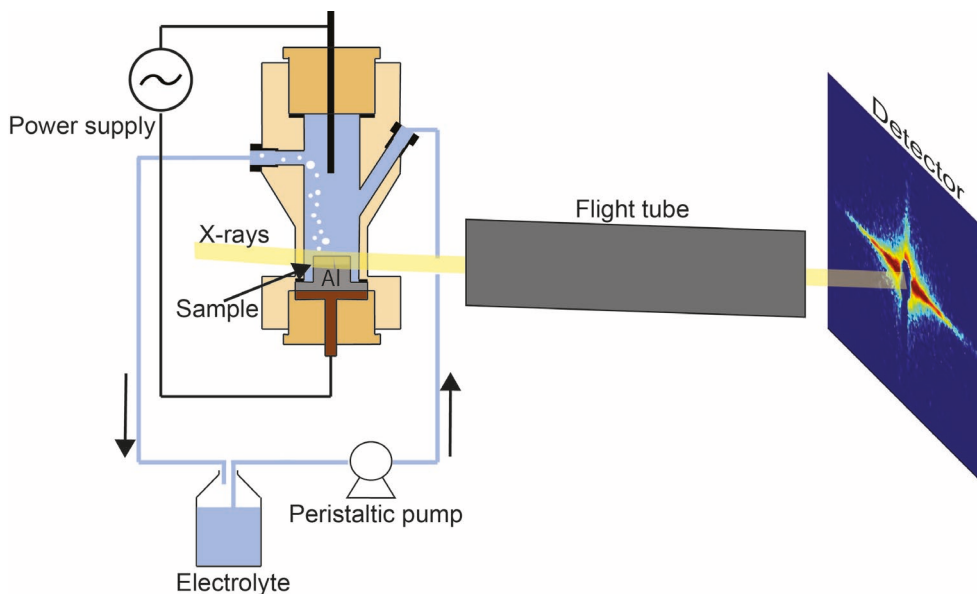


Figure 22. The experimental setup used for the GTSAXS measurement of the NP-AAO and the electrochemical metal deposition into them.

The GTSAXS scattering pattern is created through the electron density difference inside the sample, and better contrast between the elements in the sample can be achieved by for example varying the x-ray energy around the absorption edge of the material of interest. This method is called Anomalous GTSAXS and makes it possible to extract element-specific information [20], [118].

Information of the out of plane structures and the in-plane structures can be given through the scattering vectors q_z and q_r (the in-plane vector which combines q_x and q_y). From the scattering pattern, the structure factor can be used to extract information about the ordering and the structure in the sample, while the form factor can be used to get information about the shape of the structures in the sample. These structures in the sample can be determined by extracting and fitting line cuts along the q_z and q_r directions in the scattering pattern [119].

The growth of porous aluminium oxide during both the first and second anodization step has been followed with GTSAXS in two papers by the Lundgren group [56], [57]. It is shown that the GTSAXS can be used to determine the pore distance and domain size in the oxide by the extraction of line cuts along the scattering pattern. From the line cuts the position and the width of the Bragg peaks can be used to

determine the pore distance and domain size, respectively, an illustration of this is shown in Figure 23.

The pore distance can for a hexagonal lattice be calculated with equation 38. In the equation, Q_{hk} is the position of the indicated Bragg peak in Figure 23, which can also be expressed as q_z or q_r if the out-of-plane or in-plane scattering is to be analysed, h and k are the miller indices, while the pore distance is given by a .

$$Q_{hk} = \frac{4\pi\sqrt{h^2+hk+k^2}}{\sqrt{3}a} \quad (\text{Equation 38})$$

The domain size, the area over which the pores are ordered in relation to each other, is expressed with equation 39. In this equation, the domain size is given by D and the width of the first Bragg peak which is used for extracting the domain size is given by Δq_y [56], [57].

$$D = \frac{2\pi}{\Delta q_y} \quad (\text{Equation 39})$$

GTSAXS was in paper II, used to follow the porous aluminium oxide growth and deposition of Sn into the pores. The experiment had the x-rays impinge on the middle of the sample instead of the edge, making sure enough pores were investigated to get reliable data. It was possible to measure this large amount of data and still get a good intensity of the detected signal because of the low x-ray absorption of aluminium [130]. A grazing incidence angle of 0.3° , which is above the critical angle of external reflection for aluminium, and an x-ray energy of 29.35 keV was used. After the x-rays had interreacted with the sample, a 2D detector was used to detect the x-rays which have been emitted from the side of the sample. From these measurements, information about the oxide growth and electrochemical deposition into the pores could be extracted by taking line cuts of the GTSAXS pattern, shown in Figure 23. The line cuts were taken along $q_z=0$ and fitting of the curve were done approximating the pores as polydisperse cylinders in a hexagonal lattice. From this, information about how the deposition of Sn affected the relative domain size could be gained.

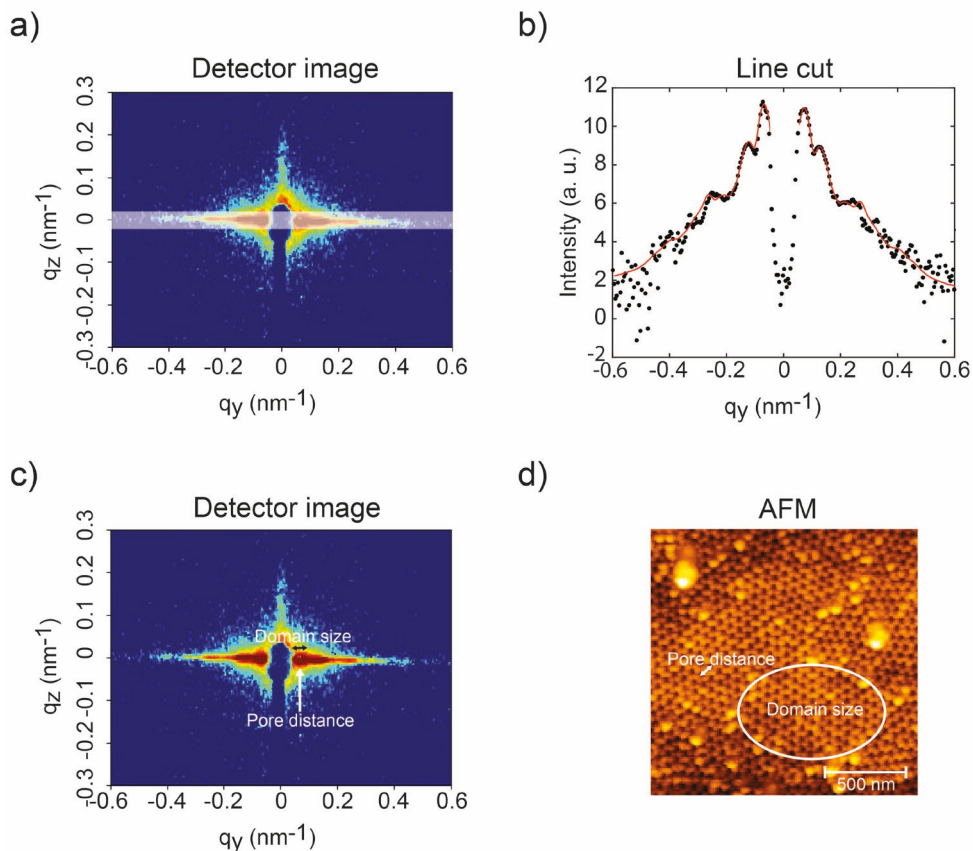


Figure 23. The GTSAXS pattern of NP-AAO with Sn deposited in the pores. The white box is where the linecut was taken. b) The plotted intensity of the line cut and a fitting of the data (red line). The peaks in this signal are the Bragg peaks in the GTSAXS pattern. c) By using the indicated Bragg peaks position and width the pore distance and domain size of the NP-AAO could be extracted. d) An AFM image of an NP-AAO indicating the domain size and pore distance.

X-ray spectroscopy methods

In this thesis, XRF and XANES have been used to follow the electrochemical deposition of Sn into NP-AAO. XPS has been used to investigate the changes in the chemical structure of an Au(111) surface during CV and LSV when the surface is oxidized. A schematic of these processes is shown in Figure 24, where the Auger process is also included due to the possibility to create and detect Auger electrons in both XANES and XPS measurements. The XRF, XAS/XANES and XPS

processes will be presented in further detail in the following sections, while the Auger process will be presented here below.

The Auger process, shown in Figure 24 d), has an x-ray impinging onto the sample, which will eject a core electron. This creates a core hole that will be filled by an electron from a higher electron shell, with higher energy. The energy difference between the two electron shells will be transferred to an electron in a higher electron shell. This electron will be ejected from the sample as a so-called Auger electron [29].

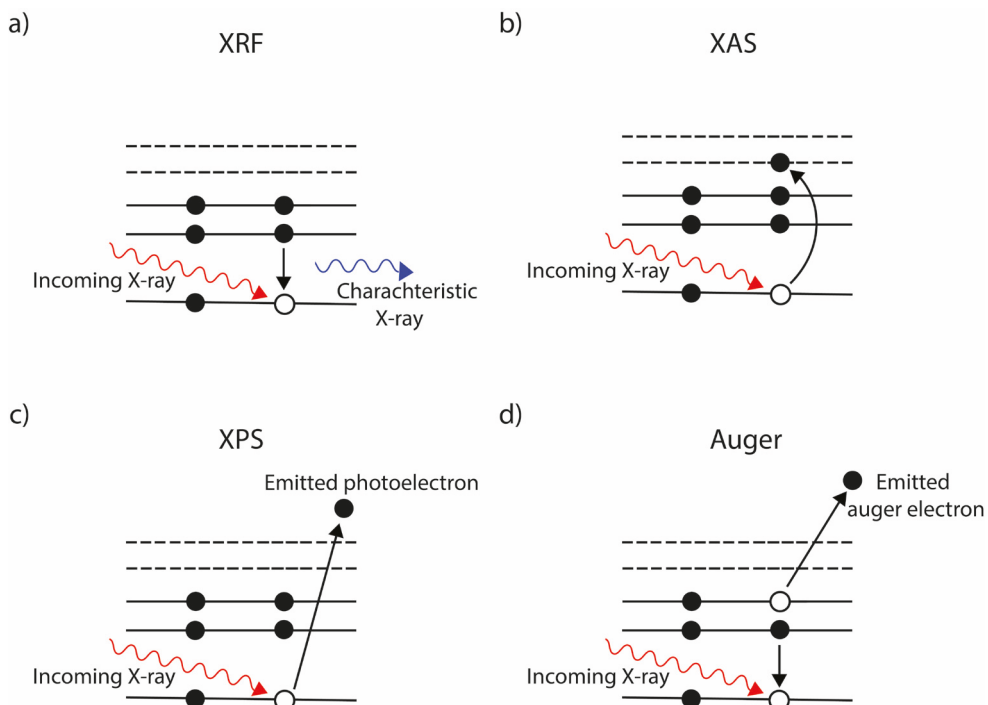


Figure 24. Illustration of the X-ray spectroscopy methods, XRF, XAS/XANES, XPS and the Auger process. a) In XRF, an incoming x-ray will eject a core electron, leaving a core hole (the white circle). This core hole will be filled by an electron from a higher energy shell falling down and the energy difference between the electron shells is emitted as a characteristic x-ray. b) The XAS or XANES method. An incoming x-ray will be absorbed by a core level electron, which will be excited to an unfilled valence shell or ejected depending on the energy of the incoming x-ray. c) In XPS the incoming x-ray will eject a core electron, which will be ejected as a so-called photoelectron. This electron will be used to create the XPS spectra. d) The Auger process starts with an incoming x-ray ejecting a core electron, the created core hole will be filled by a higher energy shell electron. The energy difference between the shells is transferred to a higher shell electron, which will be ejected as a so-called Auger electron.

X-ray Fluorescence (XRF)

XRF is an x-ray spectroscopy technique used to investigate the chemical composition of a sample. The technique is illustrated in Figure 24 and explained here as x-rays impinging onto the sample with an energy that is higher than the binding energy for the investigated materials core-shell electrons. This will lead to absorption of the x-rays by the core electrons, which will be ejected from the atom creating an electron-hole vacancy in the core shell and making the atom excited. An electron with higher binding energy, originating from a higher electron shell will fill the electron-hole and emit the energy difference between the electron-hole and the higher electron shell as a characteristic x-ray. This characteristic x-ray has a specific energy for the particular material investigated, due to the specific energy levels of each material. Another way for the atom to become deexcited is through Auger electron ejection. The cross-section of the process will determine if fluorescent x-rays or Auger electrons will be emitted, where fluorescent x-rays are the most probable for heavy elements, while Auger electrons are more likely for lighter elements [20], [29].

XRF was used in this thesis to follow the electrochemical deposition process of Sn into the NP-AAO. This was done in both papers I and II, where the deposition was followed during the whole deposition time and as a function of the height of the pores. The fluorescence signal could be detected to increase over time as the pores filled. It was also possible to see that the deposition started in the bottom of the pores and filled them as the deposition occurred, which was visible in the height scan of the XRF signal. The XRF signal as a function of height is shown in Figure 25 for two different x-ray beam sizes.

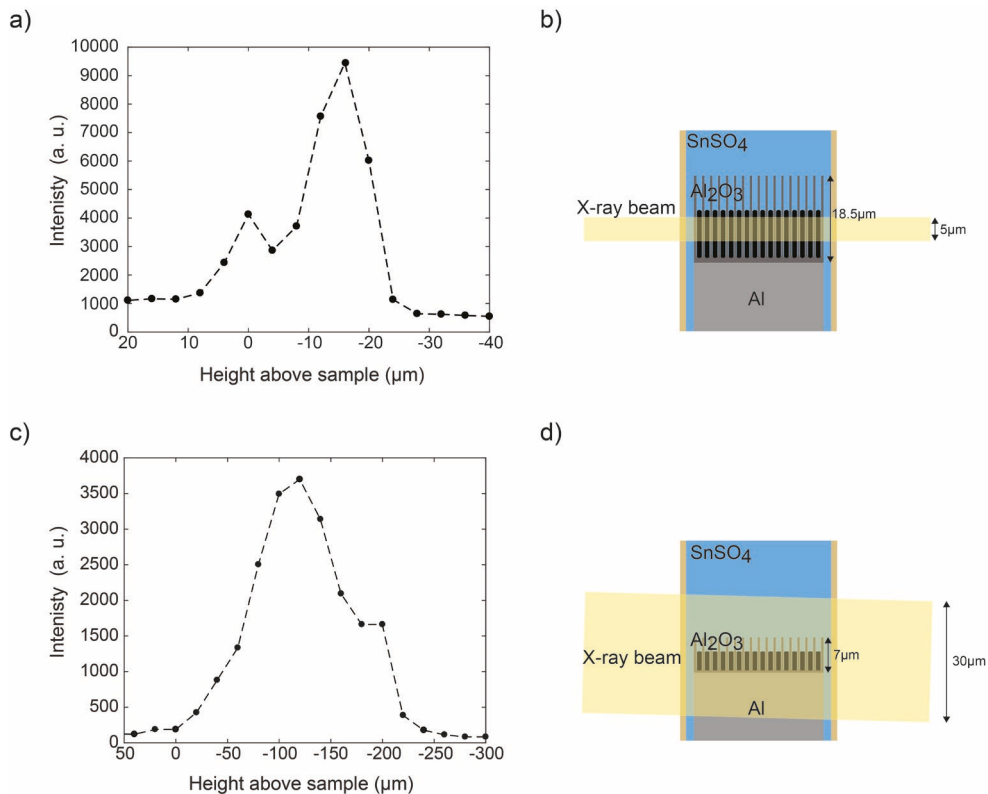


Figure 25. a) and b) are the data measured in paper I. a) The XRF signal of Sn in the NP-AAO measured as a function of sample height. The x-ray beam was 5 μm and the pores were 18,5 μm high. b) The pores illustrated in relation to the height of the x-ray beam. c) and d) are the data measured in paper II. c) The XRF signal of Sn in the NP-AAO measured as a function of sample height. The x-ray beam was 30 μm and the pores were 7 μm in height. d) The pores illustrated in relation to the height of the x-ray beam.

X-ray Absorption Spectroscopy (XAS)

XAS is a technique used to probe the electronic states and the structure of the sample. The technique scans the x-ray energy through the core-shell electrons binding energy of the element of interest in the sample. At the x-ray energy corresponding to the core electrons binding energy, there is an increase in absorption, which corresponds to the core-shell electrons absorption energy. This increase in absorption is called the absorption edge. The energy for this absorption edge is specific to the core-shell energy of the investigated element, making this an element-specific method. The scan goes between the x-ray energies below the absorption edge and the x-ray energies above the absorption edge, leading to a spectrum containing information both at the absorption edge and around it. The

absorption of the x-rays as the scan is conducted results in the core electrons becoming excited either to the continuum as photoelectrons or to the unfilled valence states of the material. These excited electrons and atoms will need to be deexcited which is achieved by the emission of either fluorescent x-rays or auger electrons. The XAS spectrum is then created either by measuring the transmitted signal, the photoelectrons, the fluorescent x-rays or the auger electrons as a function of the energy of the incident x-rays [20], [131].

X-ray Absorption Near Edge Structure (XANES)

XANES is a XAS technique that measures the signal at the absorption edge and close around it. The area of the XAS spectrum used for XANES is illustrated in Figure 26. From the measured XANES spectra, the chemical (oxidation) state can be determined for the investigated material.

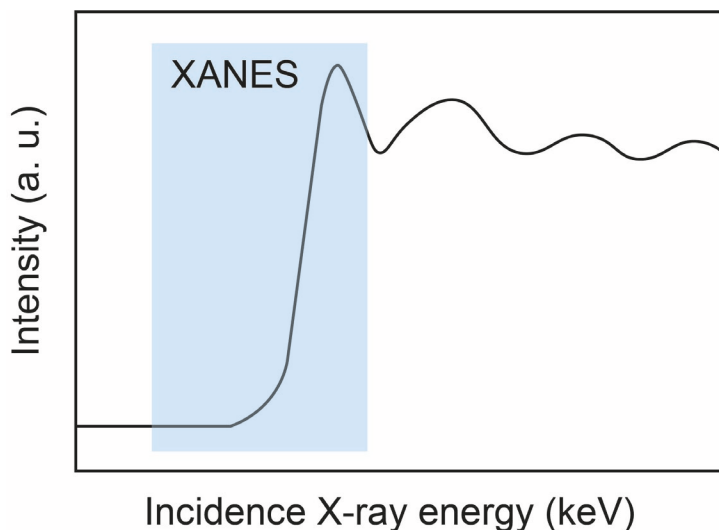


Figure 26. An illustration of a hypothetical XAS spectrum. The blue area shows the part of the XAS spectra used for XANES measurements.

The XANES signal is measured as a function of the energy of the x-ray impinging onto the sample, the same as for the standard XAS measurement. In this technique the x-ray energy is scanned from below, but close to, the absorption edge until just above it for the material of interest. A sharp edge is shown in the spectrum at the absorption edge where the electrons are excited into the lowest unoccupied state in the atom. In XANES we measure the spectrum using either the intensity of the transmitted beam, the photoelectrons, the fluorescent x-rays or the Auger electrons.

The measured signal is visualized as an intensity signal versus the incidence x-ray energy. The spectrum can give information about the geometry and electronic state of the material/atoms investigated. Usually, to determine the chemical state of the material in the sample, the spectrum is compared to measured curves of reference samples[20], [132], [133].

XANES was used in paper II to determine the chemical state of the deposited Sn in the NP-AAO. Measurements were conducted both before and after the deposition had occurred and the measured spectrums were compared with standard reference samples. It was shown that before any deposition occurred, the state of the Sn in the pores, which were the Sn dissolved in the electrolyte, were Sn^{2+} . After the electrochemical deposition had occurred the Sn inside of the pores were metallic, indicating the growth of metallic Sn nanorods. The spectrums used to gain this information are shown in Figure 27.

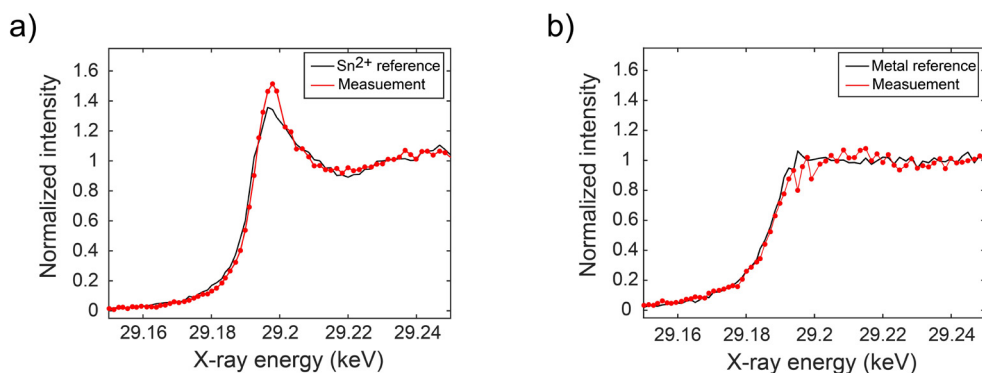


Figure 27. a) The XANES spectrum before deposition. The red measured XANES curve is shown to correlate quite well with the Sn^{2+} reference curve, indicating that the Sn in the pores and electrolyte is in that chemical state. b) The XANES spectrum after deposition. The red measured XANES curve is shown to correlate quite well with the metallic Sn reference curve, indicating that the Sn in the pores is metallic confirming the growth of Sn metal nanowires.

X-ray Photoelectron Spectroscopy (XPS)

XPS, or Electron Spectroscopy for Chemical Analysis (ESCA) as it is also called, is a surface-sensitive x-ray technique used for investigating the chemical state of a sample's surface. The technique is based on the photoelectric effect which was discovered in 1887 by Hertz and explained by Einstein in 1905, for which he received the Nobel prize in 1921 [134]. XPS relies on the knowledge that the chemical state of the elements can be determined from their core-level binding energy. The binding energy is dependent on the chemical surrounding of the atoms and will shift in energy due to this interaction, which was discovered by Siegbahn. He used this discovery to develop the modern-day XPS system during the 1960s,

for which he received the Nobel prize in 1981 [135], [136]. Most XPS systems utilise UHV conditions, however, systems for higher pressures (Ambient pressure – XPS) as well as systems for conducting electrochemical experiments inside the XPS system exists [137].

XPS use monochromatic x-rays between 10 to several 1000 eV to irradiate the sample [138], these will interact with the electrons within the sample through the photoemission process. This leads to the emission of core electrons. The x-rays will penetrate and interact with the sample up to several micrometres into it, however, only the electrons close to the surface will escape. This is due to the short mean free path of electrons inside of matter, only making it possible for electrons from around some tens of Å to escape the sample without scattering inelastically. The electrons which have no inelastic losses will create the peaks in the XPS spectra and electrons suffering from inelastic scattering losses will contribute to the background signal in the spectra. The detection of the emitted electrons determines the number of emitted electrons from the sample and their kinetic energy, which is often converted to the binding energy of the photoemitted electrons. Each element has specific binding energies of the core levels making it possible to determine the elements in the sample from these measured energies, as well as their chemical state.

The spectrometer used for the detection of the electrons is constructed by extraction lenses/optics, an analyser and a detector (electron multipliers), shown in Figure 28. The lenses and optics define the acceptance angle for the detected electrons emitted from the sample. The energy of the detected electrons determines the resolution of the system, where lower energies give better resolution. Because of this, the electrons travelling through the detector will get their energy reduced via the interaction with the lenses to a specific pass energy before they enter the analyser. The smaller pass energy will give a better resolution, but also less intensity. The most common analyser is the hemispherical analyser, constructed by an outer and inner sphere. These spheres have voltages applied to them, with the inner one being more negative than the outer one. This construction will only let electrons with a certain energy pass through the analyser and be detected, if the energy is not correct the electrons will instead collide with one of the spheres. Electrons with different energies can pass through the analyser by changing the voltages applied to the spheres. The achievable resolution of the detected signal will be determined by the radius of the spheres [134], [137].

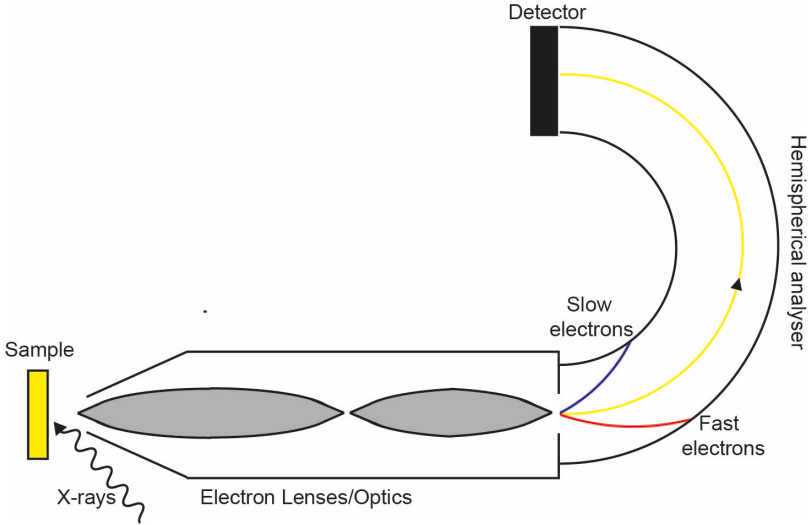


Figure 28. An illustration of an XPS setup, the whole setup will be in UHV. As the x-rays shine onto the sample photoelectrons will be created. These will then travel through the lenses, where they are focused and reduced in energy. These will then reach the analyser where only the electrons with specific energy will pass through and get detected.

To describe the emission process of the electrons from the sample, a three-step model developed by Berglund and Spicer can be used, this is an approximate description of the XPS process [139], [140]. In the first step, the system or sample is at an initial energy of E_i . An x-ray with energy $h\nu$ will impinge onto the sample and interact with an electron in the system leading to excitation of the electron. The next step results in the excited electron travelling to the surface of the sample. In the final step, the electron overcomes the vacuum barrier of the sample and becomes free, leaving the sample with a kinetic energy of E_{kin} (or KE). This leaves the sample with a final energy of E_f . Using the law of conservation of energy this process can be expressed by equation 40.

$$E_i + h\nu = E_f + E_{kin} \quad (\text{Equation 40})$$

Considering that the ionization potential of this sample is the energy difference between the initial (E_i) and final state (E_f), and that the ionization potential can also be expressed as the combination of the binding energy E_{bin} (or BE) and the work function of the sample ϕ , makes it possible to rewrite equation 40 to equation 41.

$$E_{kin} = h\nu - E_{bin} - \phi \quad (\text{Equation 41})$$

By keeping the Fermi level of the spectrometer equal to the Fermi level of the sample, the combination of the work function of the sample (ϕ_{Sample}) and the kinetic energy (KE_{Sample}) in regard to the sample, will be equal to the work function of the spectrometer ($\phi_{Spectrometer}$) and the kinetic energy, which will be the measured kinetic energy ($KE_{Spectrometer}$), in regard to the spectrometer, this is illustrated in Figure 29 and expressed as equation 42.

$$KE_{Sample} + \phi_{Sample} = KE_{Spectrometer} + \phi_{Spectrometer} \quad (\text{Equation 42})$$

Using this it's possible to rewrite equation 41 into equation 43 in which all parameters except the binding energy can be measured or are known.

$$KE_{Spectrometer} = h\nu - E_{bin} - \phi_{Spectrometer} \quad (\text{Equation 43})$$

In the equation above the photon energy, $h\nu$, will be known as long as a monochromatic x-ray source is used, $KE_{Spectrometer}$ is the measured kinetic energy and the work function $\phi_{Spectrometer}$ of the spectrometer is a known parameter for the specific spectrometer used. Since all these parameters are known equation 43 can be used for determining the binding energy of the emitted electron.

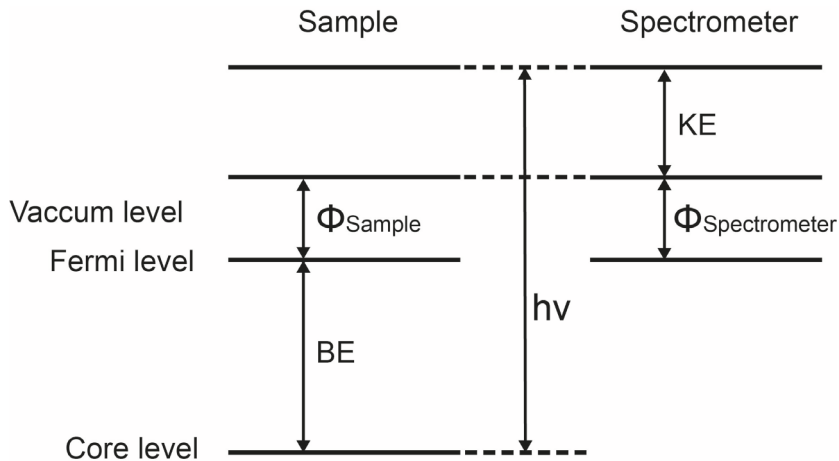


Figure 29. An illustration of the sample and spectrometers energy levels and binding energy in regard to the energy of the impinging x-ray.

The emission of the photoelectrons will lead to the creation of a core electron-hole, this core hole will be filled by an electron from an outer shell falling down. The electron will emit the energy difference between its originating shell and the core shell as either fluorescent x-rays or auger electrons. The auger electrons will be able to be detected and shown as peaks in the XPS spectra and can sometimes be useful in the determination of the elements in the sample. Their energy will be determined by the energies of the shells of the electrons taking part in the process and will be independent of the incidence x-ray. This means that a change in x-ray energy will shift the measured energy of the Auger lines. The energy of the Auger electrons is also affected by the chemical environment of the atom [134].

The XPS spectrum is created by measuring the number of emitted electrons as a function of the binding energy. The measurement usually starts by measuring a survey spectra, usually between 0-1100 eV [138], to determine the elements in the sample, after which narrower high-resolution scans are measured to determine the exact positions and binding energies of the peaks of interest. In a lot of cases, the peaks for the detected photoelectrons are split into two peaks due to the core level having spin-orbit coupling. The binding energy of the peaks gives information about the chemical state of the material and can give information about for example the oxidation state of the material. When a material is oxidized the binding energy will be shifted to higher energies, where the shift will be larger with higher oxidation numbers [137]. The determination of the chemical state and oxidation state is achieved by comparing the shift in the binding energy with experimental standards of the materials. To determine the elements or elements creating overlapping peaks, fitting of the spectra can be used.

XPS was used to measure the chemical state of an Au(111) crystal as it was electrochemically oxidized using an 0.05 M H₂SO₄ electrolyte in paper VIII. The measured spectrums for specific applied potentials are shown in Figure 30. To follow the electrooxidation, the O 1s, the S 2p and the Au 4f spectra were measured. The measurements started with potentials of 1.5 V and continued to higher potentials up until the potential for OER was reached. The first indication of a change of the surface comes at a potential of 1.6 V where peaks appear in the S 2p and O 1s regions indicating absorption of sulphate or bi-sulphate on the Au surface. The sulphur peak disappears at 1.8 V, while a new peak appears in the O 1s spectra together with an oxide peak in the Au 4f spectra, suggesting the start of gold oxide or gold hydroxide formation on the Au surface.

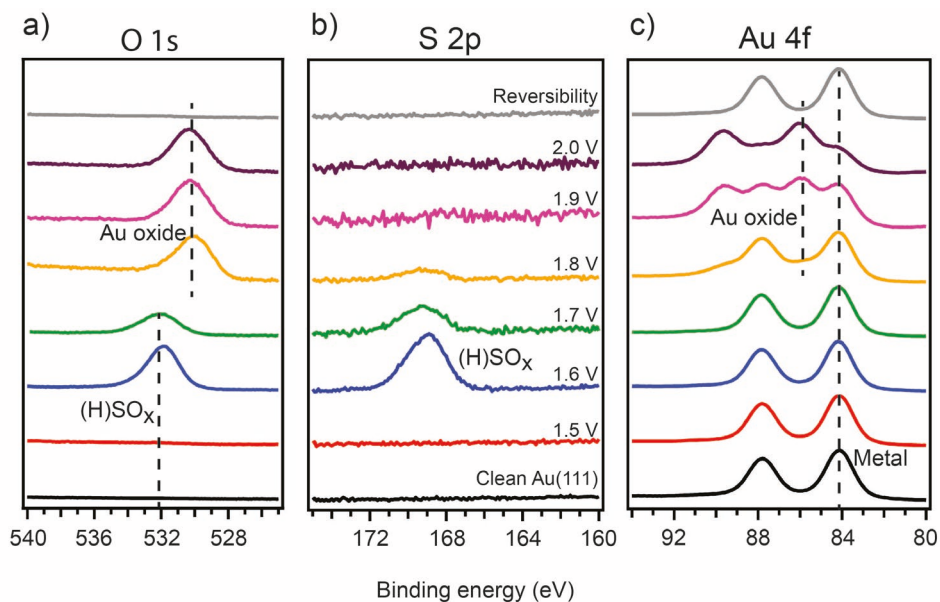


Figure 30. The O1s, S2p and Au4f spectra measured for Au(111) during electrooxidation using a 0.05 M H₂SO₄ electrolyte. It is shown that as the potential is increased a component appears in the S 2p in conjunction with the appearance of a component in the O 1s region indicating the absorption of sulphate or bi-sulphate. As the potential increases, these components disappear and a new peak in the O 1s spectra is observed with the appearance of an oxide peak in the Au 4f spectra indicating the formation of an oxide or hydroxide on the Au(111) surface.

Non-X-ray based techniques

2D-Surface Optical Reflectance (2D-SOR)

2D-SOR is an optical technique used for investigating the samples surface and its surface changes on a macroscopic/microscopic scale. The technique measures the changes (decrease or increase) of the reflected light from the sample surface during a reaction, and as such can follow how the sample is changing due to the reaction occurring. This method was first applied to gaseous reactions to follow the surface changes of the sample during catalytic activities [15]–[18], [81]. However, in this thesis, the possibility to apply it to electrochemical systems have been shown.

This technique uses incoherent, collimated light from an LED with a 650 nm wavelength, which is focused onto the sample. The collimation and filtering of the light are achieved through lenses and aperture. The light is then reflected onto the sample with a beam splitter. The reflected light from the sample is then registered with a CMOS camera after passing through the beam splitter and additional lenses [81]. To extract the reflectance changes of the measured image, the image will be subtracted by the image measured from the sample before any reaction has occurred.

To combine this technique with the electrochemical PEEK cell a modification of the top part of the cell was made to include a glass window, through which the light could be reflected from the sample. A schematic of the 2D-SOR setup with the electrochemical cell is shown in Figure 31. The setup with exact specifications of the 2D-SOR components and the modified PEEK cell are given in paper V.

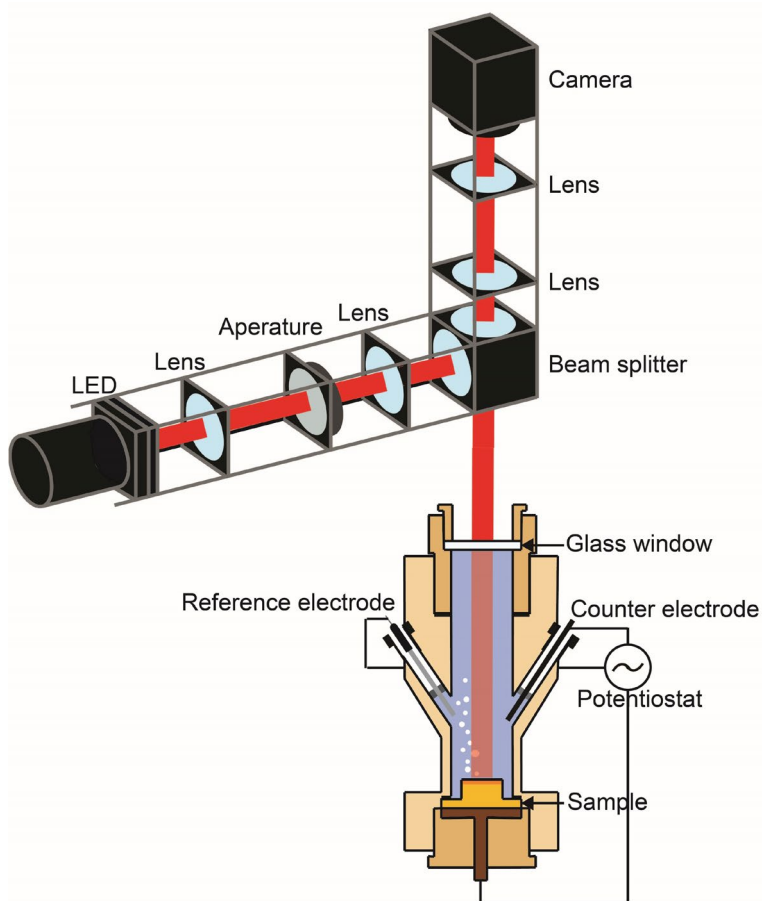


Figure 31. The experimental setup for applying 2D-SOR to electrochemistry. The light will shine onto the sample through the electrolyte.

2D-SOR has been used to follow both anodization of aluminium samples as well as the surface changes during CV of Au(111) and Pt(100) single crystals and polycrystalline Au and SDSS samples. It was possible to correlate well-known reactions and surface changes indicated by the change in CV current with the measured intensity of the 2D-SOR. This showed that the technique is useful for following electrochemical processes *in situ*. The 2D-SOR at four different potentials, where characteristic features in the CV of Au(111) are found, is shown in Figure 32. It was shown that the intensity of the reflectance decreased as the surface oxidized and the potential went into the oxygen evolution region, which is likely due to the formation of oxide and a roughening of the surface. It is also possible to see that the most reflective surface is the one at the negative potential limit. A similar trend could be detected for the Pt(100) single crystal, shown in paper

V. In paper VI the possibility of the 2D-SOR to follow surface changes of polycrystalline samples was shown, showing how different grains behaved differently during electrochemical conditions. The 2D-SOR has also been correlated with HESXRD measurements of Au(111) in paper VII, which demonstrated that the highest measured reflectance of the 2D-SOR was correlated with the appearance of the reconstructed HB surface.

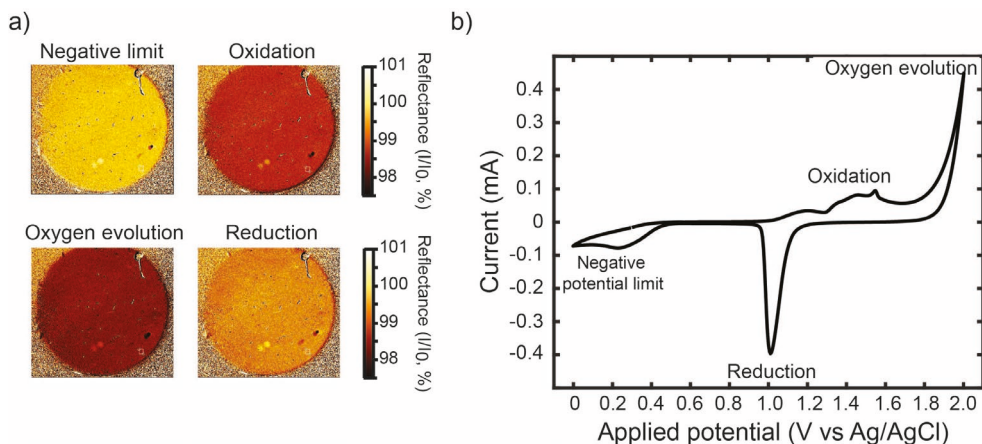


Figure 32. a) The 2D-SOR signal measured at four distinct reactions occurring on the Au(111) sample surface. The circle is the sample surface and the reflectance of this surface is indicated as a percentage, which is extracted by dividing each image with an image of the sample before any reaction has occurred. b) The measured CV of the Au(111) taken together with the 2D-SOR measurement.

Atomic Force Microscopy (AFM)

AFM is a microscopy method used either in vacuum or ambient pressures to record a real space image of a sample's surface. Both conducting and non-conducting samples can be imaged with this technique. The imaging of the sample is achieved by raster scanning an atomically sharp tip (attached to a cantilever) over the sample's surface while registering the atomic forces between the surface and the tip. The atomic forces are for example van der Waals, magnetic, electrostatic and chemical forces. These long- and short-range atomic forces will create an attraction or repulsion between the sample and the tip, which are measured as a deflection of the cantilever (in contact mode measurements) or a change in the oscillatory frequency of the cantilever (in a non-contact mode measurement). Different cantilevers with different properties exist for the AFM, where two examples are the silicon cantilever and the qPlus sensor. The silicon cantilever reflects a laser onto the cantilever to detect the change in position or frequency. The qPlus sensor is a quartz tuning fork, where the change in frequency is used for creating the AFM image [141], [142].

AFM in the non-contact mode was used to image the NP-AAO, shown in Figure 33. These pores were grown using an oxalic acid electrolyte to anodize the aluminium sample. From this image, it is possible to see the pores and their hexagonal arrangement.

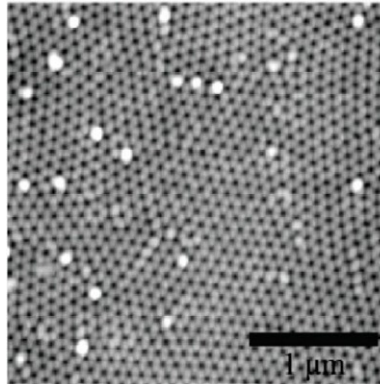


Figure 33. AFM image of the NP-AAO. Courtesy to Jonas Evertsson for the image [143].

Focused Ion Beam-Scanning Electron Microscope (FIB-SEM)

This thesis used a FIB-SEM, an instrument that incorporates both a SEM and a FIB to image and cut into the samples. FIB-SEM was used to cut into the NP-AAO and image the pores and the deposited metals within the pores.

Scanning Electron Microscope (SEM)

SEM is an imaging technique that scans a beam of electrons over a sample to image the sample surface of mainly conducting materials, non-conducting materials are possible to image however they are more challenging. This technique investigates the area close to the samples surface, to reveal information about both the structure and the chemical composition. The surface sensitivity depends on the penetration depth of the electrons into the sample, which depends on the energy of the electrons, the density of the investigated material and the atomic number, where a higher surface sensitivity is achieved with low electron energy and materials with a high atomic number. SEM use vacuum conditions for the whole microscope setup to minimise unwanted scattering. The use of vacuum conditions means that any sample which should be investigated with SEM needs to be compatible with this environment.

In the SEM, the generation of the electrons is achieved using an electron gun. In the electron gun a current will be supplied to a tungsten filament which will heat and emit electrons, the higher current the more electrons will be emitted. Between this electron gun and an anode, there will be applied a potential, usually between 1-30 kV, which accelerate the electrons to a desired energy of 1-30 keV. After the acceleration, the electrons will be focused and bundled together using (electromagnetic) condenser lenses and apertures. An objective lens will be used for controlling the beam position onto the sample, and as such the scanning of the beam over the sample to create the image. The size of the area over which the beam is scanned will determine the magnification in the image and the resolution will be determined by the size of the beam hitting the sample and is controlled by the current. The SEM image is then constructed by detecting the emitted electrons and x-rays from the sample at each position of the beam, where different detectors are used for registering the backscattered electrons, secondary electrons, and x-rays. The detection of the electrons is accomplished using a bias between the sample and the detector to accelerate the electrons towards the detector. In the detector the electrons will interact with a scintillator, to convert the electron signal into light. This signal is then amplified with a photomultiplier tube and thereafter converted to a voltage to create the SEM image.

The interaction between the sample and the electron beam will be through scattering of the electrons in the sample creating, secondary, backscattered and auger electrons as well as x-rays. These different species will be emitted from different depths of the sample, which is shown as the interaction volume of the electrons with the sample, see Figure 34. The size of the interaction volume, and as such the depth the electrons can reach into the sample and still emit the different species, is determined by the acceleration voltage, where a higher voltage will result in a larger interaction volume. The created auger electrons will escape the sample from just a short distance into the sample. In the case of the secondary electrons, which are created by inelastic scattering between the incidence electrons and the atoms in the sample, only the ones created close to the surface (5-10 nm into the sample) will be able to escape and be detected. This is due to the low energy of these electrons, which will be around 50 eV or lower. The backscattered electrons, which are electrons that have scattered elastically one or multiple times in the sample, will be able to escape from deeper within the sample. This is due to them having higher energy, usually above 50 eV. Characteristic x-rays, which are created by the core hole (created due to the incidence electron ejecting a core electron) being filled by a higher energy shell electron and the energy difference being emitted as an x-ray, will be able to escape the sample from even further within. There is also the possibility to emit bremsstrahlung x-rays, due to the deceleration of the electrons within the sample [144].

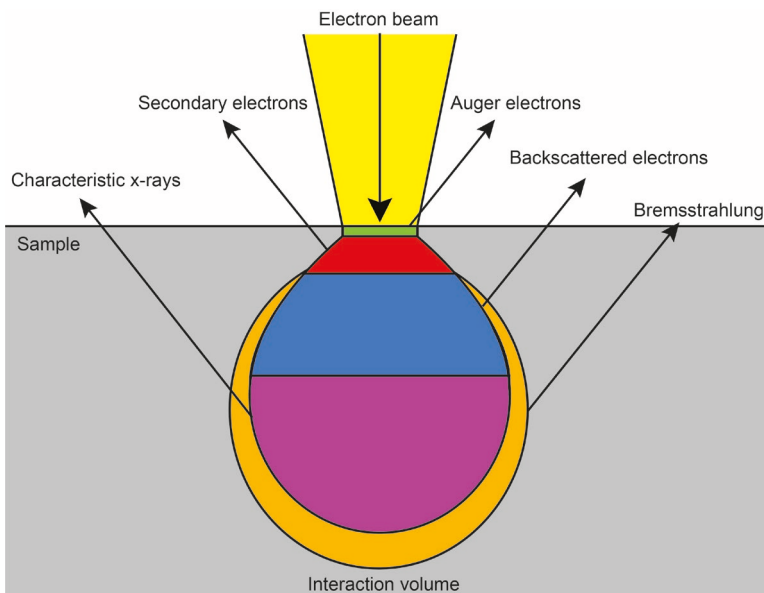


Figure 34. The interaction volume of the incident electron beam with the sample. The image shows from where in the sample the auger electrons, the secondary electrons, the backscattered electrons, the characteristic x-rays and the bremsstrahlung originates.

The detection of the backscattered and secondary electrons represents two different modes to create SEM images. The backscattering imaging mode creates its image from the backscattered electrons that leave the sample at an angle of 90° or above. This imaging method will be able to differentiate between the different material in the sample which is due to the scattering intensity varying between different materials. A material with a higher atomic number will result in more scattering and a more intense signal, this is shown brighter in the image. The secondary electron mode is a surface-sensitive imaging mode due to the emitted secondary electrons originating close to the samples surface, creating images of high topographical resolution. The Auger electrons and the characteristic X-rays will be able to give information about the chemical composition of the sample, due to their characteristic energy for each specific element. This makes it possible to create elemental maps of the sample [145], [146].

SEM could be used to image the NP-AAO as well as the deposited metals inside the NP-AAO. It was possible to see metal rods for all three metals (Sn, Pd and Au) deposited into the pores in paper I-IV. The clear visualisation of metal rods inside of the NP-AAO showed that electrochemical metal deposition is a good method to grow well-ordered nanowires. The deposited Sn in the NP-AAO has been imaged in Figure 35 by SEM, SEM images of the Pd and Au rods can be seen in paper III and IV.

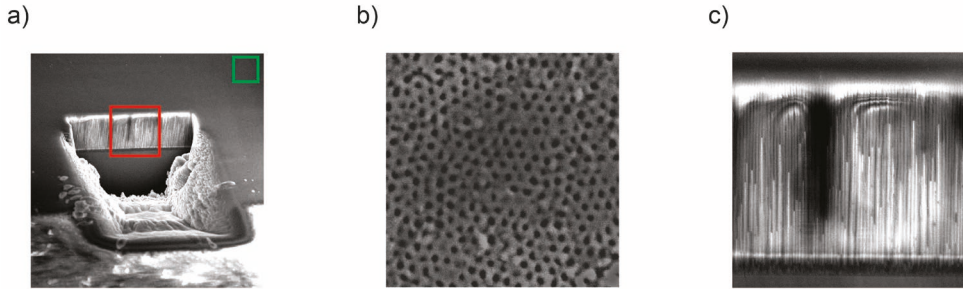


Figure 35. a) A SEM image of the NP-AAO with Sn deposited inside of the pores showing a trench cut into the sample to expose the pores. The green and red box indicate at which location image b) and c) are recorded, respectively. b) The NP-AAO imaged from the top, here the pores are clearly visible. c) The pores with deposited Sn inside. The brighter rods are the Sn nanorods in the sample.

Focused Ion Beam (FIB)

The FIB is a scanning microscope that uses an ion beam to irradiate the sample. This technique can be used both for imaging and to cut into the sample to reveal the structure inside of the sample.

In the FIB the ions, usually gallium ions, are created using an ion beam needle or tip which is connected to a Ga metal piece. As the ion gun is heated the ions will flow from the metal piece to the tip, where extraction of the ions is achieved by applying a strong electric field on the tip using an extractor electrode and suppressor to achieve the right amount of emission. The ion beam is then accelerated through the column (containing the focusing optics) and focused with electrostatic lenses and apertures. An objective lens is used for scanning the beam across the sample [147]. The accelerating voltage used for the Ga beam will control the energy of the ions and as such the penetration depth (interaction volume/damage zone) into the sample, it will also affect the resolution where a higher voltage will give better resolution but penetrate further into the sample, resulting in a larger damage zone. The current controls the intensity of the beam where a smaller current will result in greater resolution and less material removal [148].

The interaction between the ion beam and the sample will lead to material being sputtered away, the creation of secondary electrons and implantation of ions into the sample, which will lead to some damage of the sample. The ions will only penetrate a small distance into the sample; however, the sputtering radius of the beam is quite large, in the range of tens of nanometres. Imaging of the sample can be achieved by detecting the secondary electrons. The sputtering of the atoms with the ion beam will be used for cutting into the sample, by milling away some material. This makes it possible to image the structures inside the sample. The ejection of the material while milling occurs because of the atoms getting a high enough translational energy

in the interaction with the ions to be released from the material. To protect the sample while cutting into it with the ion beam, as well as creating a smooth cutting cross-section, a metal, such as Pt, can be deposited onto the surface before the milling begins. The sputtering/milling makes it possible to also cut out lamellas from the sample, by milling away the material around the lamella. This lamella can be moved to for example a TEM grid for further analysis with TEM imaging. The mentioned deposition of for example metals onto the sample in a FIB can be achieved with ion-beam activated deposition of a gas that is injected into the chamber [148], [149].

FIB was used in paper I-IV to cut into the NP-AAO samples to expose the pores, making it possible to image them with SEM. In papers I and IV FIB were also applied to cut out lamellas for further TEM investigation of the deposited nanorods.

Transmission Electron Microscope (TEM)

TEM is an electron microscope that images a sample by the detection of the electrons which have passed through the sample. Because this technique detects the transmitted electrons, the samples need to be thin, usually in the range of 100 nm or smaller, so as not to absorb too much of the electron beam. The need for thin samples might therefore require a lot of sample preparation before imaging with a TEM.

The TEM setup uses an electron gun to generate the electrons, where a current is passed over a tungsten filament to heat it and release electrons. These electrons will thereafter be accelerated by an applied potential to energies ranging between 100-300 keV, these high energies are needed for the electrons to pass through the sample. After the acceleration of the electrons, there is lenses and apertures to focus the electron beam onto the sample. The interaction between the beam and the sample will lead to electrons that are transmitted, scattered, and reflected through and from the sample. The electrons which pass through the sample are selected and focused by apertures and lenses onto the detector, to create the image of the sample. The magnification of the sample in the image will depend on how large/small the area irradiated with the electron beam is. The resolution of the TEM is determined by the wavelength of the electrons and the numerical aperture (the range of angles of the electrons that are transmitted through the microscope), where the typical resolution can be down to around 0.2 nm. It is possible to achieve atomic resolution with the TEM under the right conditions, high vacuum and specific wavelength of the electrons [150].

The TEM has two imaging modes, the bright field and the dark field mode. Whichever is chosen for the imaging is determined by the placement of the aperture after the sample, which determines which electrons are let through to the detector. In the bright field mode, the transmitted beam and the forward scattered electrons

are chosen to be let through to the detector, while the dark field mode blocks the direct beam and lets through the electrons which have diffracted within the sample. The bright-field mode is the most common mode used for imaging the sample. In this mode, the signal will be a 2D projection of the sample where the detected intensity at each position in the image will be determined by how much the electron has been absorbed in each position in the sample. The areas with high absorption of the electron beam, such as where the sample is thicker, the atomic number is higher and the material is denser, the detected intensity will be low and the image will be dark, while at the areas where most of the beam have been transmitted the image the intensity will be high, and the image will be bright. The dark field mode uses as mentioned the diffracted beam to create its image. Here the areas of the sample which have more material (the dark areas in the bright field mode) will lead to more diffracted electrons, which gives a high intensity of the signal and will be shown as bright structures in the image. The areas in the sample where there is less material to diffract the electrons lead to a less intense signal and this will be shown as dark areas in the image. The dark field imaging mode has the possibility to for example give information about the crystalline structure of the sample [151]. The diffracted electrons can also be used to detect a diffraction pattern, by changing the focusing, this technique is called Selected Area Electron Diffraction (SAED) and is presented in a separate section.

TEM has been used to image the Sn, Pd and Au nanostructures in papers I, III and IV. With this technique, it was possible to gain atomic-scale information about the nanostructures.

Energy Dispersive X-ray Spectroscopy (EDS)

EDS is used to determine the chemical composition of a sample. The technique uses fluorescent x-rays to determine the chemical composition, which is possible due to their characteristic energy for each specific element. The process for the creation of the fluorescent x-rays is the same as explained in the XRF section, with the only difference being that the core hole is here created by irradiating the sample with an electron beam.

The investigated area can be controlled by the energy of the electron beam, lower beam energy will give better spatial resolution due to less spread of the beam inside of the sample, but the intensity of the detected x-ray signal will decrease. An elemental map of the sample can be achieved by raster scanning the beam over the sample and measuring the fluorescence spectra at each position. The detected x-rays create a spectrum with intensity peaks corresponding to the different materials in the sample. By identifying these peaks, the elemental composition of the sample at the position of irradiation can be determined. There will, however, be detected a

background signal in the fluorescence spectra due to the interaction between the electrons and the sample also creating x-rays with continuous energy, this will limit the detection of very small elemental concentrations. The intensity of the detected fluorescence peaks will be used to determine the amount of the detected elements within the sample by comparing them to measurements of calibration standards of the elements [145], [152].

This technique was used to determine the elemental composition of the Pd and the Au nanostructures in paper III and IV.

Selected Area Electron Diffraction (SAED)

This is an electron diffraction technique implemented inside of a TEM, used to determine the crystal structure of a sample. The method utilises thin samples. A part of the electron beam shining onto the sample will diffract as it travels through the sample, resulting in constructive interference in specific directions determined by the crystal structure, similar to XRD. These diffracted electrons will create a diffraction pattern from which the structure and phase of the sample can be determined. The advantage of this technique is its ability to choose the area, which can be as small as a few hundred nanometres, that should be analysed by inserting an aperture that only allows electrons from a specific area of the sample to be detected. This makes it possible to image single grains in for example a polycrystalline sample [150].

This technique has been used in paper IV to study the grown Au nanostructures.

Electron Backscattering Diffraction (EBSD)

EBSD is a surface-sensitive electron diffraction technique used to obtain crystallographic information about the investigated sample. The technique can be used to extract information about the size, phase, and orientation of the grains in the sample's surface.

The measurement is conducted by shining an electron beam onto a polished flat crystalline sample. A shallow angle between the sample and the electron beam is used. The electrons which interact with the sample will be diffracted in a certain direction depending on the crystal structure of the sample, leading to interference between the diffracted electrons. The diffraction pattern will spread spherically in space from the interaction point between the sample and the electron beam. A fluorescent screen connected to a CCD chip is used to detect the diffracted electrons,

which creates a diffraction pattern (a so-called EBSD pattern). This whole measurement is conducted in UHV conditions.

The detected EBSD pattern will show bright bands, Kikuchi bands/(diffraction lines), which creates a unique pattern for each specific crystal structure. From this EBSD pattern information about the crystallographic phase and surface orientation of the sample can be extracted using dedicated software. The method can be used for analysing individual grains of the surface as well as large areas of the sample containing many different grains, through scanning of the beam over the sample [145].

This technique was used to determine the crystallographic orientations of the gains in the polycrystalline Pd and Au samples in paper VI.

Low Energy Electron Diffraction (LEED)

LEED is a surface-sensitive method used for determining the ordered crystallographic structure of a sample's surface. It is based on diffraction of the incoming electrons, in the same way, as XRD is based on diffraction of x-rays. The main difference between them is that LEED will only investigate the top atomic layers of the sample, due to the small mean free path of electrons within a material. LEED will give information about the in-plane structure, resulting in continuous lattice rods in the direction perpendicular to the sample and detector. The diffracted signals which will be detected are the ones intersecting the Ewald sphere. The spacing of the rods and the magnification of the LEED pattern will be determined from the incidence energy of the electron beam since it determines the radius of the Ewald sphere.

The electrons used for irradiating the sample will be created in an electron gun, which will also focus the beam onto the sample. The energy of the electrons will be between 30-300 eV making it a very surface-sensitive technique [153]. Scattering of the electrons will occur in the first few atomic layers, resulting in both elastically scattered electrons, inelastically scattered electrons and secondary electrons. The back-scattered electrons will be the ones travelling to the detector. The detector is constructed by a fluorescent screen to detect the electrons and grids used to filter out the unwanted electrons. The first grid, and the closest to the sample, will be grounded in the same way as the sample making the emitted electrons travel in a field-free space between the sample and the first grid of the detector. The second grid in the detector is used to filter out the unwanted electrons, the inelastically scattered and secondary ones. This is achieved by applying a retarding/negative potential to the grid, only making it possible for the elastically scattered electrons to

pass through the grid. The third grid is used to separate the fluorescent screen from the second grid. The fluorescent screen has a positive charge, leading to acceleration of the electrons onto the screen. As the electrons hit the screen fluorescent light will be produced, where the intensity is dependent on the intensity of the incoming electrons. The whole experiment is performed in UHV to limit the scattering of the electrons and any surface contamination. A schematic of the LEED is shown in Figure 36 a).

The detected elastically scattered electrons create a 2D reciprocal diffraction pattern, which can be used to determine the in-plane surface structure of the sample and its unit cell. A typical LEED pattern of a clean Au(111) surface is shown in Figure 36 b). By varying the incidence electron beam energy, it is possible to measure so-called intensity energy/voltage (I-V or I-E) curves, which can with modelling give information about the atomic positions at the surface and a few layers below [154].

LEED has in this thesis been used to investigate the Au(111) surface during electrooxidation in paper VIII.

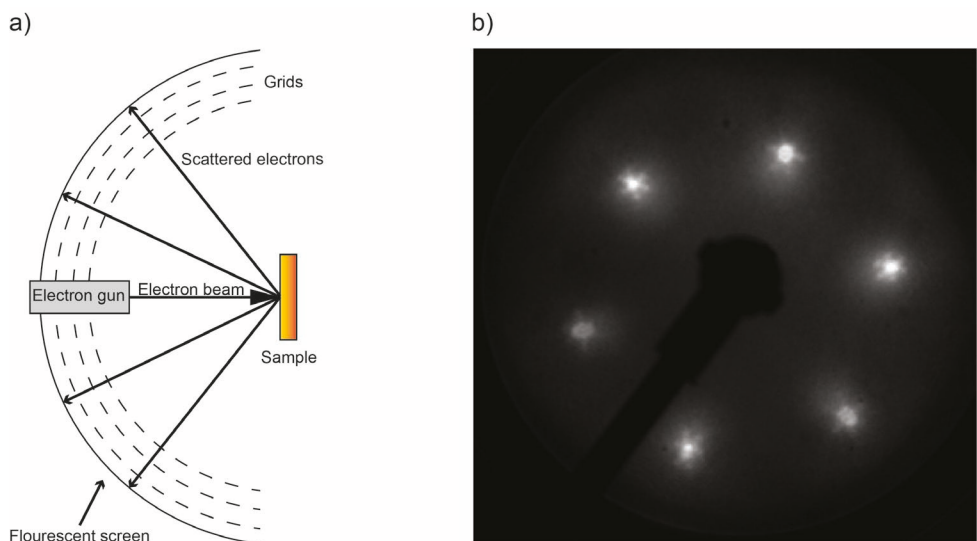


Figure 36. a) The schematics of the LEED setup. Where the electrons will shine onto the sample at a vertical angle and a hemispherical screen/detector is used so that all the back-scattered electrons from the sample can be detected. b) A LEED pattern of the clean Au(111) surface with the HB reconstruction on the surface, detected as weaker peaks around the main diffraction peaks.

Summary of papers

The papers in this thesis can be divided into two main projects. The first one is the study of electrochemical deposition into NP-AAO of different materials to gain a better understanding of the controlled nanowire growth inside of the pores. Paper I and II follow the growth of Sn nanostructures within the pores with a single NP-AAO template design to get a better understanding of the growth process. Paper III followed the deposition of Pd into two different templates to determine their effect on the nanowire growth. Paper IV followed the deposition of Au into two different templates, one of these templates was the same as for Paper III. The effect of the templates on the nanostructures was studied as well as the effect of using different deposition times.

The second project started with the demonstration in paper V of how a modification to our electrochemical cell could be combined with 2D-SOR to gain optical reflectance images of the sample's surface during electrochemical reactions. This showed the potential of using 2D-SOR to study surfaces inside a liquid. The potential of this technique to be used on polycrystalline materials was demonstrated in paper VI together with some further modification of our electrochemical cell to improve the measurement quality. In paper VII 2D-SOR was combined with HESXRD to study the Au(111) single crystal during CV measurements. The paper showed the possibility to correlate atomic changes to the measured reflectance and how 2D-SOR could detect monolayer changes of the surface. It also showed the potential of using HESXRD to follow the atomic surface changes during CV of the Au(111) single crystal, where an interest in the measured surface changes during the oxidation led to the study of this process in more detail using XPS and LEED in paper VIII. The well-known HB reconstruction on Au(111) was easily detected in the HESXRD pattern and an interest to show how HESXRD could follow the dynamics of this reconstruction lead to the investigation in paper IX. A software program was developed to analyse these measurements, following the lifting and formation of the HB reconstruction on the Au(111) single crystal during CV measurements.

Paper I: *Observing Growth under Confinement: Sn Nanopillars in Porous Alumina Templates*

Paper I focus on gaining a deeper knowledge of confined nanostructure growth in NP-AAO, in this case, to understand how the Sn structures grow and their crystalline state within the pores.

The electrochemical deposition of Sn into NP-AAO was followed *in situ* using XRD and XRF. The deposition process was investigated as a function of the pore depths and the deposition time. The NP-AAO templates used for deposition was created through the two-step anodization process, applying barrier layer thinning as the finishing step of the oxide growth. Branching of the pore bottoms was shown to occur due to this barrier layer thinning. The deposition into the pores used an electrolyte containing SnSO₄ and H₂SO₄ and an alternating voltage of 15 V_{rms} with a frequency of 400 Hz. By moving the sample up and down in the x-ray beam during the deposition process, information about the deposition process within the sample at different pore heights could be gained as a function of the deposition time. It was shown that the Sn deposited from the bottom up and grew β-Sn nanorods. The nanorods were constructed from crystalline grains which had a (100) crystal orientation. The grain size was shown to be around 7.5 nm in-plane, while the out of plane grain size was around 12 nm inside of the branched pore bottoms and increased continuously to 13.5 nm as the pores filled beyond the pore bottoms. A compressive strain was measured for both the in-plane and out of plane directions of the nanorods, the strain was also measured to be larger closer to the bottom of the pores. The part of the nanorods grown in the branched pore bottoms showed higher in-plane rotational disorders than the parts grown in the main pores. FIB-SEM/TEM was used *ex situ* to image the Sn rods within the sample, where Sn was visible within the main pores as well as in the branches in the bottom of the pores.

Paper II: *The State of Electrodeposited Sn Nanopillars within Porous Anodic Alumina from in Situ X-ray Observations*

Paper II focus on understanding how Sn nanostructures grow and fill the pores in the NP-AAO as well as determining the chemical state of the grown Sn nanostructures.

The electrochemical deposition of Sn into NP-AAO was studied with GTSAXS, XRF and XANES *in situ*. The NP-AAO templates were created through the two-step anodization and barrier layer thing process. The deposition was achieved using a SnSO₄ and H₂SO₄ electrolyte and an alternating sin wave voltage of V_{limit} = ± 21.22 V with a frequency of 400 Hz. The XRF measurements showed a continuous increase in the amount of Sn within the pores during the entire deposition process, indicating the growth of the nanorods. The increase in fluorescent signal was also shown to correlate well with the integrated deposition current, indicating that the

amount of current supplied to the system is well correlated with the amount of deposited Sn. The Sn nanostructures were determined to be metallic using XANES. GTSAXS followed how the in-plane ordering and relative domains of the pores in the oxide changed with the deposition. A decrease of in-plane ordering and domain size was detected and attributed to the pores filling unevenly. The uneven filling can be explained by variations in the barrier layer between the pores, resulting in differences in the deposition current in the pores. SEM was used to image the Sn within the NP-AAO after the deposition, showing Sn nanorods inside the pores. These nanorods were shown to have a non-uniform height confirming the GTSAXS measurement. This deposition process results in aluminium samples with a glossy black finish.

Paper III. *Electrochemical Fabrication and Characterization of Palladium Nanowires in Nanoporous Alumina Templates*

Paper III focus on gaining a deeper knowledge about how the NP-AAO template affects the nanostructure growth of Pd, its grain size, strain, chemical and crystalline state.

The electrochemical deposition of Pd into NP-AAO and the effect of the confined growth on the Pd nanowires were here of interest. Two different NP-AAO templates were used for the electrochemical deposition, one grown with an 0.3 M sulphuric acid electrolyte with a potential of 25 V and one with an 0.3 M oxalic acid electrolyte with a potential of 40 V, resulting in pores with 25 nm and 40 nm diameters, respectively. The templates were constructed through a two-step anodization process and barrier layer thinning. The electrochemical deposition was conducted using pulsed deposition in a neutral electrolyte containing $\text{Pd}(\text{NH}_3)_4\text{Cl}_2$ and NH_4Cl . The pulsed deposition applied -10 V for 5 ms to deposit the palladium, followed by a potential of 10 V for 5 ms to discharge the barrier layer, after which an off period of 0 V was applied for 190 ms before applying a new pulse.

The grown nanowires were investigated with SEM, HR-TEM, EDS and XRD. The SEM measurements visualised the nanorods inside the pores and from this, the height of the nanorods could be measured. The HR-TEM was used for investigating the atomic structure of the Pd nanorods as they had been dissolved from the template and showed that the rods contained crystalline grains with sizes in the range of the nanowire diameter. EDS could show that the Pd nanorods were constructed from pure Pd. The SXRD showed that the palladium nanostructures were constructed from many small crystalline grains, and was also used to gain information about the strain and the size of the grains in the pores. It could be detected that the grains were longer in the direction along the rods compared to across the rods for the nanostructures grown in either of the two NP-AAO templated. The measured strain in the nanorods showed compressive strain perpendicular to the rods and tensile strain along the rods.

Paper IV. *Electrochemical synthesis of Au nanostructures using porous anodic alumina templates*

Paper IV focus on gaining a deeper knowledge about how the NP-AAO template and deposition time affect the nanostructure growth of Au, the strain and grain size as well as the chemical and crystal state of the structures.

The electrochemical deposition of Au into NP-AAO was investigated using SEM, TEM, EDS, SAED and XRD. The NP-AAO used were created using a two-step anodization process in 0.3 M H₂SO₄ at 25 V followed by either a barrier layer thinning or a pore widening step, creating two different templates for the electrodeposition. The electrolyte used for the deposition was a combination of HAuCl₄ and H₂SO₄ added into a phosphate buffer solution containing H₃PO₄ and KOH. Pulsed deposition was used for growing the Au structures inside of the NP-AAO using a pulse of -17.5 V for 2 ms followed by a pulse of 17.5 V for 2 ms, after these pulses a there was a rest period of 196 ms before applying a new pulse. Either nanorods or spherical nanoparticles of Au could be grown, which was grown was controlled by the deposition time and the template.

The effect of the pore modifications, pore widening and barrier layer thinning on the barrier layer and the deposition process into the aluminium template was investigated. FIB-SEM imaged the Au inside of the pores, where it was possible to see that the pore widened template led to a more homogenous height of the nanostructures but with a lower height than those grown in the barrier layer thinned template. The EDS measurements showed that the nanowires were constructed from pure Au. TEM was used to get a high-resolution image of the Au nanostructures, and together with SAED, it could be determined that the nanostructures are polycrystalline. The XRD measurements used x-rays with an energy of 25 keV to follow the deposition into a pore widened aluminium template using two different geometries, grazing-incidence and Bragg-Brentano. From these measurements, the grain size and strain of the Au nanostructures were determined. The horizontal grain size was measured to be in the range of the pore diameter, a compressive strain was measured across the nanowires and a tensile strain along the growth direction of the nanowires.

Paper V. *An electrochemical cell for 2-dimensional surface optical reflectance during anodization and cyclic voltammetry*

Paper V focus on the potential of applying 2D-SOR to electrochemical measurements and how we can modify our electrochemical cell to be compatible with the 2D-SOR technique.

The inclusion of a glass window in our electrochemical cell makes it possible to apply 2D-SOR to electrochemical reactions for studying the surface changes during the reaction. 2D-SOR was used to follow the surface changes of polycrystalline Al

during anodization and Au(111) and Pt(100) single crystals during cyclic voltammetry. The reflectance changes in the 2D-SOR were shown to be clearly correlated with the measured current of the electrochemical reactions, making it possible to detect oxidation and reduction of the surface with the 2D-SOR signal.

The polycrystalline Al sample was anodized using anodization conditions which creates a barrier layer oxide. It was shown that as the oxide grows in thickness with higher and higher applied anodization potential the 2D-SOR reflectance decreased, until 70 V where the reflectance started to increase again.

The CV measurements of the Au(111) was performed using a 0.05 M H₂SO₄ electrolyte and scanning between 0 V and 2 V. The reflectance was shown to correlate well with the CV measurements, where the reflectance decreased in intensity as the surface was oxidized and increased in intensity as the surface was reduced. This lead, to a high detected reflectance at low applied potentials and a low reflectance at high applied potentials, showing that the surface will reflect differently if it is oxidized or reduced.

The CV measurements for Pt(100) was performed in a 0.05 M H₂SO₄ electrolyte and scanning between 0.005 V and 1.65 V. The reflectance showed a similar trend to the one detected for the Au(111). However, the Pt(100) surface had regions that reacted differently to the CV scanning, where some areas were shown to have a continuous decrease in reflectance related to a degradation of the surface in these regions.

The changes in 2D-SOR reflectance were in this paper well correlated with known features in the measured CV, making this a good technique to spatially follow the surface changes.

Paper VI. *Operando Reflectance Microscopy on Polycrystalline Surfaces in Thermal Catalysis, Electrocatalysis and Corrosion*

Paper VI focus on showing the potential of the 2D-SOR for applications in realistic environments and on more complex (polycrystalline) and industrial (steel) samples.

2D-SOR was used to follow the surface changes of a polycrystalline Pd during CO oxidation in gas-phase, polycrystalline Au during CV and super duplex stainless steel during corrosion, where it was possible to see how the surface grains behaved differently during the reactions. EBSD was used for all three samples to characterise the different gains of the surface.

For the polycrystalline Pd, the catalytic activity of the different surface grains was studied during CO oxidation. It was possible to see that the reflectance had a sharp decrease when the high activity region of the sample was reached, indicating oxidation of the surface. It was also shown that the reflectance of the different crystallographic grains behaved quite differently during the CO oxidation, with the

grains close to a (100) orientation having a large continuous decreasing in reflectance and the grains close to a (110) or (111) orientation showing a smaller decrease in reflectance during the oxidation.

On the Au sample, electrocatalysis was investigated by performing CV measurements on the sample between -0.1 V and 2 V in a 0.1 M H_2SO_4 electrolyte. The reflectance decreased as the surface was oxidized and increased as it was reduced. A clear difference in the 2D-SOR signal between the grains was visible during the CV measurement. It could be shown that the 2D-SOR reflectance started to decrease at a lower potential for the most uncoordinated surface, which is due to this surface starting to oxidize at a lower potential compared to the less uncoordinated surfaces.

Corrosion of the super duplex stainless steel sample from Sandvik, a real industrial sample, was investigated by performing CV measurements on the sample between -0.9 V and 1.5 V in a 1 M NaCl electrolyte. The sample contains both ferrite and austenite grains, which are visible with the 2D-SOR. The CV curve could detect the oxidation of Cr(III) at a potential of 1.4 V and reduction at 0.5 V, this could be correlated with a decrease and increase in the 2D-SOR reflectance, respectively. A continuous dissolution of Cr from the sample was detected by the CV signal, which was detected in the 2D-SOR as a continuous decrease in reflectance. The dissolution rate of the ferrite and austenite grains differed, which were detected with the 2D-SOR as a stronger decrease in reflectance for the ferrite grains since they dissolved faster.

These measurements showed the potential of the 2D-SOR to follow heterogeneous samples in realistic experimental environments.

Paper VII. *The brightest gold: A combined high energy x-ray diffraction and optical reflectance study of the Au(111) surface during cyclic voltammetry*

Paper VII focus on the potential of combining HESXRD and 2D-SOR to study surface changes on Au(111) during the electrochemical reaction, for gaining knowledge about atomic and micro/macrosopic surface changes. It demonstrates the power of the 2D-SOR to detect atomistic surface changes.

The surface changes of an Au(111) single crystal sample during cyclic voltammetry was followed using 2D-SOR and HESXRD. The CV measurements were conducted in our modified electrochemical PEEK cell using an electrolyte of 0.1 M HClO_4 and scanning between 0 V and 1.75 V. The measurements showed clearly how the 2D-SOR signal followed the CV curve in the same manner as in paper V, where a decrease in reflectance could be detected when the surface oxidized and an increase in the reflectance was detected as the surface was once again reduced. The HESXRD signal followed how the intensity of the CTR signal from the unreconstructed (1×1) Au surface and the intensity of the SLR from the reconstructed $(22 \times \sqrt{3})$ HB

surface changed as a function of the CV measurement. The SLR signal was present when the HB was on the surface of the Au(111) single crystal, and at the same time, the CTR signal disappeared due to the mixed surface of HCP and FCC sites during the HB reconstruction. As the HB reconstruction was lifted the SLR disappeared and the CTR increased in intensity. During oxidation of the surface, the CTR vanished, indicating oxidation and roughening of the surface. There were no additional peaks detected in the HESXRD pattern due to the formation of the Au oxide, suggesting that the oxide is amorphous.

By correlating the 2D-SOR signal and the HESXRD measurements it was possible to follow how the atomic surface changes affected the reflectance signal. As the HB was lifted and the unreconstructed 1x1 surface was recovered, the 2D-SOR decreased in reflectance which is suggested to be due to a roughening of the surface by Au island formation and a decrease in atom density (since the HB is denser than the unreconstructed 1x1 surface). When the CTR signal disappears due to the formation of an oxide on the surface the 2D-SOR continues to decrease, showing that 2D-SOR can follow the oxidation and the continued roughening of the surface. The most interesting thing about the 2D-SOR measurements is the increase in reflectance as the HB reconstruction (the most dense Au(111) surface) is present on the surface. Since the HB reconstruction is a monolayer reconstruction this shows the potential of the 2D-SOR to detect surface changes in the range of Ångströms when the sample is inside a liquid.

A theoretical simulation was performed for the reconstructed Au(111) surface, which confirmed the measured SLR and CTR intensities.

Paper XIII. *The electro-oxidation of Au(111): An ex situ Electrochemical, XPS and LEED study.*

Paper XIII focus on gaining a deeper knowledge of the oxidation of Au(111), using a newly developed XPS-LEED setup. The investigation of the chemical species on the surface during electrooxidation is here one of the main interests.

The experiments used an 0.05 M H₂SO₄ electrolyte and performed both CV and LSV measurements, and measured XPS at specific potentials. LEED was measured at just a few of the potentials used for XPS. In the first measurement, a CV was scanned between - 0.2 V and 1.6 V, which didn't show any large changes in the surface, except that the HB reconstruction had been lifted.

The second measurement was a LSV scan, where the potential was stopped and held at specific values for 30 s before extraction of the sample from the electrolyte. These measurements showed peaks in the O 1s and S 2p spectra indicating the presence of SO_x species on the surface at potentials between 1.8 - 2.0 V. When a potential of 2.1 V was reached, the peak in the S 2p spectra disappeared together with new peaks

appearing in the O 1s and Au 4f spectra indicating the desorption of the SO_x and the formation of an Au oxide on the sample's surface.

The third experiment was a LSV scan, where the potential instead was stopped and held at specific values for 300 s. At an applied potential of 1.6 V there appeared peaks in the O 1s and S 2p spectra indicating the presence of sulphate or bi-sulphate ions adsorbed on the surface. These peaks disappeared as new peaks appeared in the O 1s and Au 4f spectra at a potential of 1.8 V, at which point the formation of an oxide on the surface will start. The oxide will continue to grow as the potential is increased. The LEED signal showed a nicely ordered Au(111) surface with the HB present after UHV cleaning and before any oxidation. During the oxidation, the LEED pattern disappeared suggesting that the formed oxide will be unordered, in agreement with paper IV.

The difference between the three measurements for when there is sulphate on the surface and when the oxide starts to form is likely due to the time the specific potentials are applied to the gold sample.

Paper IX. High-energy surface x-ray diffraction reveals the dynamic surface structure of Au(111) in acidic media

Paper IV focuses on demonstrating how HESXRD can follow the dynamics of the HB reconstruction and the development of the HESXRD-Analysis-Toolkit (HAT) software to analyse the HESXRD images.

HESXRD were used to follow the dynamics of the HB reconstruction on the Au(111) during CV in 0.1 M HClO₄ electrolyte. By the development of the computer software HESXRD-Analysis-Toolkit (HAT), time-resolved reciprocal space maps could be created and used to follow the dynamics of the reconstruction. It was shown that the lifting of the HB reconstruction is kinetically slow and that the potential for the lifting of the HB had a slight difference between the two scan rates 2 mV/s and 5 mV/s, where the lifting occurs at a slightly higher potential for the later one. The formation of the HB reconstruction is shown to have an activation barrier that has to be overcome before the reconstruction occurs, this is indicated by the reconstruction appearing at the same potential for both scan rates.

Conclusions & Outlook

This thesis has studied electrochemical processes both *in situ* and *ex situ*. The electrochemical deposition of Sn, Pd and Au into NP-AAO has been followed with different x-ray techniques to gain information about the deposition process and the crystallographic and chemical information about the deposited nanostructures. These were complemented with *ex situ* measurements to visualise and investigate the nanostructures more closely. The measurements showed that the nanostructures grew from the bottom up and that all of them had a metallic structure. It was also possible to show the effect the NP-AAO template had on the growth and the structure of the nanostructures, on for example the strain in the nanostructures, where a tensile strain was measured along the Pd and Au nanostructures and a compressive strain was measured across them.

This thesis also showed the potential to apply our newly developed 2D-SOR technique to electrochemical measurements, where we follow surface changes due to oxidation, roughening and reduction of the sample's surface. It was also shown that 2D-SOR can detect surface changes in the Ångström range since it could detect the presence of the monolayer HB reconstruction on Au(111). Polycrystalline samples were also investigated with this technique, where it could spatially resolve the different grains. It was possible to follow how the different grains in the Pd, Au and the SDSS samples behave differently during the reactions taking place, making it a useful technique for studying the changes of many different crystallographic orientations simultaneously. This shows that 2D-SOR has great potential for further applications in surface science related measurements.

The dynamics and structural changes of the Au(111) surface were followed with both *in situ* and *ex situ* techniques showing how an amorphous oxide is formed on the surface as it is oxidized. During the oxidation and OER, the surface will become rougher. It was also shown that adsorption of sulphate ions onto the surface occurs before any formation of a gold oxide. The dynamics of the HB reconstruction, its lifting and reappearance were studied in detail using HESXRD.

Further studies for the grown nanostructures would be to test the catalytic activity of the grown Pd nanowires and to use the grown Au nanostructures for the growth of ordered III-V nanowires.

Further studies using the 2D-SOR would be to combine it with HESXRD to study other surface orientations and polycrystalline samples. This would make it possible

to correlate the atomic changes of these surface with the measured reflectance. By correlating atomic changes with the features in the reflectance signal it could be used on its own, after enough characteristics have been made, to determine atomic structural changes of samples studied in the home lab. The possibility to study polycrystalline materials will make it valuable to follow how different surface structures reacts to the same experimental condition. This could be used for creating libraries of the structures and their specific reflectance signal.

2D-SOR could also be combined with Grazing Incidence XAS in thermal catalysis or electrochemistry using model catalysts or electrodes, which would provide a microscopic image of the sample with simultaneous chemical formation.

The studies of the structural changes in the Au(111) surface, could help to get a better understanding of how the electrooxidation and the OER reaction affect the gold surface and how the surface structure might promote or poison these reactions. In particular, the understanding of the dissolution and the resulting stability of the anode is an important issue in green H₂ production through water splitting for the development of better fuel cells.

References

- [1] S. Das and V. Jayaraman, ‘SnO₂: A comprehensive review on structures and gas sensors’, *Prog Mater Sci*, vol. 66, pp. 112–255, 2014.
- [2] P. Offermans, H. D. Tong, C. J. M. van Rijn, P. Merken, S. H. Brongersma, and M. Crego-Calma, ‘Ultralow-power hydrogen sensing with single palladium nanowires’, *Appl Phys Lett*, vol. 94, pp. 223100-1-223110–3, 2009.
- [3] C. Xu, H. Wang, P. K. Shen, and S. P. Jiang, ‘Highly Ordered Pd Nanowire Arrays as Effective Electrocatalysts for Ethanol Oxidation in Direct Alcohol Fuel Cells’, *Adv. Mater.*, vol. 19, pp. 4256–4259, 2007.
- [4] K. T. Kim, S. J. Sim, and S. M. Cho, ‘Hydrogen gas sensor using Pd nanowires electrodeposited into anodized alumina template’, *IEEE Sens J*, vol. 6, pp. 509–513, 2006.
- [5] K. Aslan, J. Zhang, J. R. Lakowicz, and C. D. Geddes, ‘Saccharide Sensing Using Gold and Silver Nanoparticles - A Review’, *J. Fluoresc.*, vol. 4.4, pp. 391–400, 2004.
- [6] S. Zeng, K.-T. Yong, I. Roy, X.-Q. Dinh, X. Yu, and F. Luan, ‘A Review on Functionalized Gold Nanoparticles for Biosensing Applications’, *Plasmonics*, vol. 6, pp. 491–506, 2011.
- [7] M. Haruta, ‘Catalysis of Gold Nanoparticles Deposited on Metal Oxides’, *CATTECH*, vol. 6.3, pp. 102–115.
- [8] S. A. Fortuna and X. Li, ‘Metalcatalyzed semiconductor nanowires: a review on the control of growth directions’, *Semicond. Sci. Technol.*, vol. 25.2, pp. 024005–16, 2010.
- [9] ‘Sapa, Sapa ytbehandling, anodisering, pulverlackering och decoral’, *Sapa*, 2018.
- [10] H. Wang, C. Xu, F. Cheng, and S. Jiang, ‘Pd nanowire arrays as electrocatalysts for ethanol electrooxidation’, *Electrochem. Commun.*, vol. 9, 2007.
- [11] L. D. Burke and P. F. Nugent, ‘The Electrochemistry of Gold: I The Redox Behaviour of the Metal in Aqueous Media’, *Gold Bull.*, vol. 30, pp. 43–53, 1997.
- [12] P. Marcus, ‘Surface science approach of corrosion phenomena’, *Electrochimica Acta*, vol. 43, pp. 109–118, 1998.
- [13] V. Maurice and P. Marcus, ‘Progress in corrosion science at atomic and nanometric scales’, *Prog. Mater. Sci.*, vol. 85, pp. 132–171, 2018.
- [14] O. Diaz-Morales, F. Calle-Vallejo, C. de Munck, and T. M. Koper, ‘Electrochemical water splitting by gold: evidence for an oxide decomposition mechanism’, *Chem. Sci.*, vol. 4, pp. 2334–2343, 2013.

- [15] W. G. Onderwaater, A. Taranovskyy, G. M. Bremmer, G. C. van Baarle, J. W. M. Frenken, and I. M. N. Groot, 'From dull to shiny: A novel setup for reflectance difference analysis under catalytic conditions', *Rev Sci Instrum*, vol. 88, pp. 023704-1-023704-6, 2017.
- [16] W. G. Onderwaater, A. Taranovskyy, G. C. van Baarle, J. W. M. Frenken, and I. M. N. Groot, 'In situ Optical Reflectance Difference Observations of CO Oxidation over Pd(100)', *J Phys Chem C*, vol. 121, pp. 11407-11415, 2017.
- [17] S. Albertin *et al.*, 'Surface optical reflectance combined with x-ray techniques during gas-surface interactions', *J. Phys. Appl. Phys.*, vol. 53, 2020.
- [18] S. Pfaff *et al.*, 'Combining high-energy X-ray diffraction with Surface Optical Reflectance and Planar Laser Induced Fluorescence for operando catalyst surface characterization', *Rev Sci Instrum*, vol. 90, pp. 033603-1-033603-8, 2019.
- [19] P. Hofmann, *Surface Physics: An Introduction*, 1.4. 2016.
- [20] P. Willmott, *An Introduction to Synchrotron Radiation: Techniques and Applications*, 1st Edition., vol. 2011. John Wiley and Sons, Inc.
- [21] P. Villars and K. Cenzual, 'Pd Crystal Structure: Datasheet from "PAULING FILE Multinaries Edition - 2012" in SpringerMaterials (https://materials.springer.com/isp/crystallographic/docs/sd_0450964)'.
https://materials.springer.com/isp/crystallographic/docs/sd_0532183.
- [22] P. Villars and K. Cenzual, 'Al Crystal Structure: Datasheet from "PAULING FILE Multinaries Edition - 2012" in SpringerMaterials (https://materials.springer.com/isp/crystallographic/docs/sd_0251015)'.
https://materials.springer.com/isp/crystallographic/docs/sd_0251015.
- [23] P. Villars and K. Cenzual, 'Pt Crystal Structure: Datasheet from "PAULING FILE Multinaries Edition - 2012" in SpringerMaterials (https://materials.springer.com/isp/crystallographic/docs/sd_0250187)'.
https://materials.springer.com/isp/crystallographic/docs/sd_0250899.
- [24] P. Villars and K. Cenzual, 'Au Crystal Structure: Datasheet from "PAULING FILE Multinaries Edition - 2012" in SpringerMaterials (https://materials.springer.com/isp/crystallographic/docs/sd_0261045)'.
https://materials.springer.com/isp/crystallographic/docs/sd_1625529.
- [25] R. Pöttgen, 'Stannides and Intermetallic Tin Compounds - Fundamentals and Applications', *Z. Für Naturforschung B*, vol. 61,6, pp. 677-698, 2014.
- [26] C. Kittel, *Introduction to Solid State Physics*, 8th ed. John Wiley and Sons, Inc, 2004.
- [27] P. Villars, 'β-Sn (Sn rt) Crystal Structure, PAULING FILE in: Inorganic Solid Phases, SpringerMaterials (online database), Springer, Heidelberg (ed.) SpringerMaterials (https://materials.springer.com/isp/crystallographic/docs/sd_1830515)'.
https://materials.springer.com/isp/crystallographic/docs/sd_1830515.
- [28] L. F. Pašteka, Y. Hao, A. Borschevsky, V. V. Flambaum, and P. Schwerdtfeger, 'Material Size Dependence on Fundamental Constants', *Phys Rev Lett*, vol. 122, pp. 160801-1-160801-8, 2019.

- [29] J. Als-Nielsen and D. McMorrow, *Elements of Modern X-ray Physics*, 2nd ed. John Wiley and Sons, 2011.
- [30] P. Hofmann, *Solid State Physics: An Introduction*, 2nd ed. Wiley-VCH Verlag GmbH & Co KGaA, 2015.
- [31] Y. Gründer, G. S. Harlow, E. Cocklin, J. Fogg, J. W. Beane, and C. A. Lucas, 'Potential-dependent surface compression of gold and its link to electrocatalytic reactivity', *Surf. Sci.*, vol. 680, pp. 113–118, 2019.
- [32] J. Wang and B. M. Ocko, 'In situ x-ray-diffraction and -reflectivity studies of the Au(111)/electrolyte interface: Reconstruction and anion adsorption', *Phys Rev B*, vol. 46, pp. 10321–10338, 1992.
- [33] K. Oura, M. Katayama, A. V. Zotov, V. G. Lifshits, and A. A. Saranin, *Surface Science An Introduction*. 2003.
- [34] J. Evertsson *et al.*, 'The thickness of native oxides on aluminum alloys and single crystals', *Appl Surf Sci*, vol. 349, pp. 826–832, 2015.
- [35] L. P. H. Jeurgens, W. G. Sloof, F. D. Tichelaar, C. G. Borsboom, and E. J. Mittenmeijer, 'Determination of thickness and composition of aluminium-oxide overlayers on aluminium substrates', *Appl Surf Sci*, vol. 144–145, pp. 11–15, 1999.
- [36] F. Bertram *et al.*, 'In situ anodisation of aluminium surfaces studied by X-ray reflectivity and electrochemical impedance spectroscopy', *J Appl Phys*, vol. 116, pp. 034902-1-03492-6, 2014.
- [37] W. Lee and S. J. Park, 'Porous Anodic Aluminium Oxide: Anodisation and Templated Synthesis of Functional Nanostructures', *Chem Rev*, vol. 114, pp. 7487–7556, 2014.
- [38] M. M. Lohregel, 'Thin anodic oxide layers on aluminium and other valve metals: high field regime', *Mater. Sci. Eng. R Rep.*, vol. 11, 6, pp. 243–294, 1993.
- [39] A. N. Gleizes, D. Samelot, C. Vahlas, V. Saru-Kanian, P. Florian, and D. Massiot, 'Temperature Dependent 4-, 5- and 6-Fold Coordination of Aluminium in MOCVD-Grown Amorphous Alumina Films: From Local Coordination to Material Properties', *Adv. Sci. Technol.*, vol. 91, p. 123, 2014.
- [40] T. Shirai, H. Watanabe, and M. Fuji, 'Structural properties and surface characteristics on aluminium oxide powders', *Annu. Rep. Ceram. Res. Lab. Nagoya Inst. Technol.*, vol. 9, pp. 23–31, 2009.
- [41] J. W. Diggle, T. C. Downie, and C. W. Goulding, 'Anodic oxide film on aluminium', *Chem Rev*, vol. 69, pp. 365–405, 1969.
- [42] H. Hashimoto, K. Tazawa, H. Asho, and S. Ono, 'NMR Spectroscopic Analysis of the Local Structure of Porous-Type Amorphous Alumina Prepared by Anodisation', *J Phys Chem C*, vol. 121, 22, pp. 12300–12307, 2017.
- [43] I. Farnan, R. Dupree, G. E. Jeong, G. C. Wood, and A. J. Forty, 'Structural chemistry of anodic alumina', *Thin Solid Films*, vol. 173, pp. 209–215, 1989.
- [44] E. J. W. Verwey, 'Electrolytic conduction of a solid insulator at high fields The formation of the anodic oxide film on aluminium', *Physica*, vol. 2, pp. 1059–1063, 1935.

- [45] J. F. Dewald, 'A Theory of the Kinetics of Formation of Anode Films at High Fields', *J Electrochem Soc*, vol. 102, pp. 1–6, 1955.
- [46] J. D. Baran, H. Grönbeck, and A. Hellman, 'Mechanism for Limiting Thickness of Thin Oxide Films on Aluminium', *Phys. Rev. Lett.*, vol. 112, pp. 146103-1-146103-5, 2014.
- [47] N. Cabrera and N. F. Mott, 'Theory of the oxidation of metals', *Rep Prog Phys*, vol. 12, pp. 163–184, 1949.
- [48] F. P. Fehlner and N. F. Mott, 'Low-Temperature Oxidation', *Oxidation Met.*, vol. 2, pp. 59–99, 1970.
- [49] H. Masuda and M. Satoh, 'Fabrication of gold nanodot array using anodic porous alumina as an evaporation mask', *Jpn J Appl Phys*, vol. 35, pp. L126–L129, 1996.
- [50] H. Masuda and K. Fukuda, 'Ordered metal nanohole arrays made by a two-step replication of honeycomb structures of anodic alumina', *Science*, vol. 268, pp. 1466–1468, 1995.
- [51] F. Li, L. Zhang, and R. M. Metzger, 'On the Growth of Highly Ordered Pores in Anodized Aluminum Oxide', *Chem Mater*, vol. 10, pp. 2470–2480, 1998.
- [52] P. Skeldon, G. E. Thompson, S. J. Garcia-Vergara, L. Inglesias-Rubianes, and C. E. Blanco-Pinzon, 'A Tracer Study of Porous Anodic Alumina', *Electrochem. Solid-State Lett.*, vol. 9, pp. B47–B51, 2006.
- [53] K. R. Herbert, 'Kinetics of anodic oxidation of aluminium and titanium: formation of porous alumina and titanium oxide nanotube layers', *Encycl. Interfacial Chem. Surf. Sci. Electrochem. Ref. Module Chem. Mol. Sci. Chem. Eng.*, pp. 267–283, 2018.
- [54] S. Ono, M. Saito, M. Ishiguro, and H. Asho, 'Controlling factor of selfordering of anodic porous alumina', *J Electrochem Soc*, vol. 151, pp. B473–B478.
- [55] J. Zhang, J. E. Kielbasa, and D. L. Carroll, 'Controllable fabrication of porous alumina templates for nanostructures synthesis', *Mater Chem Phys*, vol. 122, pp. 295–300, 2010.
- [56] N. A. Vinogradov *et al.*, 'Observation of Pore Growth and Self-Organization in Anodic Alumina by Time-Resolved X-ray Scattering', *ACS Appl Nano Mater*, vol. 2018, no. 1, 3, pp. 1265–1271.
- [57] J. Evertsson *et al.*, 'Self-organization of porous anodic alumina films studied in situ by grazing-incidence transmission small-angle X-ray scattering', *RSC Adv.*, vol. 2018, no. 8, pp. 18980–18991.
- [58] E. J. Mittenmeijer, *Fundamentals of materials science: the microstructure-property relationship using metals as model systems*. Heidelberg; New York: Springer., 2010.
- [59] S. H. Na and C. H. Park, 'First-Principles Study of the structural Phase Transition in Sn', *J. Korean Phys. Soc.*, vol. 56,1, pp. 494–497, 2010.
- [60] A. Kumar, M. M. Mohammadi, and M. T. Swihart, 'Synthesis, growth mechanisms, and applications of palladium-based nanowires and other one-dimensional nanostructures', *Nanoscale*, vol. 11, pp. 19058–19085, 2019.

- [61] G. Slaughter and T. Kulkarni, 'Fabrication of palladium nanowire array electrode for biofuel cell application', *Microelectron. Eng.*, vol. 149, pp. 92–96.
- [62] J. S. Lee, M. H. Seo, K. W. Choi, J. Y. Yoo, M. S. Jo, and J. B. Yoon, 'Stress-engineered palladium nanowires for wide range (0.1%–3.9%) of H₂ detection with high durability', *Nanoscale*, vol. 11, pp. 16317–16326, 2019.
- [63] Y. Huang, P. J. Kooyman, and M. T. M. Koper, 'Intermediate stages of electrochemical oxidation of single-crystalline platinum revealed by in situ Raman spectroscopy', *Nat. Commun.*, vol. 7, pp. 1–7, 2016.
- [64] D. J. S. Sandbeck, O. Brummel, K. J. J. Mayrhofer, J. Libuda, I. Katsounaros, and S. Cherevko, 'Dissolution of Platinum Single Crystals in Acidic Medium', *ChemPhysChem*, vol. 20, pp. 2997–3003, 2019.
- [65] O. T. Holton and J. W. Stevenson, 'The Role of Platinum in Proton Exchange Membrane Fuel Cells', *Platin. Met. Rev.*, vol. 57, pp. 259–271.
- [66] A. Borg, A.-M. Hilmen, and E. Bergene, 'STM studies of clean, CO- and O-exposed Pt(100)-hex-R0.7"', *Surf. Sci.*, vol. 306, 1994.
- [67] Sandvik AB, 'SANDVIK SAF 2507® SUPER-DUPLEX STAINLESS STEEL'. SANDVIK SAF 2507® SUPER-DUPLEX STAINLESS STEEL (accessed Mar. 10, 2021).
- [68] P. Rodriguez and M. T. M. Koper, 'Electrocatalysis on gold', *Phys.Chem.Chem.Phys.*, vol. 16, pp. 13583–13594, 2014.
- [69] J. Wang, A. J. Davenport, H. S. Isaacs, and B. M. Ocko, 'Surface Charge-Induced Ordering of the Au(111) Surface', *Science*, vol. 255, pp. 1416–1418, 1992.
- [70] A. T. Hubbard, *The Handbook of Surface Imaging and Visualization*, 1st ed. CRC Press, 1995.
- [71] A. R. Sandy, S. G. J. Mochrie, D. M. Zehner, G. Grübel, K. G. Huang, and D. Gibbs, 'Au(111) and Pt(111) surface phase behavior', *Surf. Sci.*, vol. 287–288, Part 1, pp. 321–324, 1993.
- [72] Y. Wang, N. S. Hush., and J. R. Reimers, 'Simulation of the Au(111) - (22 x $\sqrt{3}$) surface reconstruction', *Phys Rev B*, vol. 75, pp. 233416-1-233416-4, 2007.
- [73] F. Hanke and J. Björk, 'Structure and local reactivity of the Au(111) surface reconstruction', *Phys Rev B*, vol. 87, pp. 235422-1-235422-6, 2013.
- [74] J. V. Barth, H. Brune, G. Ertl, and R. J. Behm, 'Scanning tunneling microscopy observations on the reconstructed Au(111) surface: Atomic structure, long-range superstructure, rotational domains, and surface defects', *Phys Rev B*, vol. 42, p. 9307, 1990.
- [75] F. Rossel, P. Brodard, F. Patthey, N. V. Richardson, and S. Wolf-Dieter, 'Modified herringbone reconstruction on Au(111) induced by self-assembled Azure A islands', *Surf. Sci.*, vol. 602, pp. L115–L117, 2008.
- [76] A. P. Seitsonen, 'Electronic structure of reconstructed Au(111) studied with density functional theory', *Surf. Sci.*, vol. 643, pp. 150–155, 2016.
- [77] S. B. Darling, A. W. Rosenbaum, Y. Wang, and S. J. Sibener, 'Coexistence of the (23 × $\sqrt{3}$) Au(111) Reconstruction and a Striped Phase Self-Assembled Monolayer', *Langmuir*, vol. 18, pp. 7462–7468, 2002.

- [78] Ch. Wöll, S. Chiang, R. J. Wilson, and P. H. Lippel, ‘Determination of atom positions at stacking-fault dislocations on Au(111) by scanning tunneling microscopy’, *Phys Rev B Condens Matter*, vol. 39, pp. 7988–7991, 1989.
- [79] F. Reinert and G. Nicolay, ‘Influence of the herringbone reconstruction on the surface electronic structure of Au(111)’, *Appl Phys A*, vol. 78, pp. 817–821, 2004.
- [80] W. Chen, V. Madhavan, T. Jamneala, and M. F. Crommie, ‘Scanning Tunneling Microscopy Observation of an Electronic Superlattice at the Surface of Clean Gold’, *Phys Rev Lett*, vol. 80, pp. 1469–1472, 1998.
- [81] J. Zhou, S. Blomberg, J. Gustafson, E. Lundgren, and J. Zetterberg, ‘Simultaneous Imaging of Gas Phase over and Surface Reflectance of a Pd(100) Single Crystal during CO Oxidation’, *J Phys Chem C*, vol. 121, pp. 23511–23519, 2017.
- [82] C. Vaz-Dominguez, A. Aranzábal, and A. Cuesta, ‘In Situ STM Observation of Stable Dislocation Networks during the Initial Stages of the Lifting of the Reconstruction on Au(111) Electrodes’, *J Phys Chem Lett*, vol. 1, pp. 2059–2062, 2010.
- [83] M. Pourbaix, *Atlas of Electrochemical Equilibria in Aqueous Solutions*, 2nd ed. National Association of Corrosion Engineers, 1974.
- [84] M. Nicol, ‘The anodic behaviour of gold’, *Gold Bull.*, vol. 13, pp. 46–55, 1980.
- [85] R. Puddephatt, *The Chemistry of Gol*. Elsevier, 1978.
- [86] H. Shi, R. Asahi, and C. Stampfl, ‘Properties of the gold oxides Au₂O₃ and Au₂O: First-principles investigation’, *Phys Rev B*, vol. 75, pp. 205125-1-205125-8, 2007.
- [87] D. Kawamoto *et al.*, ‘Structure of a Gold(III) Hydroxide and Determination of Its Solubility’, *Bull. Chem. Soc. Jpn.*, vol. 89, pp. 1385–1390, 2016.
- [88] A. Hamelin, ‘Cyclic voltammetry at gold single-crystal surfaces. Part 1. Behaviour at low-index faces’, *J. Electroanal. Chem.*, vol. 407, pp. 1–11, 1996.
- [89] P. Rodriguez, N. Garcia-Araez, and M. T. M. Koper, ‘Self-promotion mechanism for CO electrooxidation on goldw’, *Phys. Chem. Chem. Phys.*, vol. 32, pp. 9373–9380, 2010.
- [90] N. D. S. Canning, D. Outka, and R. J. Madix, ‘The adsorption of oxygen on gold’, *Surf. Sci.*, vol. 141, pp. 240–254, 1984.
- [91] A. Cuesta, M. Kleinert, and D. M. Kolb, ‘The adsorption of sulfate and phosphate on Au(111) and Au(100) electrodes : an in situ STM study’, *Phys. Chem. Chem. Phys.*, vol. 2, pp. 5684–5690, 2000.
- [92] J. Desilvestro and M. J. Weaver, ‘Surface structural changes during oxidation of gold electrodes in aqueous media as detected using surface-enhanced Raman spectroscopy’, *J. Electroanal. Chem. Interfacial Electrochem.*, vol. 209, pp. 377–386, 1986.
- [93] T. Kondo *et al.*, ‘Structure of Au(111) and Au(100) Single-Crystal Electrode Surfaces at Various Potentials in Sulfuric Acid Solution Determined by In Situ Surface X-ray Scattering’, *J Phys Chem C*, vol. 35, pp. 13197–13204, 2007.
- [94] H. Angersterin-Kozłowska, B. E. Conway, A. Hamelin, and L. Stoicoviciu, ‘Elementary steps of electrochemical oxidation of single-crystal planes of Au

- Part II. A chemical and structural basis of oxidation of the (111) plane', *J. Electroanal. Chem. Interfacial Electrochem.*, vol. 228, pp. 429–453, 1987.
- [95] F. Gossenberger, F. Juarez, and A. Groß, 'Sulfate, Bisulfate and Hydrogen Co-adsorption on Pt(111) and Au(111) in an Electrochemical Environment', *Front Chem*, vol. 8, pp. 1–11, 2020.
- [96] T. Kondo, J. Zegenhagen, S. Takakusagi, and K. Uosaki, 'In situ real-time study on potential induced structure change at Au(111) and Au(100) single crystal electrode/sulfuric acid solution interfaces by surface x-ray scattering', *Surf. Sci.*, vol. 631, pp. 96–104.
- [97] C. Zoski, *Handbook of Electrochemistry*, 1st ed. Elsevier, 2007.
- [98] A. J. Bard and L. R. Faulkner, *Electrochemical methods: Fundamentals and Applications*, 2nd ed. John Wiley and Sons, Inc, 2001.
- [99] N. Elgrishi, K. J. Rountree, B. D. McCarthy, E. S. Rountree, T. Eisenhart, and J. L. Dempsey, 'A Practical Beginner's Guide to Cyclic Voltammetry', *J Chem Educ*, vol. 95, 2, pp. 197–206, 2018.
- [100] Y. Shao, 'Electrochemistry at Liquid/Liquid Interfaces', in *Handbook of Electrochemistry*, 2007th ed., Elsevier.
- [101] C. Xu, G. Li, H. Zhao, and H. Li, 'Electrodeposition of ferromagnetic nanowire arrays on AAO/Ti/Si substrate for ultrahigh-density magnetic storage devices', *Mater Lett*, vol. 60, pp. 2335–2338, 2006.
- [102] H. Umh, H. H. Shin, J. Yi, and Y. Kim, 'Fabrication of gold nanowires (GNW) using aluminium anodic oxide (AAO) as a metal-ion sensor', *Korean J Chem Eng*, vol. 32, pp. 299–302, 2015.
- [103] P. T. Kissinger and W. R. Heineman, 'Cyclic voltammetry', *J Chem Educ*, vol. 60, pp. 701–706, 1983.
- [104] F. Scholz, *Electroanalytical Methods: Guide to Experiments and Applications*, 2nd ed. Springer, 2010.
- [105] R. G. Compton, E. Laborda, and K. R. Ward, *Understanding voltammetry: Simulation of Electrode Processes*. Imperial College Press, 2014.
- [106] D. V. Tripkovic, D. Strmcnik, D. van der Vliet, V. Stamenkovic, and N. M. Markovic, 'The role of anions in surface electrochemistry', *Faraday Discuss.*, vol. 140, pp. 25–40, 2009.
- [107] Y. Xu, G. C. Thompson, G. C. Wood, and B. Bethune, 'ANION INCORPORATION AND MIGRATION DURING BARRIER FILM FORMATION ON ALUMINIUM', *Corros. Sci.*, vol. 27, pp. 83–102, 1987.
- [108] W. Lee, K. Schwim, M. Steinhart, P. Eckhard, R. Scholz, and Gösele, 'Structural engineering of nanoporous anodic aluminium oxide by pulse anodisation of aluminium', *Nat. Nanotechnol.*, vol. 3, pp. 234–239, 2008.
- [109] Y. D. Gamburg and G. Zangari, *Theory and Practice of Metal Electrodeposition*. Springer New York, 2011.
- [110] K. Nielsch, F. Müller, A. P. Li, and U. Gösele, 'Uniform Nickel Deposition into Ordered Alumina Pores by Pulsed Electrodeposition', *Adv. Mater.*, vol. 8, pp. 582–586, 2004.

- [111] D. Li and E. Podlaha, ‘Template-Assisted Electrodeposition of Fe-Ni-Co Nanowires: Effects of Electrolyte pH and Sodium Lauryl Sulfate’, *J Electrochem Soc*, vol. 164, 3, pp. D843–D851, 2017.
- [112] J. K. Wang, J. M. Char, and P. J. Lien, ‘Optimization Study on Supercritical Electrodeposition of Nickel Nanowire Arrays Using AAO Template’, *ISRN Chem. Eng.*, pp. 1–5, 2012.
- [113] W. J. Stępniewski, W. Florkiewicz, M. Norek, M. Michalska-Domańska, E. Kościuczyk, and T. Czujko, ‘Various modifications of electrochemical barrier layer thinning of anodic aluminium oxide’, *Int. J. Chem. Mol. Nucl. Mater. Metall. Eng.*, vol. 8, pp. 1488–1491, 2014.
- [114] C. Furneaux, W. R. Rigby, and A. P. Davidson, ‘The formation of controlled-porosity membranes from anodically oxidized aluminium’, *Nature*, vol. 337, pp. 147–149, 1989.
- [115] N. Taşaltın, S. Öztürk, N. Kılınç, H. Yüzer, and Z. Z. Özrürk, ‘Fabrication of vertically aligned Pd nanowire array in AAO template by electrodeposition using neutral electrolyte’, *Nanoscale Res Lett*, vol. 5, pp. 1137–1143, 2010.
- [116] V. Haehnel *et al.*, ‘Towards smooth and pure iron nanowires grown by electrodeposition in self-organized alumina membranes’, *Acta Mater.*, vol. 58, 7, pp. 2330–2337, 2010.
- [117] R. Felici, ‘Surface X-Ray Diffraction’, in *Characterization of Materials*, 2003 by John Wiley & Sons, Inc, 2012.
- [118] G. Renaud, R. Lazzai, and F. Leroy, ‘Probing surface and interface morphology with Grazing Incidence Small Angle X-Ray Scattering’, *Surf Sci Rep*, vol. 2009, no. 64, pp. 255–380.
- [119] P. Müller-Buschbaum, ‘A Basic Introduction to Grazing Incidence Small-Angle X-Ray Scattering’, *Lect Notes Phys*, vol. 2009, no. 776, pp. 61–89.
- [120] X. Lu, K. G. Yager, D. Johnston, C. T. Black, and B. M. Ocko, ‘Grazing-incidence transmission X-ray scattering: surface scattering in the Born approximation’, *J. Appl. Cryst.*, vol. 2013, no. 46, pp. 165–172.
- [121] J. Gustafson *et al.*, ‘High-Energy Surface X-ray Diffraction for Fast Surface Structure Determination’, *Science*, vol. 343, no. 6172, pp. 758–761, 2014.
- [122] E. Arakawa, ‘Surface X-Ray Diffraction’, in *Compendium of Surface and Interface Analysis*, Springer, Singapore, 2018.
- [123] I. K. Robinson and D. J. Tweet, ‘Surface X-ray Diffraction’, *Rep Prog Phys*, vol. 55, pp. 599–651, 1992.
- [124] I. Robinson, P. Eng, and R. Schuster, ‘Origin of the Surface Sensitivity in Surface X-Ray Diffraction’, *Acta Phys. Pol. A*, vol. 86, pp. 513–520, 1994.
- [125] T. Fuchs *et al.*, ‘Structure dependency of the atomic-scale mechanisms of platinum electro-oxidation and dissolution’, *Nat. Catal.*, vol. 3, pp. 754–761.

- [126] U. Hejral, M. Shipilin, J. Gustafson, A. Stierle, and E. Lundgren, 'High energy surface x-ray diffraction applied to model catalyst surfaces at work', *J Phys Condens Matter*, vol. 33, 2021.
- [127] S. Cherevko, A. A. Topalov, A. R. Zeradjanin, I. Katsounaros, and K. J. J. Mayrhofer, 'Gold dissolution: towards understanding of noble metal corrosion', *RSC Adv.*, vol. 3, 2013.
- [128] P. Müller-Buschbaum and A. Hexemer, 'Advanced grazing-incidence techniques for modern soft-matter materials analysis', *IUCrJ*, vol. 2012, no. 2(Pt 1), pp. 106–125.
- [129] T. Li, A. J. Senesei, and B. Lee, 'Small Angle X-ray Scattering for Nanoparticle Research', *Chem Rev*, vol. 2016, no. 116, 18, pp. 11128–11180.
- [130] N. Mahadevapuram, J. Strzalka, and G. E. Stein, 'Grazing-Incidence Transmission Small Angle X-Ray Scattering from Thin Films of Block Copolymers', *J Polym Sci Part B Polym Phys*, vol. 2013, no. 51, 7, pp. 602–610.
- [131] J. Yano and V. K. Yachandra, 'X-ray absorption spectroscopy', *Photosynth Res*, vol. 102(2–3), pp. 241–254, 2009.
- [132] G. S. Henderson, F. M. F. de Groot, and B. J. A. Moulton, 'X-ray Absorption Near-Edge Structure (XANES) Spectroscopy', *Rev Miner. Geochem*, vol. 78, pp. 75–138, 2016.
- [133] B. Ravel and M. Newville, 'ATHENA, ARTEMIS, HEPHAESTUS: data analysis for X-ray absorption spectroscopy using IFEFFIT', *J Synchrotron Radiat*, vol. 12(Pt 4), pp. 537–541, 2005.
- [134] F. A. Stevie and C. L. Donley, 'Introduction to x-ray photoelectron spectroscopy', *J Vac Sci Technol A*, vol. 38, pp. 063204-1-063204–20, 2020.
- [135] K. Siegbahn, 'Electron Spectroscopy for Atoms, Molecules, and Condensed Matter', *Science*, vol. 217, pp. 111–121, 1982.
- [136] Nobel Media AB, 'The Nobel Prize in Physics 1981'. <https://www.nobelprize.org/prizes/physics/1981/summary/>.
- [137] S. Oswald, 'X-Ray Photoelectron Spectroscopy in Analysis of Surfaces', in *Encyclopedia of Analytical Chemistry: Applications, Theory and Instrumentation*, John Wiley & Sons, Ltd, 2013.
- [138] J. F. Moulder, W. F. Stickle, P. E. Sobol, and K. D. Bomben, *Handbook of X-ray Photoelectron Spectroscopy*. Perkin-Elmer Corporation, Physical Electronics Division, 1992.
- [139] C. N. Berglund and W. E. Spicer, 'Photoemission Studies of Copper and Silver: Theory', *Phys. Rev.*, vol. 136, pp. A1030–A1044, 1964.
- [140] C. N. Berglund and W. E. Spicer, 'Photoemission Studies of Copper and Silver: Experiment', *Phys. Rev.*, vol. 136, pp. A1044–A1064, 1964.
- [141] P. Hofmann, *Surface Physics: An Introduction*, 1.4 Edition., vol. 2016. Philip Hofmann.
- [142] S. Morita, F. J. Giessibl, and R. Wiesendanger, *Noncontact Atomic Force Microscopy*, vol. 2009. Springer-Verlag Berlin Heidelberg.
- [143] J. Evertsson, *Protective and Nanoporous Alumina Films Studied in situ by X-ray and Electrochemical Methods*. Lund University, Faculty of

- Science, Department of Physics, Division of Synchrotron Radiation Research., 2017.
- [144] The Kavli Nanoscience Institute at Caltech, ‘Scanning Electron Microscopy (SEM) Lecture: Principles, Techniques & Applications’, 2020, Accessed: Apr. 12, 2021. [Online]. Available: <https://www.youtube.com/watch?v=Zh21tp3aPEw>.
- [145] W. Zhou and Z. L. Wang, *Scanning Microscopy for Nanotechnology: Techniques and applications*. Springer Science+Business Media, LLC, 2006.
- [146] J. I. Goldstein, D. E. Newbury, J. R. Michael, N. W. M. Ritchie, J. H. J. Scott, and D. C. Joy, *Scanning Electron Microscopy and X-Ray Microanalysis*, 4th ed. © Springer Science+Business Media LLC 2018.
- [147] L. A. Giannuzzi and F. A. Stevie, ‘A review of focused ion beam milling techniques for TEM specimen preparation’, *Micron*, vol. 30, pp. 197–204, 1999.
- [148] The Kavli Nanoscience Institute at Caltech, ‘Gallium Focused Ion Beam (Ga-FIB) Lecture: Principles, Techniques & Applications’, 2020, Accessed: Apr. 12, 2021. [Online]. Available: The Kavli Nanoscience Institute at Caltech.
- [149] C. A. Volkert and A. M. Minor, ‘Focused Ion Beam Microscopy and Micromachining’, *MRS Bull.*, vol. 35(2), pp. 289–399, 2007.
- [150] D. B. Williams and C. B. Carter, *Transmission Electron Microscopy, Part 1: Basics*, 2nd ed. Springer, 2009.
- [151] T. Coffey, ‘Transmission Electron Microscopy (TEM) basics’, 2017, [Online]. Available: <https://www.youtube.com/watch?v=1oGOWpiVvw8>.
- [152] A. V. Girão and G. Caputo, ‘Application of Scanning Electron Microscopy-Energy Dispersive X-ray Spectroscopy (SEM-EDS)’, in *Comprehensive Analytical Chemistry*, vol. 75, 2017.
- [153] D. Woodruff, ‘Low Energy Electron Diffraction’, in *Reference Module in Materials Science and Materials Engineering*, Elsevier, 2016.
- [154] S. Y. Tong, ‘THEORY OF LOW-ENERGY ELECTRON DIFFRACTION’, *Prog. Surf. Sci.*, vol. 7, pp. 1–48, 1975.